Summer 8-31-2008

Novel polypropylene based microporous membranes via spherulitic deformation

Kuan-Yin Lin
New Jersey Institute of Technology

ABSTRACT

NOVEL POLYPROPYLENE BASED MICROPOROUS MEMBRANES VIA SPHERULITIC DEFORMATION

by
Kuan-Yin Lin

A novel method for creating a microporous polypropylene membrane via spherulitic deformation is described. The microporous structure was generated by the combination of intra-spherulitic and inter-spherulitic deformations. Polypropylene was selected due to its unique cross-hatched lamellar morphology facilitating inter-spherulitic deformation. A precursor film with a spherulitic structure was made under low-stress melt processing condition. A tangential lamellae-rich spherulite was created and identified with a positive birefringence sign. A sequential annealing process improved the crystalline structure, and in particular the thickness of the tangential lamellae. The annealing process proved to be critical for initiating the inter-spherulitic deformation. The post-extrusion process conditions for initiating inter-spherulitic deformation to create microporous membranes by lamellar separation are delineated. The processing parameters are: annealing temperature, extension ratio, stretching rate, and stretching temperature. A fixed set of extrusion conditions was chosen for producing precursor films having similar spherulitic properties. A Wide Angle X-ray Scattering (WAXS) examination provides a quick characterization method for the inter-spherulitic deformation. Membrane porosity measurements showed a consistent correlation with the observed α-form orientation index. A highly interconnected solvent-resistant porous polypropylene membrane having a pore size in the range of 50~100 nm and a porosity

of about 0.18 was thereby developed in this study. This concept can be further expanded by using an α-nucleating agent to reduce spherulite sizes and utilizing interfacial debonding between two different phases to enhance permeability. A highly methanol permeable membrane with an estimated porosity of 0.29 was produced with the nucleated polypropylene samples, and a reasonable permeability was also observed in the membrane made from an immiscible blend. However, the occurrence of debonding can also compensate for the energy to create inter-spherulitic deformation. Increasing extension ratio did not change the microstructure in the non-annealed sample; however, the lamellae can be further oriented in the annealed samples. Inter-spherulitic deformation became obvious at slow stretching rates; intra-spherulitic deformation was more favored at a fast stretching rate. The DSC thermal analysis of the precursor films showed two significant endothermic discontinuities (T_1 at 0 °C and T_2 at 40 °C) in the non-annealed or annealed precursor films; T_1 is believed to be the conventional T_g of polypropylene; T_2 appears to be the result of the rigid amorphous fraction trapped within "lamellar wells" where the amorphous phase is surrounded by R-lamellae and T-lamellae. The lamellae could break down or slip from the lamellar knots as stretching temperatures are high enough to minimize the effect of the rigid amorphous fraction, and the annealed lamellae can still be oriented without a catastrophic cold-drawn deformation.

NOVEL POLYPROPYLENE BASED MICROPOROUS MEMBRANES VIA SPHERULITIC DEFORMATION

by
Kuan-Yin Lin

A Dissertation
Submitted to the Faculty of
New Jersey Institute of Technology
in Partial Fulfillment of the Requirements for the Degree of
Doctor of Philosophy in Chemical Engineering

Department of Chemical, Biological and Pharmaceutical Engineering

August 2008

APPROVAL PAGE

NOVEL POLYPROPYLENE BASED MICROPOROUS MEMBRANES VIA SPHERULITIC DEFORMATION

Kuan-Yin Lin

Dr. Kamalesh K. Sirkar, Dissertation Advisor — Date
Distinguished Professor of Chemical, Biological and Pharmaceutical Engineering, NJIT

Dr. Marino Xanthos, Dissertation Co-Advisor — Date
Professor of Chemical, Biological and Pharmaceutical Engineering, NJIT

Dr. Costas Gogos, Committee Member — Date
Distinguished Research Professor of Chemical, Biological and Pharmaceutical Engineering, NJIT

Dr. Edward Dreizin, Committee Member — Date
Professor of Chemical, Biological and Pharmaceutical Engineering, NJIT

Dr. Michael Jaffe, Committee Member — Date
Research Professor of Biomedical Engineering, NJIT

Dr. Kwabena A. Narh, Committee Member — Date
Associate Professor of Mechanical Engineering, NJIT

BIOGRAPHICAL SKETCH

Author: Kuan-Yin Lin

Degree: Doctor of Philosophy

Date: August 2008

Undergraduate and Graduate Education:

- Doctor of Philosophy in Chemical Engineering,
  New Jersey Institute of Technology, Newark, NJ, 2008
- Master of Science in Chemical Engineering,
  Chung Yuan Christian University, Chung Li, Taiwan, 2001
- Bachelor of Science in Chemical Engineering,
  National Taiwan University, Taipei, Taiwan, 1997

Major: Chemical Engineering

Presentations and Publications:

K. –Y. Lin, M. Xanthos and K. K. Sirkar,
"Novel polypropylene microporous membrane via spherulitic deformation"
Journal of Membrane Science, submitted.

K. –Y. Lin, M. Xanthos and K. K. Sirkar,
"Nanoporous Membranes by Solventless Melt Processing and Post-treatments"
Conference Proceeding, NSF design, Service and Manufacturing Grantees and Research Conference 2006.

K. –Y. Lin, M. Xanthos and K. K. Sirkar,
"Novel Immiscible Blends for Membrane Applications"
Conference Proceeding, Annual Technical Conference – ANTEC 2005.

K. –Y. Lin, D. –M. Wang and J. –Y. Lai,
"Nonsolvent-induced gelation and its effect on membrane morphology"
Macromolecules 35 (2002) 6697.

"Scientists study the world as it is; engineers create the world that has never been."
- Theodore von Kármán

To my beloved families and friends

ACKNOWLEDGMENT

I would like to express my deepest appreciation to Dr. Kamalesh K. Sirkar and Dr. Marino Xanthos, who not only served as my research supervisors providing valuable and countless resources, insight, and intuition, but also constantly gave me support, encouragement, and reassurance. Special thanks are given to Dr. Costas Gogos, Dr. Edward Dreizin, Dr. Michael Jaffe and Dr. Kwabena Narh for serving as members of committee. Their support and recommendations are invaluable.

Financial support and research funding provided by the National Science Foundation, the Otto H. York Department of Chemical, Biological and Pharmaceutical Engineering, and the Center for Membrane Technology are highly appreciated. I would like to acknowledge the staff of the Polymer Processing Institute (PPI) for their assistance and suggestions. I want to thank Dr. Kun Sup Hyun (PPI) for facilitating the materials acquisition, and Mr. Dale Conti and Mr. Mike Zawisa of PPI for their help with instruments in the Laboratory. A special thanks to Dr. Victor Tan (PPI) for his assistance with apparatuses and inspiring discussions.

I am also grateful to all of my colleagues and friends, Dr. Gordana Obuskovic, Dr. Praveen Kosaraju, and Dr. Liming Song for their help and suggestions. I also would like to thank Dr. George Collins and Dr. Chien-Yueh Huang for their insightful comments.

Finally, I take this opportunity to sincerely thank my parents and my sister for their unconditional love and unceasing support, and Dr. Shu-Ching Fan for her encouragement throughout this time period. It would have been impossible and meaningless to accomplish what I have done without them.

TABLE OF CONTENTS

TABLE OF CONTENTS
(Continued)

TABLE OF CONTENTS
(Continued)

LIST OF TABLES

LIST OF TABLES
(Continued)

Table **Page**

LIST OF FIGURES

LIST OF FIGURES
(Continued)

LIST OF FIGURES
(Continued)

LIST OF FIGURES
(Continued)

LIST OF FIGURES
(Continued)

LIST OF FIGURES
(Continued)

LIST OF FIGURES
(Continued)

CHAPTER 1

INTRODUCTION

1.1 Membrane Fabrication (Dense Membranes)

A membrane is a thin selective layer used to separate different species by size or solubility differences. Membrane processes can be categorized by the mechanisms adopted for the separation processes. In general, these mechanisms are divided into two types, namely, the selection in the pore-flow regime and selection in the solution-diffusion regime as shown in Figure 1.1. Based on the membrane pore size, an accepted definition for the transition between these two regimes is about 5-10 Å [1, 2]. Membranes can be made from inorganic materials (ceramic membrane), organic materials (polymeric membrane) and even natural biomedical materials (cell membrane). This study only focuses on membranes made with polymeric materials.

In the pore-flow regime, the membrane transport mechanism can be described by a pore-flow model as a pressure driven process. The typical membrane processes in this regime are microfiltration, ultrafiltration and microporous Knudsen-flow gas separation where the separation of permeating species (permeants) is based on their sizes. For example, a commonly used definition for ultrafiltration membrane is the molecular weight cut-off which is defined by 95% retention of the permeant that has a specific molecular size.

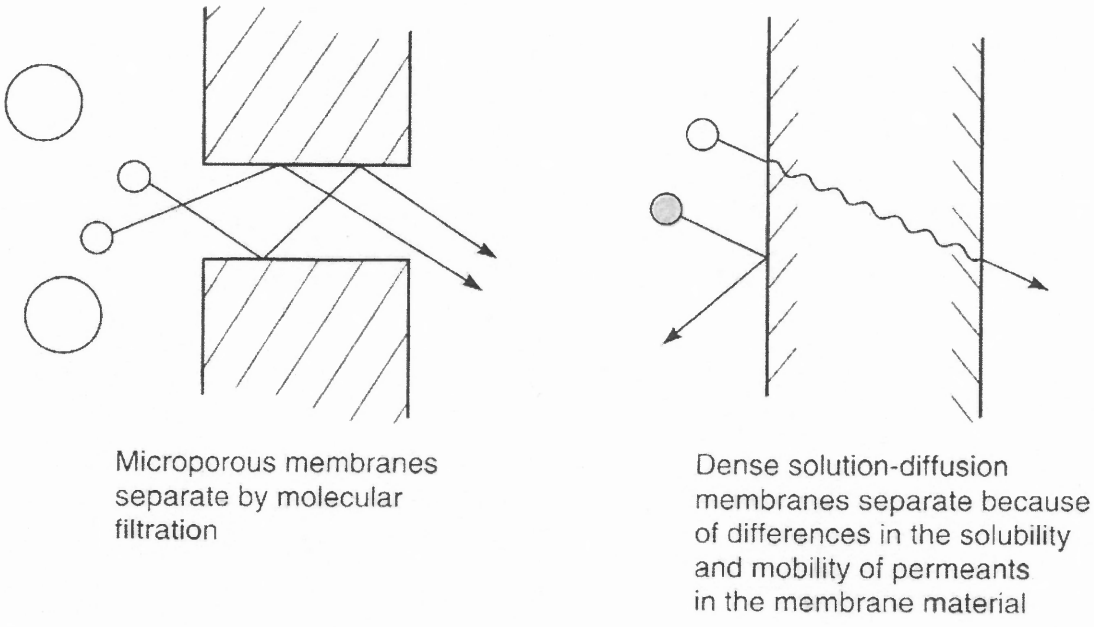

Figure 1.1 Membrane transport mechanisms; pore-flow model (left) and solution-diffusion model (right) [1].

In the solution-diffusion regime, the membrane transport mechanism is not governed only by the effect of size exclusion. The "pores" are less than 5 Å and are no longer pores in the ordinary sense. The presence of these pores is actually created by the thermal motion of polymer chains. Often the permeation is controlled by the solubility of permeants in the membrane material. Typical membrane processes in this regime are gas separation, pervaporation and reverse osmosis. A schematic representation of the pore size and their transport mechanisms is shown in Figure 1.2.

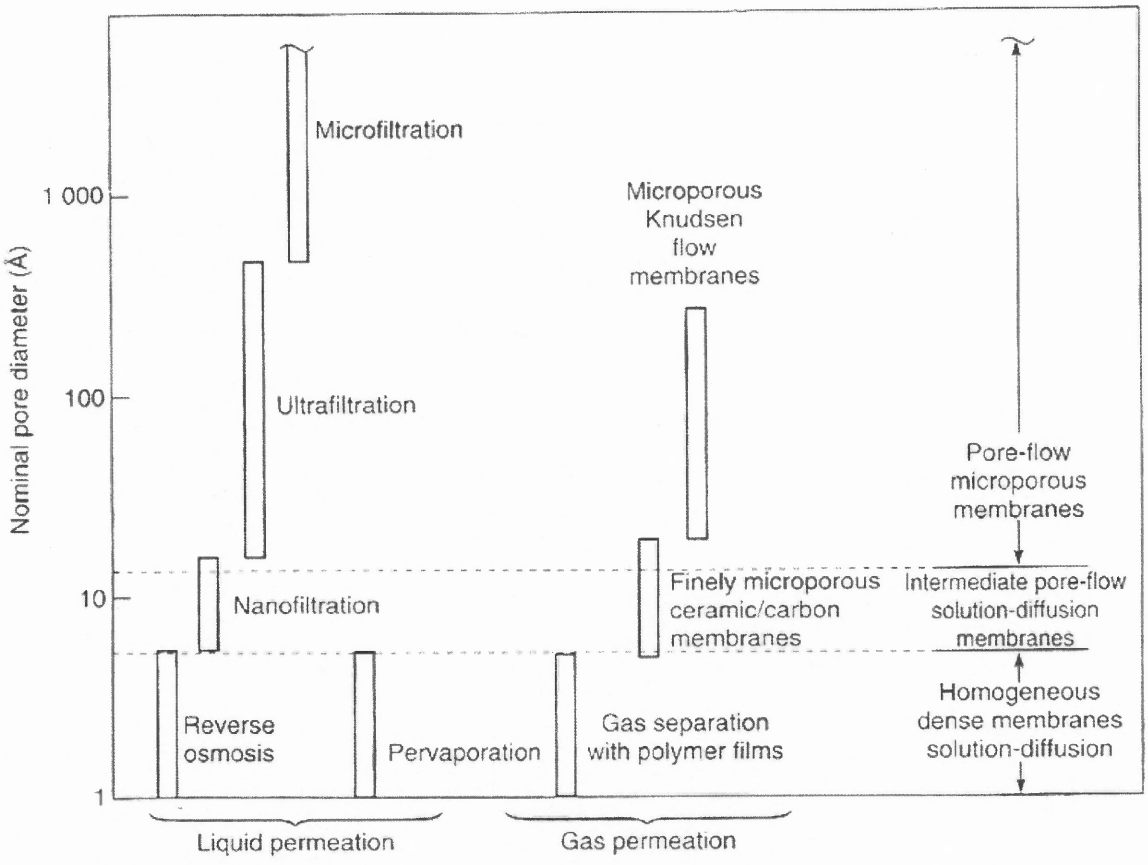

Figure 1.2 Nominal pore size of membrane processes and their mechanisms [1].

Membrane fabrication is critically important to membrane separation processes, since membrane separation relies on the existence of appropriate channels for selected permeants to pass. For pore-flow membranes, this implies a control of pore size and pore size distribution. An overview of polymeric membrane fabrication methods is considered later; the membrane fabrication processes for solution-diffusion membranes is dealt with first.

For solution-diffusion membranes, even though solubility is an important factor for the separation process, the species permeability can still be improved by enhancing the diffusivity of the selected permeant; this can be achieved by modifying the chain configurations of the polymeric materials. For gas separation membranes, it is known that the permeability of small molecules increases with increasing free volume which exists due to

imperfections in packing of the polymer chains [3]. From the perspective of modification of chain configuration, the increase in free volume can be achieved in two ways. Firstly, free volume can be modified by synthesis of flexible main chains, such as in elastomers, to lower the glass transition temperature (T_g). The free volume increases dramatically above T_g due to the much loosely packed main chains. As a result, the selectivity of the modified membranes depends mainly on the solubility of the selected permeant.

Secondly, increases in free volume can also be achieved by introducing bulky side chains into the polymeric material. In this case, T_g of the modified material is increased dramatically, and the increased free volume is due to the hindering effect on the chain packing and an increasing excess free volume. A membrane with a significantly high T_g can be created, and there is an opportunity to produce a permanent channel with a high selectivity for the permeants. These two modification methods seem to be contradictory intuitively; however, both of them have been adapted as standard modification strategies for a long time.

On the other hand, modification to achieve a novel material is not the only way to improve membrane performance. An alternative strategy is to modify membrane morphology. Membrane permeability can be dramatically increased by using thinner membranes. Asymmetric membrane morphology is the final goal since selectivity is provided by a very thin skin layer and the mechanical properties of the membranes are controlled by a more porous supporting layer. In the earliest membrane production processes, a solution-diffusion membrane was usually fabricated by pouring the polymer solution on a flat surface (such as a glass) and a dense membrane with a substantial thickness was formed after the evaporation of the solvent. The thickness of the membrane can only be reduced down to a certain range due to the occurrence of defects during solvent evaporation. Therefore, a defect

free dense membrane was usually formed with a reduction in permeability, and this is called a symmetric membrane. For making thinner dense membranes, the idea of interfacial polymerization provides an important route for making asymmetric membranes. A very thin selective layer is polymerized on the surface of a porous support which provides mechanical strength with very little permeation resistance.

Another noteworthy idea toward optimum membrane performance in recent years is the development of mixed-matrix membranes (MMMs) shown in Figure 1.3(a). The morphological modification in MMMs is achieved by combining inorganic materials (zeolites) with polymeric materials, since zeolites are acting as molecular sieves and can have very high selectivity. These membranes are utilizing zeolites to create permanent channels with a very high selectivity. In order to activate the function of MMMs, a minimum zeolite concentration of about 20~30 wt% is necessary to achieve a percolation threshold. The idea of percolation threshold is shown in Figure 1.3(b).

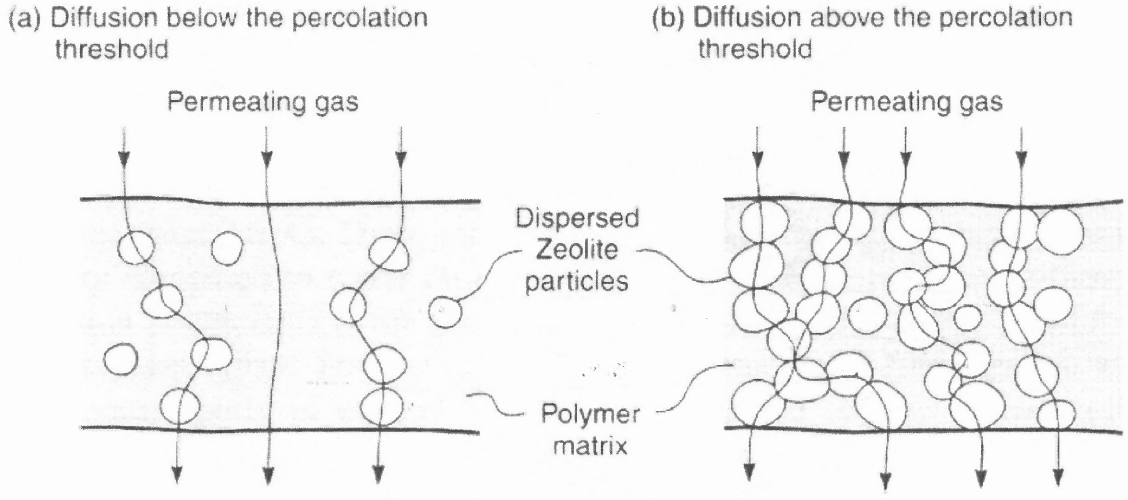

Figure 1.3 A schematic explanation of gas permeating through mixed-matrix membranes (MMMs): (a) zeolite concentration is lower than percolation threshold, (b) channels connected through zeolites are created above percolation threshold [1].

1.2 Membrane Fabrication (Porous Membranes)

For pore-flow membranes, the fabrication process is very different from those operating in the solution-diffusion regime. The smallest pore size in this regime is about 1 nm and the porous structure can not be created via the modification of polymer chains. The membrane fabrication processes for pore-flow membranes includes: phase separation, etching, sintering, and melt processing. Each of them uses a state-of-the-art technology to serve this purpose.

Phase separation is the most frequently used and also the most versatile strategy to produce pore-flow membranes. It can be further categorized into non-solvent induced phase separation (NIPS) process and thermally induced phase separation (TIPS) process based on the driving forces used to trigger the phase separation [4]. Phase separation processes can be applied to many polymers; however, a homogenous polymer solution has to be formed before initiating any phase separation. The schematic explanation for the TIPS process is shown in Figure 1.4. First of all, a polymer solution is prepared (Figure 4(a)) and kept at a high temperature to achieve a homogeneous phase (this applies to the upper critical solution temperature (UCST) system). The phase separation is achieved by cooling the polymeric solution. The polymer solution is usually cast on a porous non-woven support with a thickness less than 1 mm.

The phase separation process adapted in membrane fabrication is usually a liquid-liquid phase separation. In the TIPS process, the phase separated polymer solution is separated into two phases when the temperature becomes lower than those for the binodal curve (as shown in Figure 1.4, inserted). The two phases formed include a polymer-rich phase and a polymer-poor phase (Figure 1.4(b)). Phase separation has two steps which include nucleation and growth. In the nucleation step, the phase-separated droplets whose

concentration depends on the initial polymer solution concentration are formed. Then the droplets keep growing until they meet each other or are stopped by solidification process. The polymer concentration inside the nucleated droplets can be a polymer-poor phase if the initial polymer concentration is higher than the critical point, and can be a polymer-rich phase within a dilute solution.

The selection of initial polymer solution concentration is important. A low polymer concentration (below its critical point) can not form a sustainable membrane structure since the polymer-poor phase is predominant after phase separation. A very high polymer concentration is not feasible as well, since the polymer solution could be too viscous for the growth of polymer-poor droplets and restrict the connectivity of pores. Within a suitable initial polymer concentration range, the droplets of polymer-poor phase can grow and agglomerate into interconnected structure (Figure 1.4(c)). By carefully selecting the polymer concentration, there is a chance that the phase separation process could pass the critical point and enter the spinodal region without the interference from the binodal region. As a result, a bicontinuous phase-separated phase can be formed with a very good interconnectivity based porous structure.

A critical step for phase separation processes is to freeze (solidify) the expanding phase-separated droplets at the suitable moment. A well-controlled solidification step implies a well-controlled pore structure. Without the solidification step, the phase-separated polymer solution will eventually form two distinct layers of polymer-rich phase and polymer-poor phase (Figure 1.4(d)). In the TIPS process, the occurrence of solidification is taken care of by quenching. As the viscosity of the polymer solution is elevated with a decreasing temperature, the frozen polymer-rich phase prevents the polymer-poor droplets from further

expanding. The solidification takes over in the system as crystallization occurs (in semicrystalline polymers) or as the decreasing temperature is approaching the T_g of the polymer-rich phase.

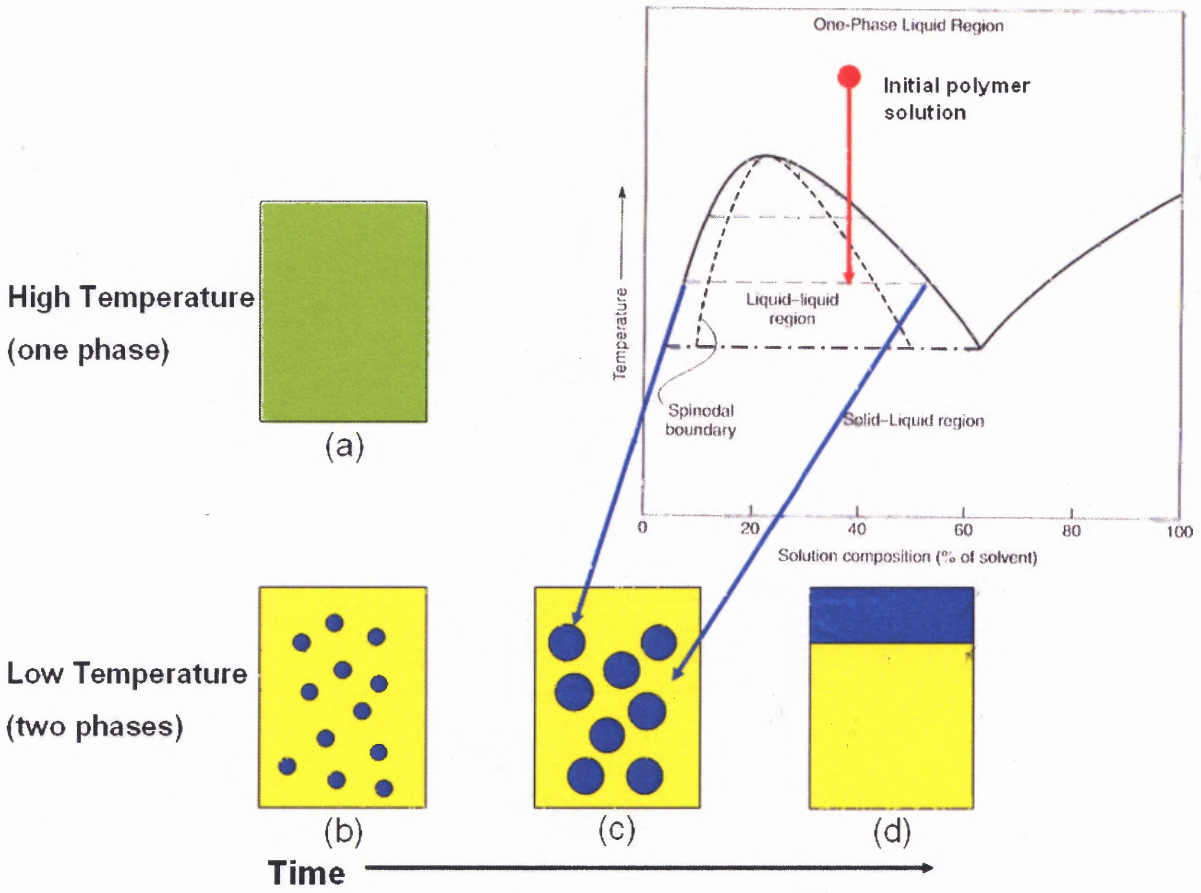

Figure 1.4 Schematic explanation for using thermally induced phase separation (TIPS) to produce pore-flow membranes: (a) polymer solution (one phase), (b) (c) (d) phase-separated polymer solution (two phases). (adapted from [1])

The same fabrication principle can also use a non-solvent as the driving force to trigger phase separation. In the NIPS process, the polymer is precipitated from the polymer solution in a nonsolvent bath. The selection of suitable solvent/non-solvent pair for the target polymer is very important in the NIPS process, since the formation of a porous structure is mainly determined by the solvent/non-solvent exchange step. The term non-solvent is related

to the polymer and not to the solvent. The chosen non-solvent and solvent pair should be completely miscible. The solidification step of the phase-separated polymer solution is facilitated by the elevated nonsolvent concentration in the cast film.

Similar to the TIPS process, it is essential to create phase-separated droplets with a polymer-poor phase and surrounded by a polymer-rich phase in order to construct a useful membrane structure. The created porous structure is frozen by the elevated viscosity of the polymer solution due to the depletion of the solvent by the non-solvent. The control of pore size in the NIPS process is far more difficult than that in the TIPS process because of the rapid solvent/non-solvent exchange. Therefore, a typical recipe for preparing a casting solution could have more than two components and would be regarded as a commercial secret by membrane making companies. Typical membrane morphologies created by the TIPS and NIPS processes are shown in Figure 1.5. The sponge-like porous structure represents the typical nucleation and growth of phase-separated polymer-poor droplets in the processes.

From the perspective of morphological modification, a favorable asymmetric porous structure can be achieved by both processes. In the TIPS process, it can be achieved by applying an evaporation step prior to the cooling step to generate a polymer concentration gradient in the cast film. After the solvent is evaporated, the polymer concentration is higher on the surface of the cast film with a faster solidification step. As a result, asymmetric membrane morphology with smaller pores close to its surface can be created as shown in Figure 1.5(a). The asymmetric morphology is easier to achieve in the NIPS process due to the rapid solvent-nonsolvent exchange step. A successful example is known as the "Loeb-Sourirajan Process" [4] which used water as a nonsolvent to precipitate cellulose acetate

from the casting solution. In this process, a very thin skin layer is formed immediately on the surface as soon as the nonsolvent contacts the casting solution. The membranes can serve the purposes of ultrafiltration as well as reverse osmosis. The skin layer is more evident in the NIPS process (Figure 1.5(b)) than in the TIPS process (Figure 1.5(a)).

This skin layer created in the NIPS process has two distinct features. First, the packing of polymer chains in the skin layer is tight enough so that its morphology is similar to that of the dense membranes fabricated by the dry casting process. Furthermore, it could be as thin as that made by the interfacial polymerization process. The porous structure beneath the skin layer provides mechanical support with very little permeation resistance, and this integrated membrane structure can be produced in just one step. However, the processing conditions of the NIPS process need to be carefully controlled in order to prevent the occurrence of macrovoids which weaken the membrane. The reason for the formation of macrovoids is believed to be the burst of non-solvent through the skin layer in the precipitation step.

Even though the NIPS process shows more advantages than the TIPS process, such as smaller pore, quick processing time and less-troublesome solvent extraction-recycle steps, the major restriction for the NIPS process is on the selection of the polymeric material for preparing the casting solution. In general, the mechanical strength of membranes increases with the molecular weight of the polymer; this also poses difficulties in the polymer solution preparation due to the decreasing solubility. The crystalline phase of semicrystalline polymer poses additional difficulties in dissolution. As a result, the NIPS process can only apply to amorphous polymers such as polysulfone and polyethersulfone. Furthermore, the membranes made by the NIPS process are vulnerable to solvents (of course, they are made by dissolution

in a solvent). An additional cross-linking step is often necessary for those membranes if the feed solution is contaminated by solvents.

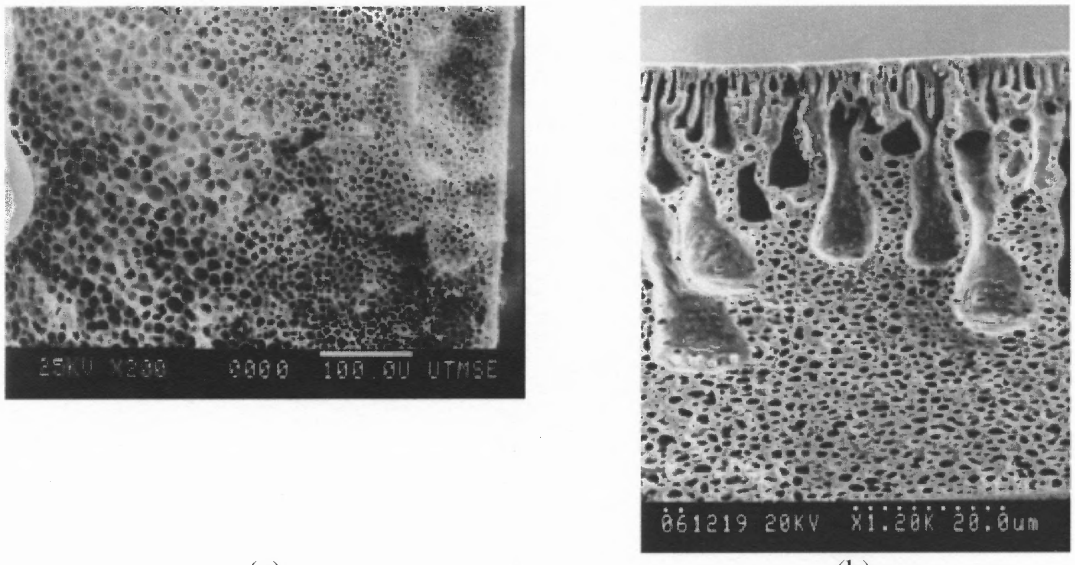

(a) (b)

Figure 1.5 Typical membrane morphology by TIPS and NIPS processes: (a) TIPS process (PP), the membrane is placed vertically and the surface is on the right [5], (b) NIPS process (Poly(methyl methacrylate) (PMMA)), the membrane is placed horizontally and surface is on the top [6].

The pore-flow membranes can also be fabricated via etching and sintering which are not always applicable due to the restrictions imposed by the available polymer systems. A membrane with very narrow pore size distribution can be prepared by etching as shown in Figure 1.6(a). A dense membrane is made first and then exposed to radiation. Well-defined cylindrical pores are produced by removing broken polymer chains in an etching bath. The etching process can only create symmetric porous structures with a low porosity and the membrane becomes very brittle as porosity increases. The pore size is also limited and can not be smaller than 0.01 μm.

Sintering is a fabrication method usually adapted for ceramic or metallic materials. The porous structure is created around the compressed powder; as a result, the pore size is

dependent on the size of the powder particles. Most polymers can not be processed by this method since conventional polymeric materials melt down easily under pressure and leave no voids around them. However, sintering could be very useful for polymeric materials such as polytetrafluoroethylene (PTFE) which has excellent thermal properties and can not be fabricated by other processes. A combination of sintering and stretching processes is necessary. In this "paste extrusion" process, the PTFE powder is blended with lubricants and compressed at high temperature followed by an extrusion step and a stretching step. A successful example is the Gore-Tex membrane whose morphology is shown in Figure 1.6(b).

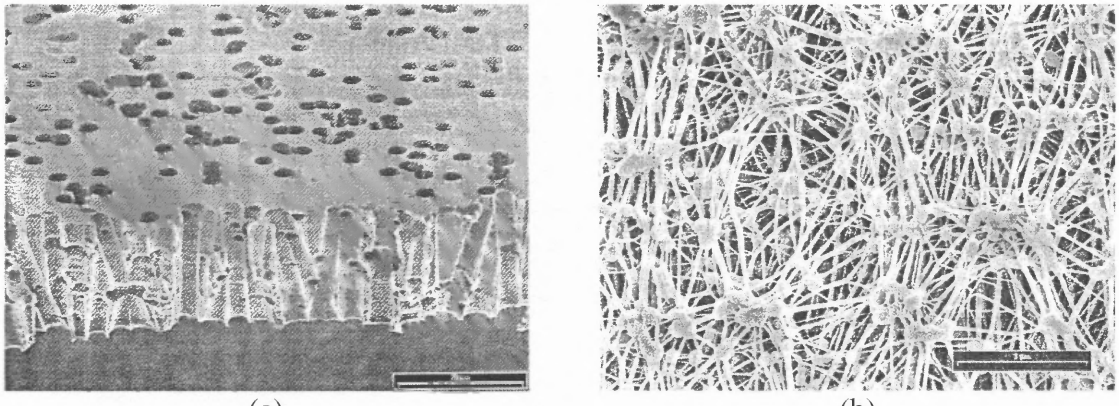

(a) (b)

Figure 1.6 Alternative methods to create pore-flow membranes: (a) etching of poly(ethylene terephthalate) (PET), (b) sintering (PTFE) [7].

1.3 Membrane Fabrication (Celgard® Process)

Semicrystalline polymers, such as polyethylene (PE) and polypropylene (PP), are excellent membrane materials with good mechanical strength, high chemical and thermal resistance thanks to the presence of a crystalline phase [8]. However, the crystalline region also restricts the processability in most conventional membrane fabrication methods. The TIPS process can be applied to semicrystalline polymers with suitable diluents; however, it is a less attractive process due to large pore sizes and the necessary post-treatments for solvents [8].

Nevertheless, there is a method which directly utilizes the crystalline phase of semicrystalline polymers to create a porous membrane without the use of any solvent. This method, also known as the Celgard® process [9], creates porous structures by deforming the crystalline region of the semicrystalline polymer. The Celgard® process includes several steps: extrusion, annealing, and stretching. In order to illustrate the concept behind these steps, some background studies on polymer crystallization and polymer deformation need to be explored.

When a semicrystalline polymer crystallizes from a dilute solution in the absence of stress, the polymer chains tend to pack and form a crystalline layer called "lamella". An electron microscope image of polyethylene crystallized from dilute solution is shown in Figure 1.7(a). The thickness of the lamella is about 10 nm and is composed of about 50 repeat units. Since the typical polymer chain length is about 1000 nm, the only explanation for the conformation of the polymer chains in the lamellar structure is a chain folding model as shown in Figure 1.7(b). The folding length increases with increasing crystallization temperature and with annealing.

Polymer crystallized from solution can also form a "shish-kebab" morphology (Figure 1.7(c)) when a stress field is applied (such as stirring a solution). The model of shish-kebab morphology (Figure 1.7(d)) suggests the lamellae (kebab) are originated from the highly oriented filament (shish) which is formed during the flow-induced crystallization.

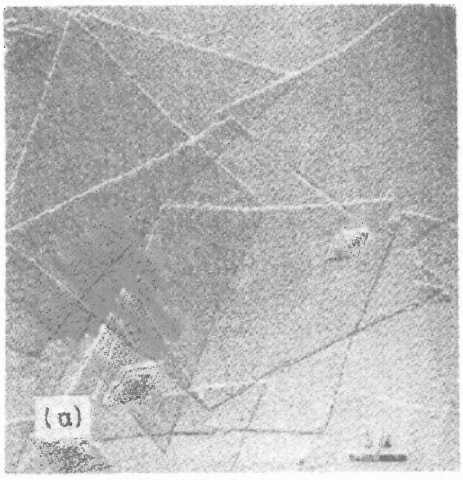

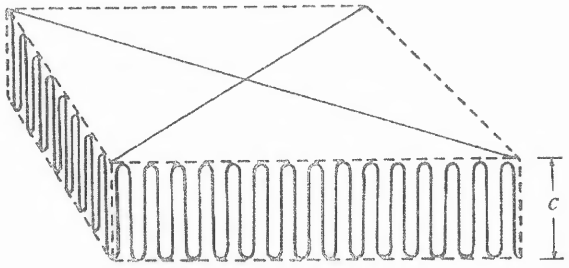

(a) (b)

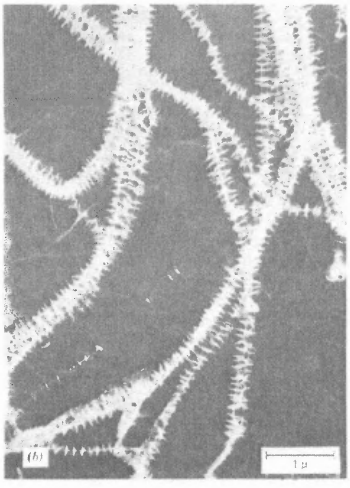

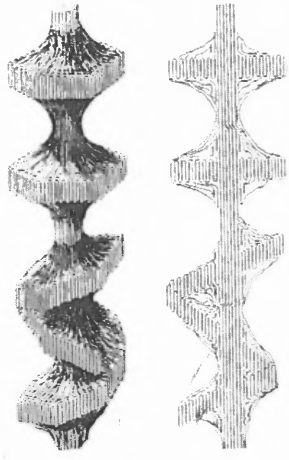

(c) (d)

Figure 1.7 Polymer crystallization from dilute solution: (a) PE in xylene (stress-free environment), (b) folding chain model of lamellar morphology, (c) PE in xylene (stressed environment), (d) model of shish-kebab morphology [10, 11].

Polymer can also crystallize from a molten state, where the chain packing and folding resembles that formed from a dilute solution; however, the aggregated lamellar morphology is quite different due to a much denser polymer chain population in the molten state. In general, these lamellae grow radially and form spherulites. The spherulites keep growing until the growing lamellar front impinges upon other spherulites. An optical microscope image of polyethylene spherulites is shown in Figure 1.8(a) and its schematic model in

Figure 1.8(b). The lamellae inside the spherulites are sandwiched by an amorphous layer (non-crystalline part) which is about of the same dimensions as the lamellae.

Under a high stress environment (such as low temperature extrusion), semicrystalline polymers can form stacked row lamellar morphology [12, 13] as shown in Figure 1.8(c). Its schematic model is shown in Figure 1.8(d). The formation mechanism of row lamellar morphology is similar to that of the shish-kebab morphology. The morphology transition from spherulites to row lamellae with increasing stress during melt processing is shown in Figure 1.9. The formation of row lamellar structure is a critical step in preparing the precursor films of the Celgard® process. This highly regular arrangement of lamellae and amorphous layers along the extrusion direction provides a regular pattern for deformation.

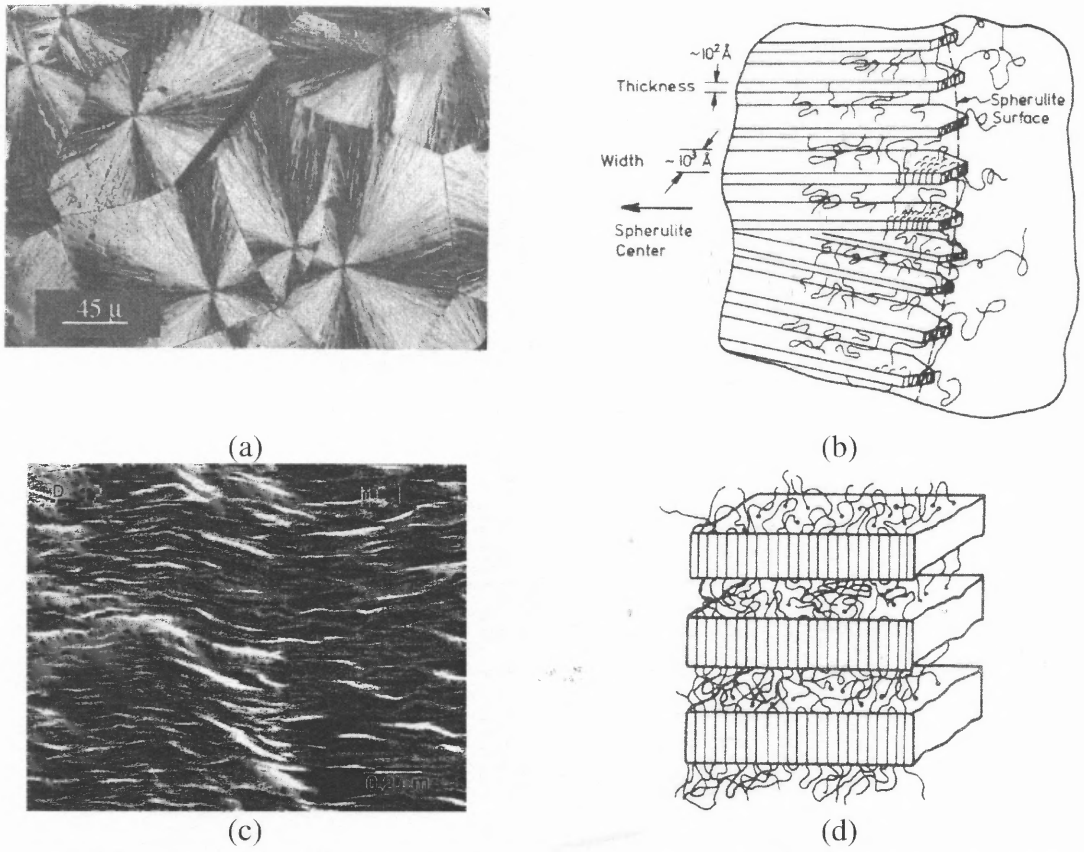

Figure 1.8 Polymer crystallization from molten state: (a) optical microscope image of PE crystallization in a stress-free environment [11], (b) model of spherulites [11], (c) electron microscope image of PE crystallization under a high stress environment [9], (d) model of row lamellae [14].

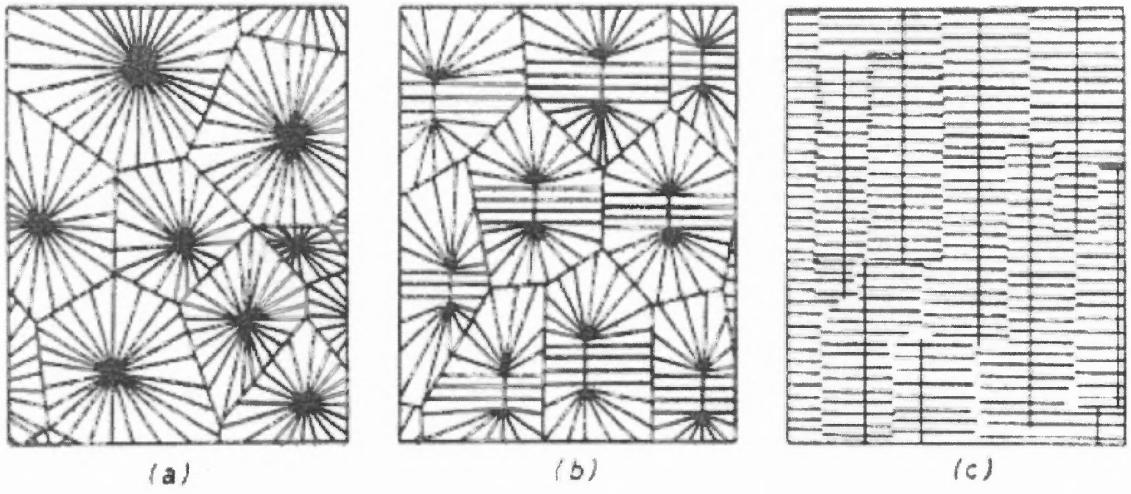

Figure 1.9 Morphology transition from spherulites to row lamellae with increasing stress during melt processing: (a) stress-free, (b) intermediate stress, (c) high stress [14].

In the Celgard® process, the extruded precursor films are undergoing an annealing step before stretching. Annealing is a heat treatment where the temperature is maintained closely below the melting point of the polymer. It is known that annealing can enhance crystalline structure by allowing the polymer chains to reorganize and form thicker lamellae with better mechanical strength. Annealing in the Celgard® process enhances the row lamellar structure without changing the arrangement of lamellae and the amorphous layers. In stretching, the amorphous region is opened up as pores, and the lamellae which are much less deformed act as structure stabilizers. The enhanced crystalline region ensures that the deformation during stretching occurs in the weaker amorphous region. As a result, a regular porous structure can be created at a similar scale as in the lamellar arrangement.

A typical polyethylene membrane made by the Celgard® process is shown in Figure 1.10(a) [9]. The residual threads between the separated lamellae are believed to be tie-molecules as shown in the model of Figure 1.10(b). Therefore, the pore size and pore density are regulated by the population of tie-molecules which is proportional to the molecular

weight. Interestingly, the hurdle on material accessibility in conventional phase separation process becomes a pre-required condition in the Celgard® process.

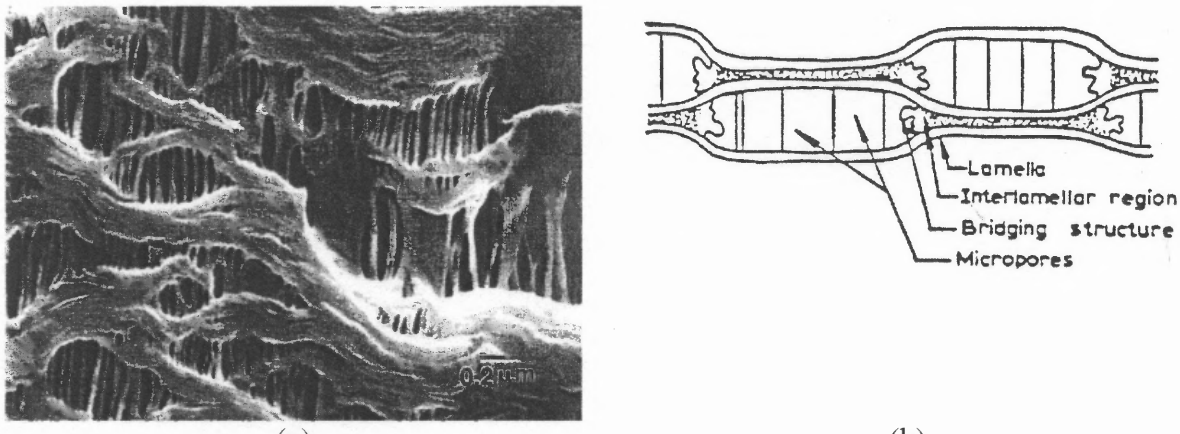

(a) (b)

Figure 1.10 (a) Electron microscope image of polyethylene membrane via the Celgard® process (b) schematic model of the deformation of row lamellae [9].

1.4 A Novel Membrane Fabrication Method via Spherulitic Deformation

In the Celgard® process, the deformation of row lamellae seems to be the ultimate strategy for utilizing the crystalline phase to create porous structure. However, there may be another way to do so. The success of the Celgard® process relies on a highly oriented and regularly distributed crystalline phase on a lamellar scale [15-18]. The row lamellar morphology provides a regular pattern for deformation during stretching. The deformed sites are always in between the lamellae. The concept could be applied to other crystalline morphologies if a similar regularity can be established, and could be deformed regularly as well.

As mentioned earlier, polymers form either spherulites or row lamellae when crystallized from the melt. A spherulitic morphology is much more often encountered than a row lamellar structure. However, to date, there is no report on the use of the deformed spherulitic morphology as a basis for making a microporous membrane, even though the

spherulitic structure has been studied for a long time. The possible reasons for that are summarized below.

Firstly, spherulites do not have the oriented regularity on a lamellar scale along the extrusion direction. In fact, lamellae grow radially into spherulites from nucleating sites. The deformation pattern of these radially aligned lamellae is irregular due to the direction of the lamellar plane (the c-axis). A schematic explanation of this irregularity is shown in Figure 1.11. During stretching, the lamellae are tilted, separated and broken, and finally the c-axis is aligned towards the stretching direction [19]. For the lamellae residing in the equatorial regions of the spherulites (based on the stretching direction), stretching would just open up the lamellae, similar to the deformation in the case of stretching row lamellae. The direction of c-axis is still preserved as before stretching. On the other hand, for the lamellae residing in the polar regions, an intense re-alignment is necessary since the c-axis of these undeformed lamellae is perpendicular to the stretching direction [20]. As shown in Figure 1.11, the lamellae are broken and aligned along the stretching direction after stretching.

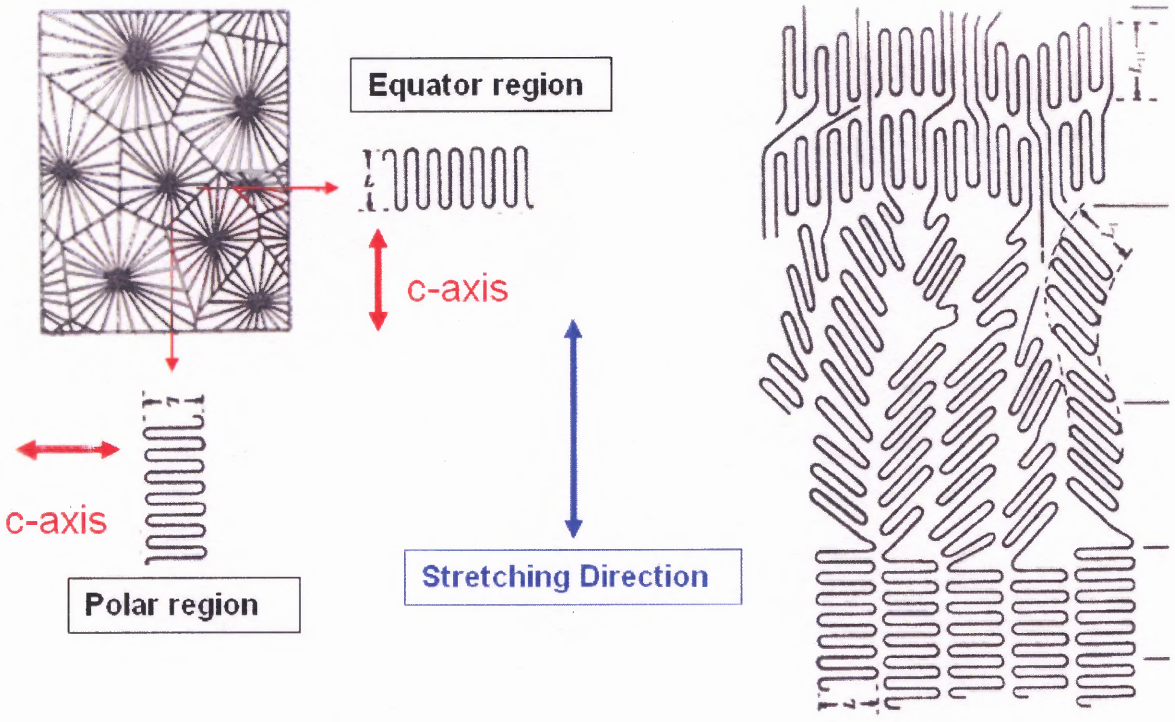

Figure 1.11 Schematic representation for lamellar irregularity in spherulites. (adapted from [14, 21])

Secondly, morphological complications in spherulite sizes and spherulite size distribution pose another difficulty in controlling the locations of the lamellar deformation. Macroscopically, the deformation of spherulites can be inter-spherulitic or intra-spherulitic as shown in Figure 1.12. For inter-spherulitic deformation (Figure 1.12(a)), the corresponding fracture sites form to compensate for the stress generated during stretching around the spherulites. It is known that the inter-spherulitic region is a weak spot since the noncrystalline part and impurities are rejected to spherulite boundaries during crystallization. Therefore, a slowly crystallized sample which has better developed spherulites often shows inter-spherulitic deformation. For intra-spherulitic deformation (Figure 1.12(b)), the lamellae inside the spherulites are broken and aligned due to the relatively weak crystalline structure. The stretched sample shows necking and cold-drawing appearance corresponding to these

oriented broken lamellae. The sample can be elongated up to several times its original length and form a highly oriented and tightly packed lamellar structure until the final structure breakdown occurs. Inter-spherulitic and intra-spherulitic deformations could be catastrophic in case of lack of tie-molecules.

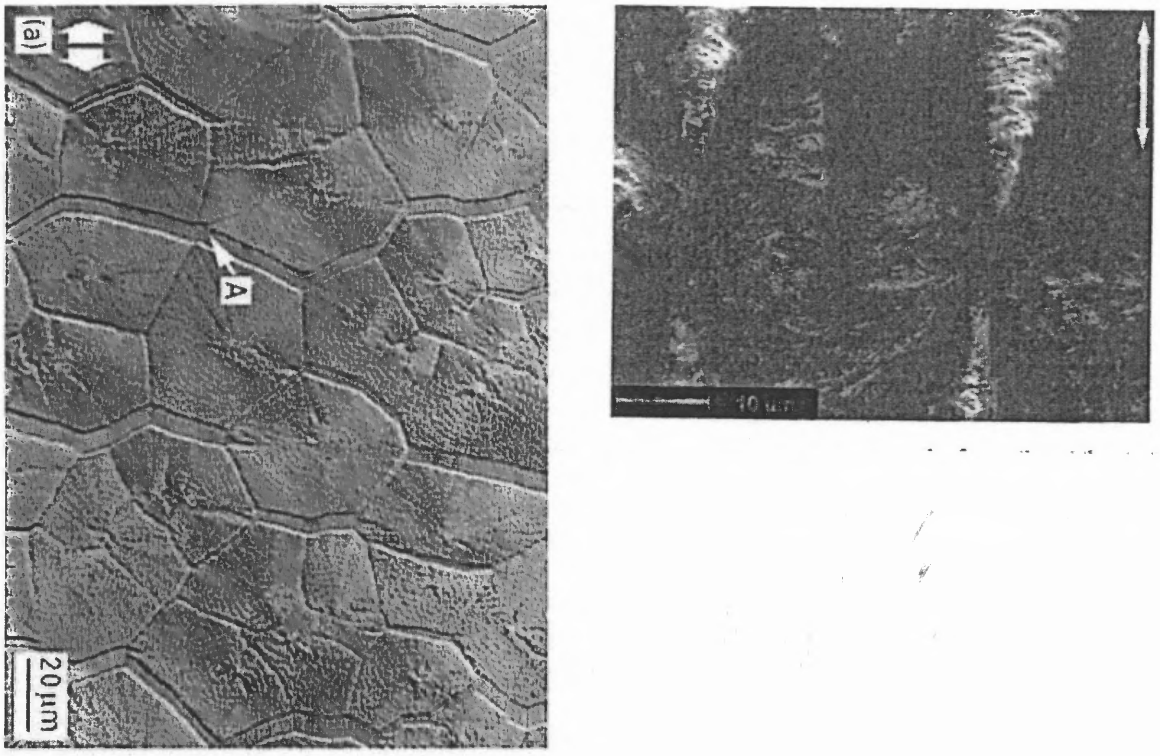

(a) (b)

Figure 1.12 (a) Inter-spherulitic deformation (PE) [22], (b) initial stage of intra-spherulitic deformation (PP) [23].

The effects of spherulite size and spherulite size distribution on the locations of lamellar opening can be illustrated by the correlation of yield stress with the corresponding spherulite size as shown in Figure 1.13. A maximum yield stress appearing at a certain spherulite size can be interpreted as the resultant effect of intra-spherulitic and inter-spherulitic deformation [24]. The yield point represents the occurrence of fracture in the microstructure. In smaller spherulites, the deformation pattern is in the regime of intra-

spherulitic deformation. The yield stress in this regime represents the occurrence of lamellar breaking. The increasing yield stress with spherulite size is due to the stronger lamellar structure in the spherulites. On the other hand, the spherulite boundaries are also becoming weaker with an increasing spherulite size, which favors the occurrence of inter-spherulitic deformation. The occurrence of a maximum yield stress indicates that the deformation pattern shifts from intra-spherulitic to inter-spherulitic in the spherulitic sample.

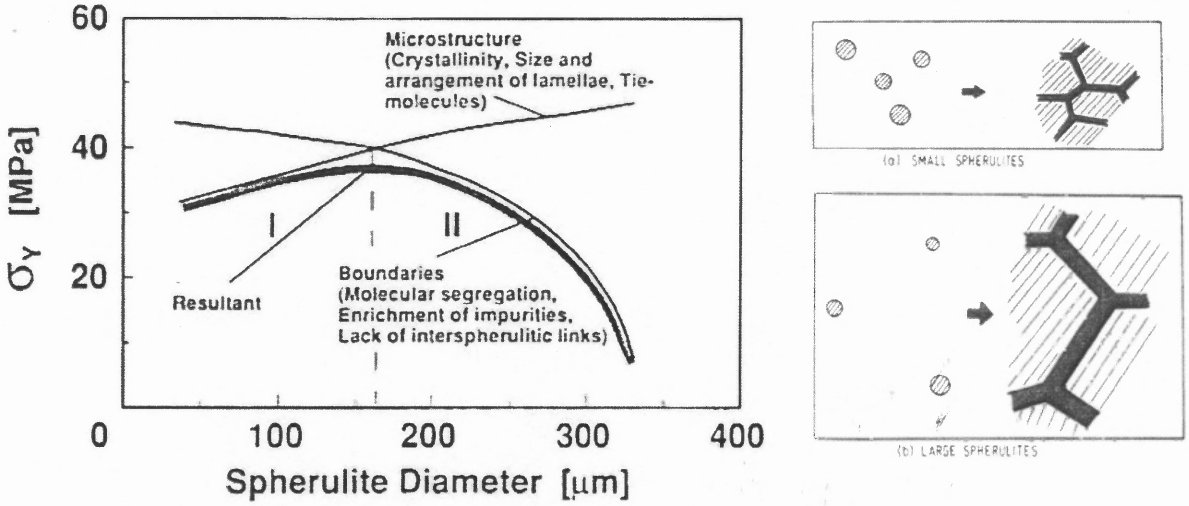

Figure 1.13 Schematic explanations for spherulitic irregularity. Region I represents the occurrence of intra-spherulitic deformation, and region II represents the occurrence of inter-spherulitic deformation [14].

So far, the spherulitic structure seems incapable of being utilized for membrane fabrication. The non-oriented lamellar morphology with various spherulite sizes are the major restrictions for that. However, the idea of using the spherulitic structure might become practical by changing the morphology of the lamellae. In the Celgard® process, this is done by rearranging the lamellar morphology (from spherulites to row lamellae). An alternative method is to change the lamellar morphology itself within a spherulitic structure. This seems an impossible task for most of the polymers, since the lamellar growth direction is always

radial. However, this modification could be achieved by utilizing polypropylene with α-form crystal structure. α-PP has a unique lamellar pattern among other polymers; it is a cross-hatched lamellar morphology composed of radial and tangential lamellae as shown in Figure 1.14(a). There are some important features of this mesh-like lamellar pattern that could be utilized for the fabrication of porous structures.

Firstly, the presence of tangential lamellae strengthens the spherulitic structure. This can limit the occurrence of catastrophic intra-spherulitic deformation which leads to an uncontrollable formation of a fibrillar morphology after cold drawing. Inter-spherulitic deformation leads to a desirable deformed pattern since in this case interconnectivity can be created easily by the pre-connected spherulite boundaries. Secondly, tangential lamellae provide extra restraints for the openings created during deformation. As shown in Figure 1.14(b), the residual mesh-like lamellae at a separated spherulite boundary show a web-like porous structure. Finally, the membrane fabricated via spherulitic deformation should have better mechanical strength in all directions due to the radially aligned lamellae.

On the other hand, it is known that annealing can enhance crystalline structure by allowing chain rearrangement with a temperature close to the melting temperature. Annealing could be important in this study, since both lamellae (R-lamellae and T-lamellae) can be strengthened and create stronger spherulites. These concepts are summarized in Figure 1.15.

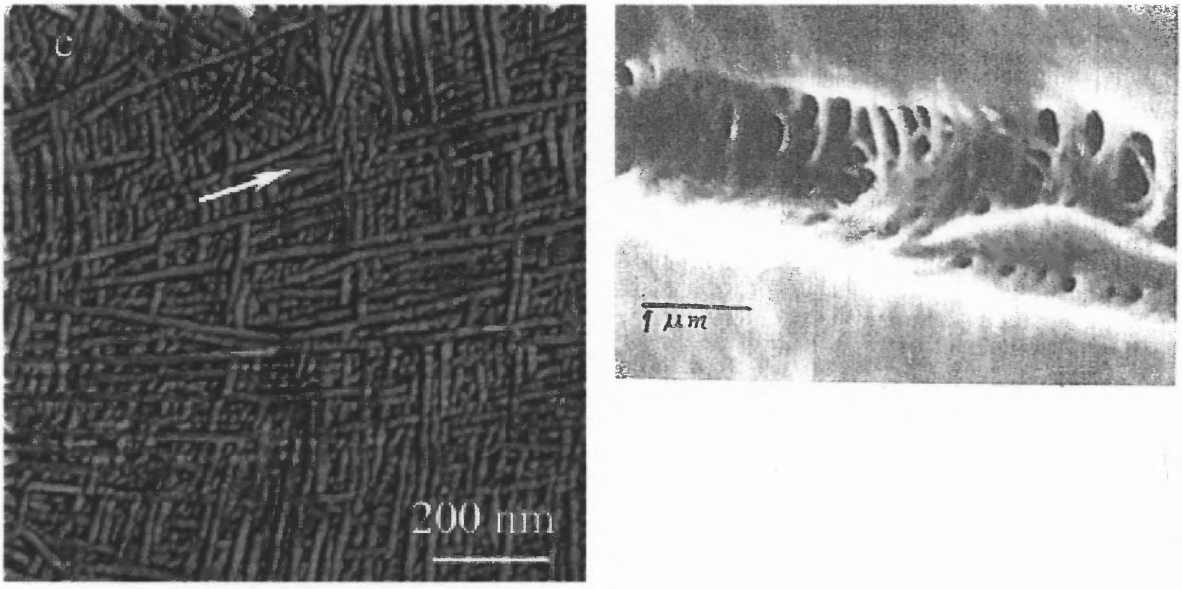

(a) (b)

Figure 1.14 Electron microscope images of mesh-like lamellae morphology in α-PP: (a) inside a spherulite [25], (b) at a separated spherulite boundary [26].

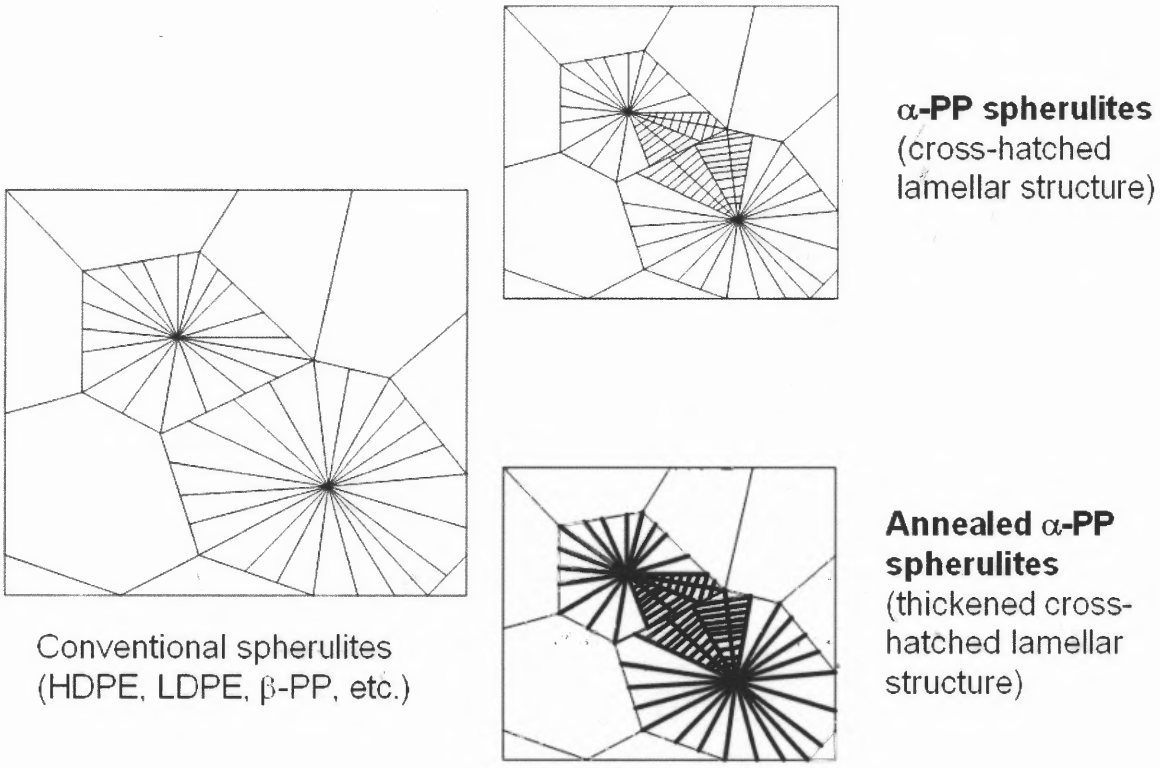

Figure 1.15 Schematic explanation of a possible membrane fabrication process based on strengthened α-PP lamellar morphology.

1.5 A Review of Polypropylene Microstructure

An important task for demonstrating the feasibility of this potential membrane fabrication process is to generate spherulites with strong lamellar structures to prevent catastrophic micronecking after the material yields. α-PP with its exceptional cross-hatched lamellar morphology as shown in Figure 1.16(a) seems to be a suitable candidate. A brief summary of this unique property of polypropylene is presented below.

From the perspective of polymer chain configuration, polypropylene has the simplest repeat unit (with the exception of polyethylene), and yet possesses several crystallographic forms. Polypropylene became an important commercial polymer after the invention of Ziegler-Natta catalysts in 1950s, which can produce highly stereoregular configurations [27]. Nowadays, with the improvement of catalysts, the commercially available polypropylene grades usually show a very high fraction of isotacticity; therefore, the term "PP" refers to isotactic polypropylene only in the following discussion.

The crystal forms of PP are quite complicated and highly dependent on the processing conditions [28, 29]. PP possesses four crystal forms: α-form, β-form, γ-form, and smectic form [30]. All of these forms involve the same 3_1-helix conformation as shown in Figure 1.16, but pack differently when folded into lamellae. Each form can be recognized by its well-defined Wide Angle W-ray Scattering (WAXS) pattern. The most common crystalline form encountered in conventional processing conditions is the α-form. The β-form can be found in some specific processing temperature ranges, or initiated by β-form nucleating agents [31]. The γ-form is obtained for the PP of high molecular weight [32] or crystallized under high pressure [33]. The smectic form is a transition crystallographic state found under very rapid cooling [34, 35], and transforms into the α-form at elevated temperatures [36, 37].

The crystallographic forms and their WAXS spectra are shown in Figure 1.17. Usually, quantification of these various crystallographic forms can be conducted based on the intensity of characteristic peaks from WAXS spectra according to Turner-Jones [38].

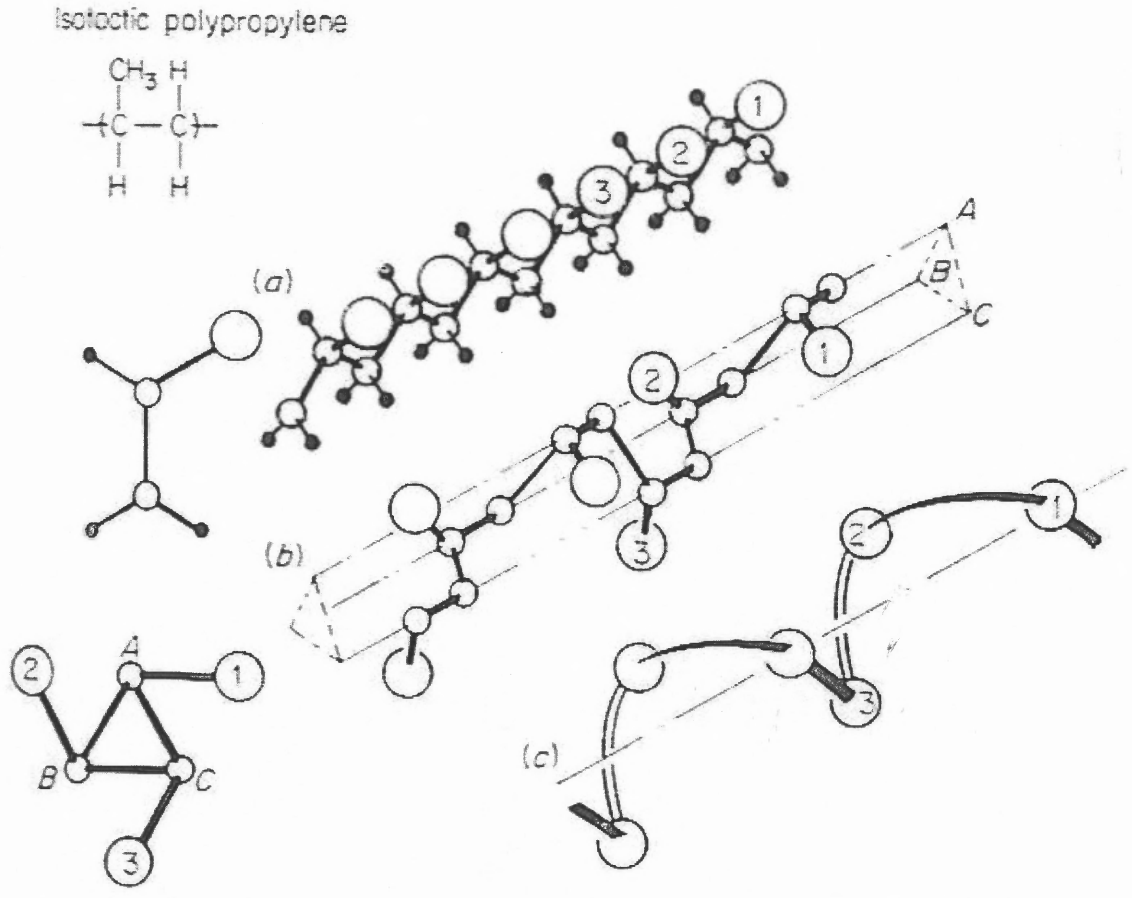

Figure 1.16 (a) Isotactic Polypropylene, (b) The 3_1-helix, (c) The 3_1-helix with only showing methyl groups [39].

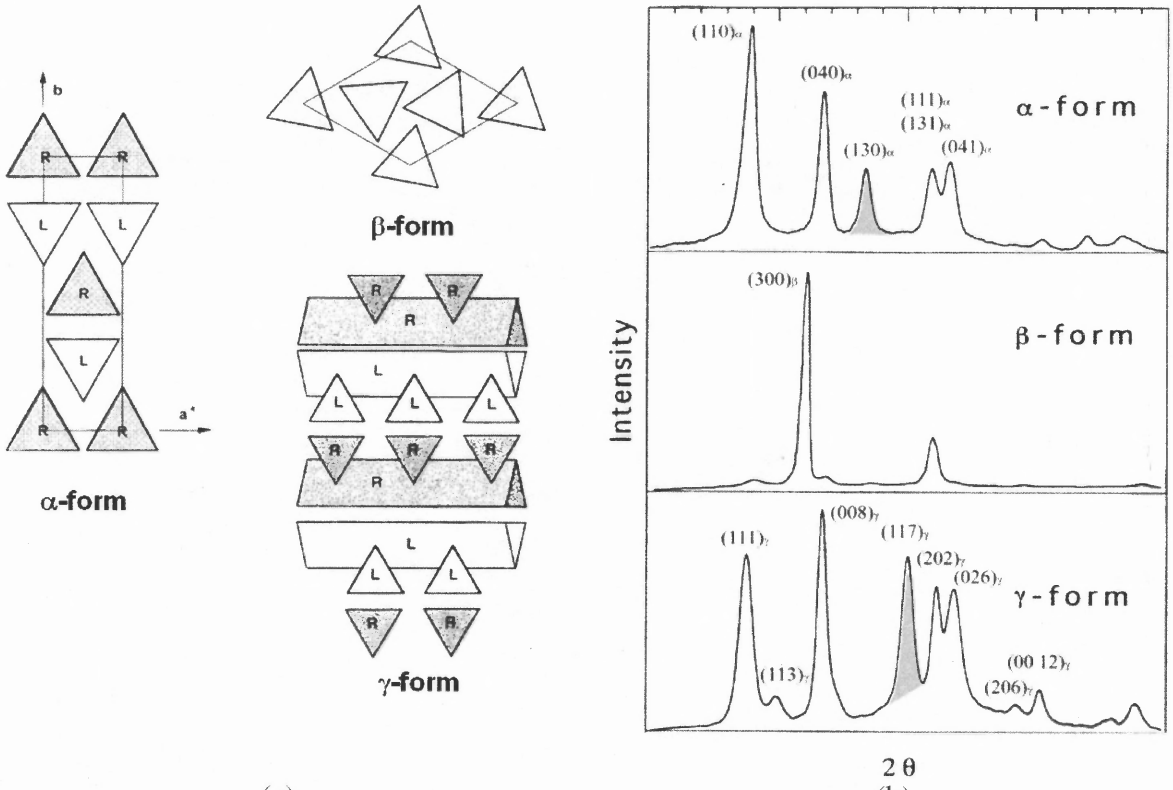

Figure 1.17 Three different crystallographic forms of PP: (a) lamellar packing morphology [40], (b) WAXS spectra (characteristic peaks are marked with shadow) [41].

The α-form has a monoclinic unit cell with parameters: a = 6.65 Å, b = 20.96 Å, c = 6.5 Å, β = 99°80 [29]. The significant peaks of the α-form can be found at the scattering angles 2θ of α_1: 14.1°(110), α_2: 16.9°(040), α_3: 18.5°(130), and a lumped α_4: (21.3°(111) 21.8°(131) 21.9°(041)). The α-form is the most stable and frequently encountered crystal form of PP. The cross-hatched lamellar morphology of radial lamellae (R-lamellae) and tangential lamellae (T-lamellae) is due to the small mismatch between the a- and c-axis unit cell parameters [42-44]. The spherulitic characteristics of the α-form are complicated due to this distinct lamellar feature. The birefringence sign of α-form spherulites can be positive, negative or mixed depending on the sample thermal history [45]. High temperature enhances the formation of an R-lamellae predominant spherulite. The T-lamellae predominant

spherulite shows a positive sign of birefringence and is less deformable [46]. With the aid of this interlocking morphology the α-form spherulites are more rigid and appear capable of maintaining their spherulitic morphology upon stressing [47]. As a result, a sample with a α-form spherulites also appears to be more brittle and vulnerable to impact [48]. The occurrence of branched lamellar morphology is evident in Figure 1.18(a). The T-lamellae are branching from the R-lamellae during crystallization. The model of this branching morphology shows that the a-c plane of the T-lamellae is growing on top of the a-c plane with a branching angle of 80° [40].

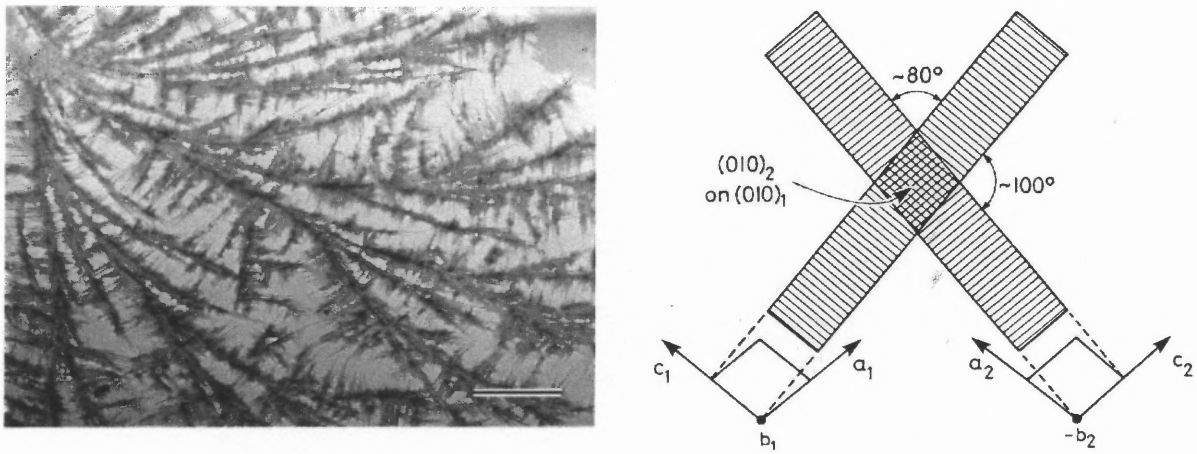

(a) (b)

Figure 1.18 (a) Electron microscope image of α-PP with an evident R-lamellae and T-lamellae morphology. (b) Model for the branching characteristics of R-lamellae and T-lamellae [40].

The β-form has a hexagonal unit cell. The β-form is thermally unstable with a melting temperature of 152 °C, and can transform to the α-form at elevated temperature or under stress [31, 49]. The β-form is known for its ductile response compared to the α-form [50, 51]. The difference in their mechanical behavior can be understood from their microstructural features. The spherulitic characteristics of the β-form resemble those of

conventional spherulites, such as a sheaf-like lamellar pattern and a negative sign of birefringence. On the other hand, the α-form with the presence of T-lamellae improves the strength of spherulites by acting like "knots" and providing anchor spots when the spherulites deform. A typical lamellar separation in the β-form spherulite is shown in Figure 1.19(a). A clear β-to-α transition due to the localized melting effect is shown in Figure 1.19(b) [52].

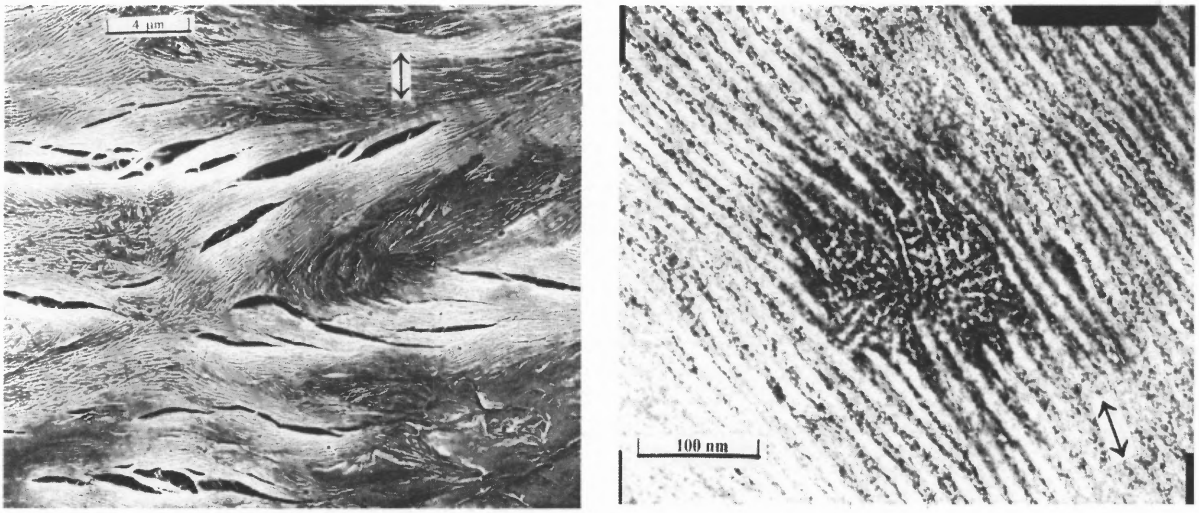

(a) (b)

Figure 1.19 (a) Lamellar separation in the β-form spherulites. The conventional sheaf-like lamellar morphology is evident. (b) A β-to-α transition with a clear lamellar morphology transformation [52].

The γ-form has a triclinic unit cell and is believed to be associated with the formation of the α-form due to its tilting lamellar angle [53-55]. Since it is seldom encountered under traditional processing conditions, there are only few reports on the lamellar and spherulitic characteristics of the γ-form. The smectic form represents a state of order intermediate between amorphous and crystalline states. The smectic-to-α form transition can be characterized with an apparent exotherm at a temperature from 65 to 120 °C in DSC scans

[37]. The smectic form has a nodular-like structure of the order of 10 to 30 nm, and shows a ductile behavior due to the lack of crystallinity [34].

1.6 Potential Modifications of the Novel Membrane Fabrication Process

There may be two potential modifications to the proposed novel membrane fabrication process in order to improve the membrane performance. The first modification (modification I) is to reduce the spherulite size by using nucleated polypropylene. It is known that the spherulite size of polypropylene can be dramatically reduced by adding nucleating agents as shown in Figure 1.20. Some very effective nucleating agents are called "clarifying agents" since a highly transparent film can be produced as a result of the presence of very fine spherulites (less than 1 μm in size) [56].

Nucleated polypropylene also shows better mechanical properties due to the more uniform sized spherulites initiated simultaneously from a very large amount of nucleating sites during crystallization [57]. The α-form and β-form lamellar characteristics of polypropylene can be preserved by the choice of appropriate nucleating agents without a change of the crystallization process [58]. Thus, the use of nucleated polypropylene provides an excellent strategy to improve the performance of the porous membranes via spherulitic deformations. The porosity and interconnectivity of the membranes should increase with a decreasing spherulite size.

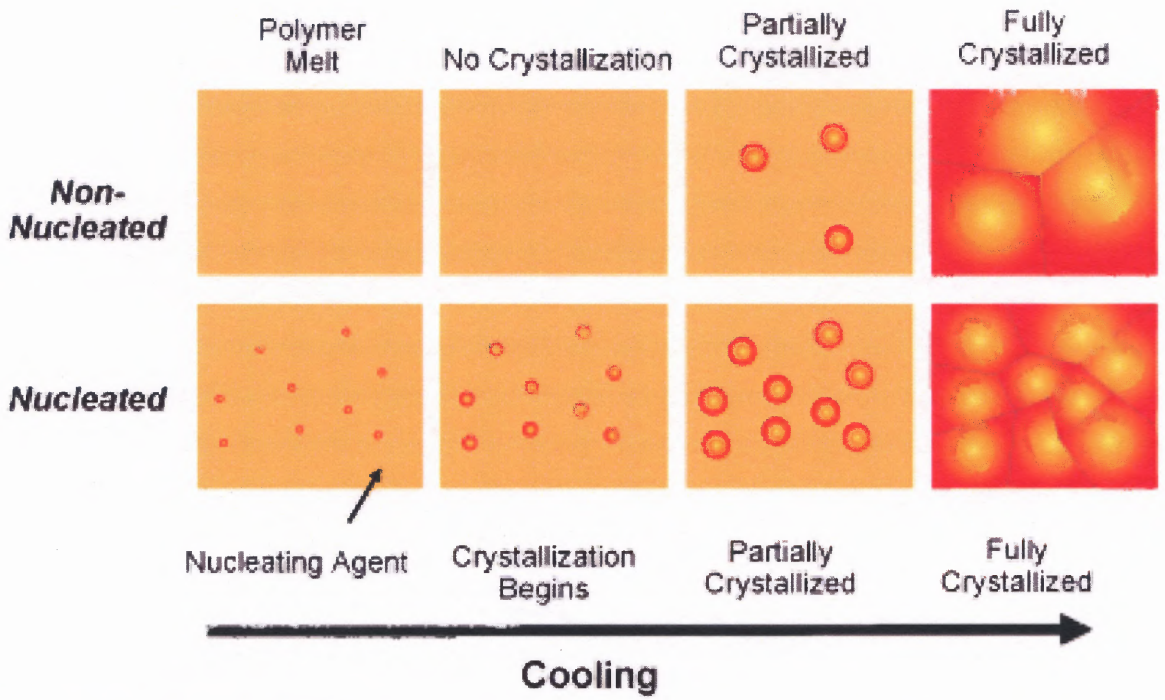

Figure 1.20 Potential modification I: the use of nucleated polypropylene (image from Milliken Chemical).

The second modification (modification II) is to utilize interfacial debonding between two different phases to enhance permeability. The debonded structure could be created by using an immiscible polymer blend system or a polymer containing fillers [59-61]. It is known that mechanical properties of polymers can be improved by adding a second component such as fillers or rubbers. A debonded morphology around the dispersed phase (the second component) is often found after the sample deformed. Debonding is a matrix yielding phenomenon due to the poor adhesion between matrix and dispersed phases. This debonded morphology can be utilized as a permeation shortcut for improving membrane permeability. A debonded morphology in a PP/$CaCO_3$ composite is shown in Figure 1.21.

A good choice for the second component is a polymeric material which is immiscible with the polypropylene matrix and can be broken down easily in distinct dispersed domains by conventional compounding processes. A good dispersion can be achieved by selecting an

immiscible blend system whose components have similar rheological properties. The concept in the modification II is similar to that in the MMMs (Figure 1.3); however, the occurrence of percolation threshold needs to be prevented. A percolated debonded morphology is of no use for fabricating a membrane with a confined pore size. A porous matrix region between the debonded openings (Figure 1.21) has to be maintained to ensure the control of pore size.

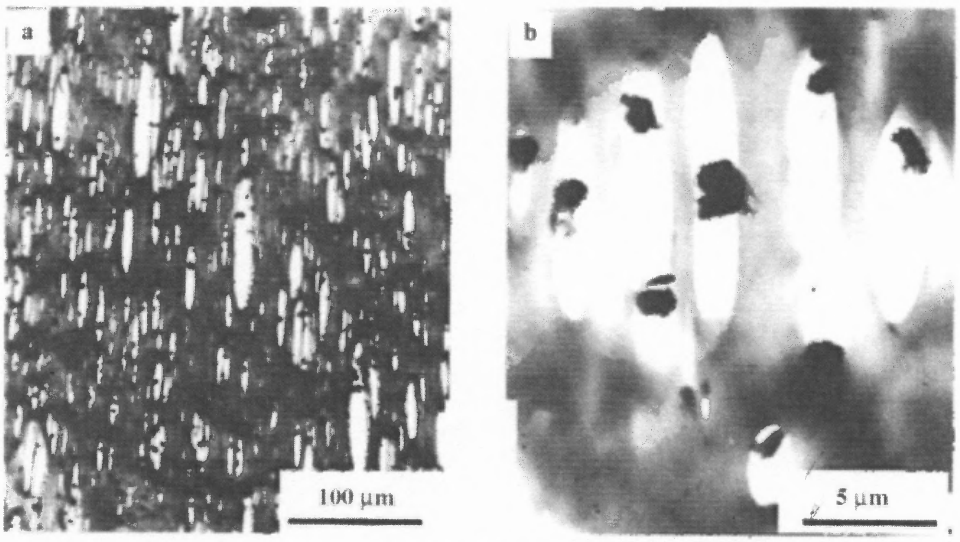

Figure 1.21 Debonded morphology of PP/$CaCO_3$ composite [61].

1.7 Scope of the Thesis

The purpose of this study is to investigate the feasibility of creating porous structures in semicrystalline polymers via inter- and intra-spherulitic deformations. Isotactic polypropylene is selected because of its unique cross-hatched lamellar structure. A parametric study of extrusion, annealing, and stretching conditions is reported. The concept is further expanded by utilizing nucleated polypropylene to reduce spherulite size and a second immiscible polymer phase. The novel porous membranes are characterized morphologically and the pore interconnectivity is examined via methanol permeability.

CHAPTER 2

EXPERIMENTAL

2.1 Materials

A film extrusion grade polypropylene (PP), Dow H314-02Z, is used in this study. It is a homopolymer with a reported density of 0.9 g/cm^3 and MFR (melt flow rate) of 2 g/10 min. A nucleated polypropylene (PPN), Dow H110-02N, with material properties similar to PP is also used for modification I. A polystyrene (PS), Dow 685D, is used to create the immiscible blend system for modification II. The properties of the materials are listed in Table 2.1.

Table 2.1 Material Properties

Polymer	Grade	Source	Density (g/cm^3)	T_g (°C)	T_m (°C)	T_c (°C)	Melt Flow Rate (g/10min)
Polypropylene (PP)	H314-02Z	Dow	0.9	-5	162	115	2.0 (230 °C, 2.16 kg)
Nucleated Polypropylene (PPN)	H110-02N	Dow	0.9	-2	159	130	2.0 (230 °C, 2.16 kg)
Polystyrene (PS)	685D	Dow	1.04	100	NA	NA	1.5 (200 °C, 5 kg)

2.2 Melt Processing and Post Treatments

2.2.1 Precursor Film Extrusion

The precursor films were extruded through a Brabender single screw extruder (D = 0.75 inch, L/D = 15) equipped with a 15-cm sheet die. The extrusion conditions were selected to ensure the formation of spherulitic structures instead of stacked row lamellar structures in the

precursor films. The temperature setting of the extruder was 230 °C, the extrusion speed was 30 rpm, and the die-lip gap was fixed at 100 μm. Take-up rolls were used to collect the extruded film. The roll temperature was maintained at 90 °C by a circulating water bath. The distance between the extrusion die and the collecting roll was kept at 2.5 cm. The take-up speed was kept low to avoid generating additional orientation in the precursor films. The thickness of the precursor films was about 70 μm. The experimental setup is shown in Figure 2.1.

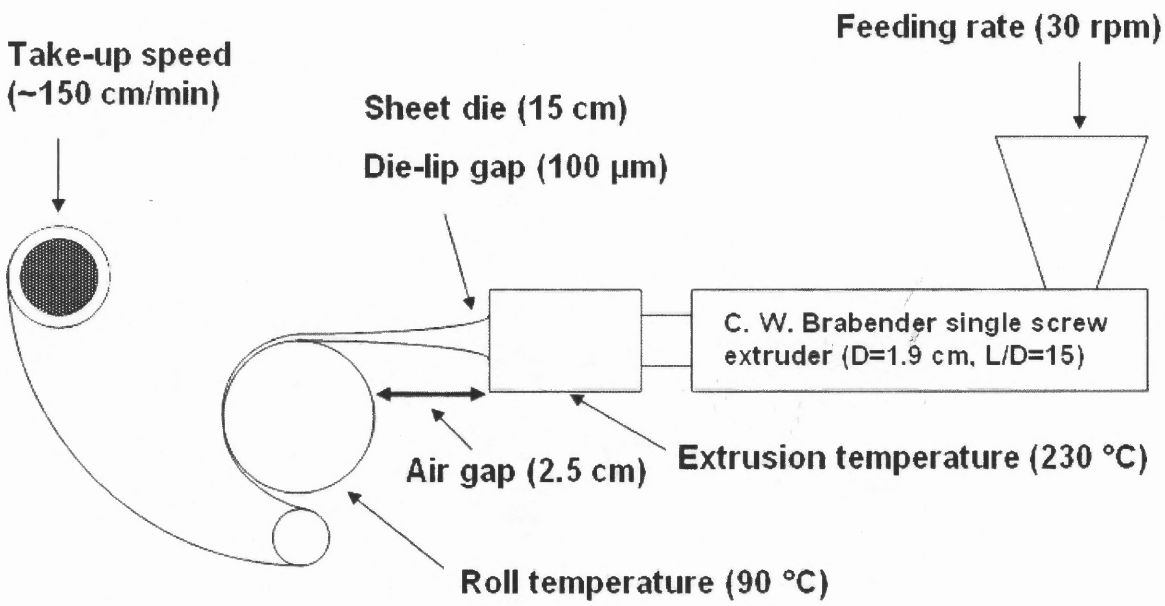

Figure 2.1 Experimental setup for preparation of precursor films via Single Screw Extruder and take-up rolls.

2.2.2 Annealing

The precursor films were annealed in an air-circulating oven for 2 hours. A long annealing time was selected to ensure that a steady temperature was reached. The annealing temperatures were set at 100 °C, 120 °C, and 140 °C. The appearance and thermal analysis

results of the annealed samples showed no signs of degradation. Samples designated as (An 100C), (An 120C), etc. indicate annealing at 100 °C, 120 °C, etc.

2.2.3 Uniaxial Stretching

A Tinius Olsen LOCAP universal testing machine equipped with a temperature control chamber was used for the stretching step. The non-annealed and annealed precursor films were cut as 7.6-cm wide rectangular sheets before stretching. The stretching direction was parallel to the extrusion direction, which is designated as the machine direction (MD). The films were held between two air-pressurized clamps with an initial distance between the clamps of 2.5 cm. The stretching rates (R_S) ranged from 0.25 cm/min to 50.8 cm/min. The extension ratios (E_S) of the films ranged from 100% (from the original length) to 600%. The stretching temperatures (T_S) were chosen as -20 °C, 25 °C, and 70 °C. Most of the samples were stretched as R_S = 12.7 cm/min, E_S = 200%, and T_S = 25 °C. The stretched membranes were then held under tension at 90 °C for 10 minutes followed by cooling down to 25 °C for 20 minutes to stabilize the structure. The final membrane thickness was about 10 to 35 μm.

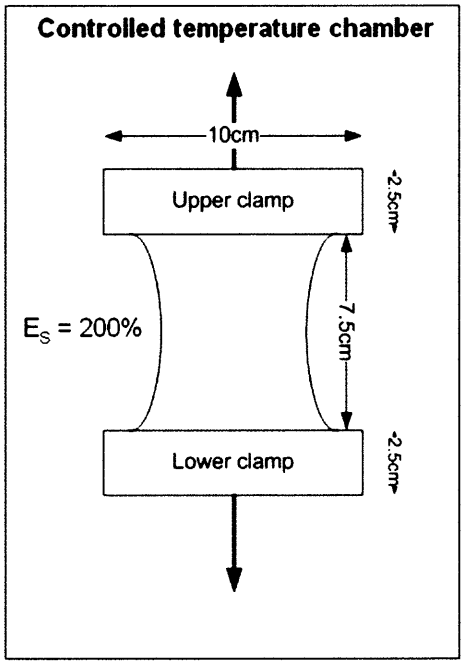

Figure 2.2 Experimental setup for preparation of stretched membranes via Tinius Olsen LOCAP universal testing machine equipped with a temperature control chamber.

2.2.4 Immiscible Blend Preparation

A PP/PS immiscible blend was prepared by compounding in a twin screw extruder. Polystyrene was chosen as the second component to regulate the stress level of the precursor films during stretching. The PP/PS 90/10 mixture was dry blended before being fed into a ZSK 30 W&P co-rotating intermeshing twin screw extruder with screws consisting of conveying elements, kneading blocks and two mixing sections. The feeding rate was 5.45 kg/hr, and the extruder was operated at 120 rpm. The barrel temperatures of the extruder were set at 230 °C except for the feeding zone (180 °C) [60]. These extrusion conditions were chosen in order to correspond to a unity viscosity ratio between PP and PS. The compounded blend was extruded as a strand and immediately passed through a water cooling bath. The cooling water temperature was kept around 40 °C. Then, the extrudate was pelletized and the pellets were dried at 80 °C at least overnight to remove any moisture

before the membrane fabrication process. The PPN/PS 90/10 immiscible blend was prepared under the same conditions due to the similar rheological properties of PPN to PP.

2.3 Characterization

2.3.1 Polarized Optical Microscope

Precursor films were analyzed using a Zeiss polarizing optical microscope. For birefringence measurements, a first order retardation λ-plate was inserted between the polarizers. The image was collected by a Zeiss image adapter and recorded on the computer.

2.3.2 Scanning Electron Microscope

The SEM images were obtained by a Leo 1530 VP field emission scanning electron microscope (FESEM). In order to prevent charge accumulation on the sample surface during examination, all samples were pre-coated with a thin layer of gold/palladium alloy.

2.3.3 Atomic Force Microscope

AFM experiments were conducted on a Nanoscope III scanning force microscope (Digital Instruments). The Tapping™ mode was used for mapping the surface morphology of the precursor films.

2.3.4 Wide Angle X-ray Scattering

The wide angle X-ray scattering pattern of the films was recorded by a Philips PW3040 X-ray Diffractometer with a Cu-K_α radiation (λ = 1.54 Å) and a 2θ range from 10° to 24°.

2.3.5 Differential Scanning Calorimetry

DSC tests of the precursor films were carried out on a TA instrument Q100 with sample weight of about 5 mg. For melting temperature measurements, the heating rate was 10 °C/min and the scan range was from -50 °C to 200 °C. For crystallization temperature measurements, the samples were first kept isothermally at 230 °C for 10 minutes to erase their thermal history and then cooled down to 25 °C at 10 °C/min. The crystallinity of the sample was calculated from enthalpy change values obtained in the heating curve, and by assuming 209 J/g as the heat of fusion of a 100% crystalline sample [27].

2.3.6 Methanol Permeation Test

Methanol permeation tests were performed in a pressurized permeation cell having a testing area of 1.77 cm^2. All samples were tested one week after preparation to avoid possible interference from aging effects. The vessel was pressurized by nitrogen at 0.41 MPa. Samples were pre-wetted with methanol for 10 minutes before testing. The permeated methanol was collected in a graduated cylinder, hourly, for three hours since the first drop appeared on the collecting tube. The methanol flux was determined from permeation data collected within the second hour.

2.3.7 Porosity Determination

The porosity (ε) of the stretched membranes was calculated from the following equations;

$$\rho_{cal} = \rho_c \chi_c + \rho_a (1 - \chi_c) \tag{2.1}$$

$$V_{cal} = M_M / \rho_{cal} \tag{2.2}$$

$$\varepsilon = \frac{V_M - V_{cal}}{V_{cal}} \tag{2.3}$$

Here ρ_{cal} is the calculated density of the stretched membrane based on its fractional crystallinity (χ_c) obtained from the DSC heating scan; ρ_c is the density of crystalline region taken as 0.946 g/cm^3; ρ_a is the density of the amorphous region taken as 0.855 g/cm^3 [27]; V_{cal} is the calculated volume of a stretched membrane of measured mass M_M and density ρ_{cal}, V_M is the measured volume of the stretched membrane with an area of 17.8 cm^2 and its measured thickness. The quantity ε can be therefore obtained from the difference of V_{cal} and V_M divided by V_{cal}.

CHAPTER 3

RESULTS AND DISCUSSION

3.1 Effect of Extrusion and Annealing Conditions on PP Precursor Films

3.1.1 Effect of Extrusion Conditions

A series of tests to determine the appropriate precursor film extrusion conditions were conducted first. It was found that low-stress extrusion conditions can ensure the reproducibility of the spherulitic structure, and produce an even-surface precursor film for stretching. The SEM image of the precursor film extruded at high stress conditions which resembles the Celgard® process is shown in Figure 3.1. An obvious stacked row lamellar structure is observed on the surface of this precursor film. The extrusion conditions of this film were used as reference for creating precursor films with spherulitic features.

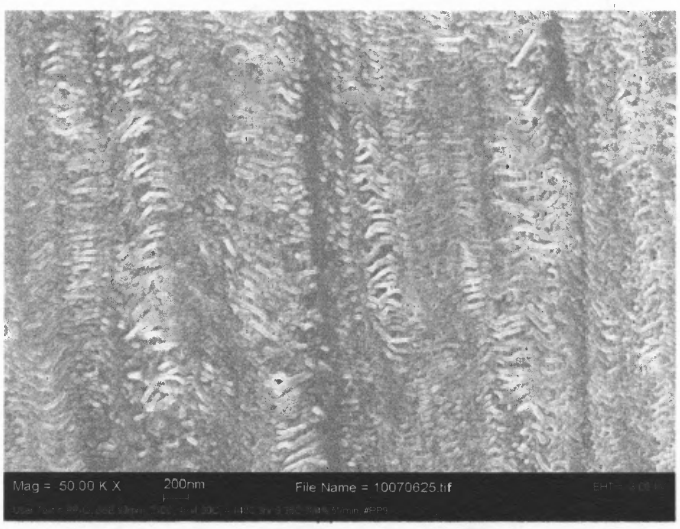

Figure 3.1 SEM image of the surface of PP precursor film produced at high stress extrusion conditions.

The spherulitic morphology of the precursor films, F-PP ("F" is used to designate precursor films), produced at low stress extrusion conditions can be characterized by the use

of optical microscope, since the spherulite sizes are in the range of observation. This examination was conducted on both sides (air-side and roll-side) of the F-PP sample, and the results are shown in Figure 3.2. The difference between these two sides is in the cooling rate. The temperature of the air-side is about 25 °C. The roll-side is in contact with the rolls where the temperature of 90 °C is controlled by circulating water. The surface of roll-side shows cross dark lines due to the rough surface of the rolls (Figure 3.2(a)). The surface of the air-side shows granular-like morphology with a size about 10 μm (Figure 3.2(b)). The granular-like morphology on the roll-side is not evident due to the dark-strips.

In fact, the spherulitic morphology of the precursor film F-PP can be identified from both surfaces by the presence of a Maltese cross pattern shown in Figure 3.2 (c) and (d). The size of the spherulites in the precursor films was about 10 μm, and their presence confirms the choice of the applied extrusion conditions. The birefringence properties of PP can provide additional important information besides a spherulitic morphology related to the presence of T-lamellae. A brief explanation is as follows:

The formation of a Maltese cross pattern is due to the birefringence properties of the lamellae in the spherulites. Birefringence properties represent the anisotropic refractive index (n) in the material. In semicrystalline polymer, the optical properties along the polymer chain (c-axis) are quite different from those normal to the chain. For example, in polyethylene, n_a = 1.514, n_b = 1.519, n_c = 1.575 [62]. Therefore, many polymers can be considered as an uniaxial medium which can be represented as a prolate ellipsoid uniaxial indicatrix as shown in Figure 3.3(a). (For an isotropic medium, the indicatrix appears to be a sphere.) The long axis in the prolate ellipsoid represents the c-axis due to the high refractive index from dense packing of chains [11].

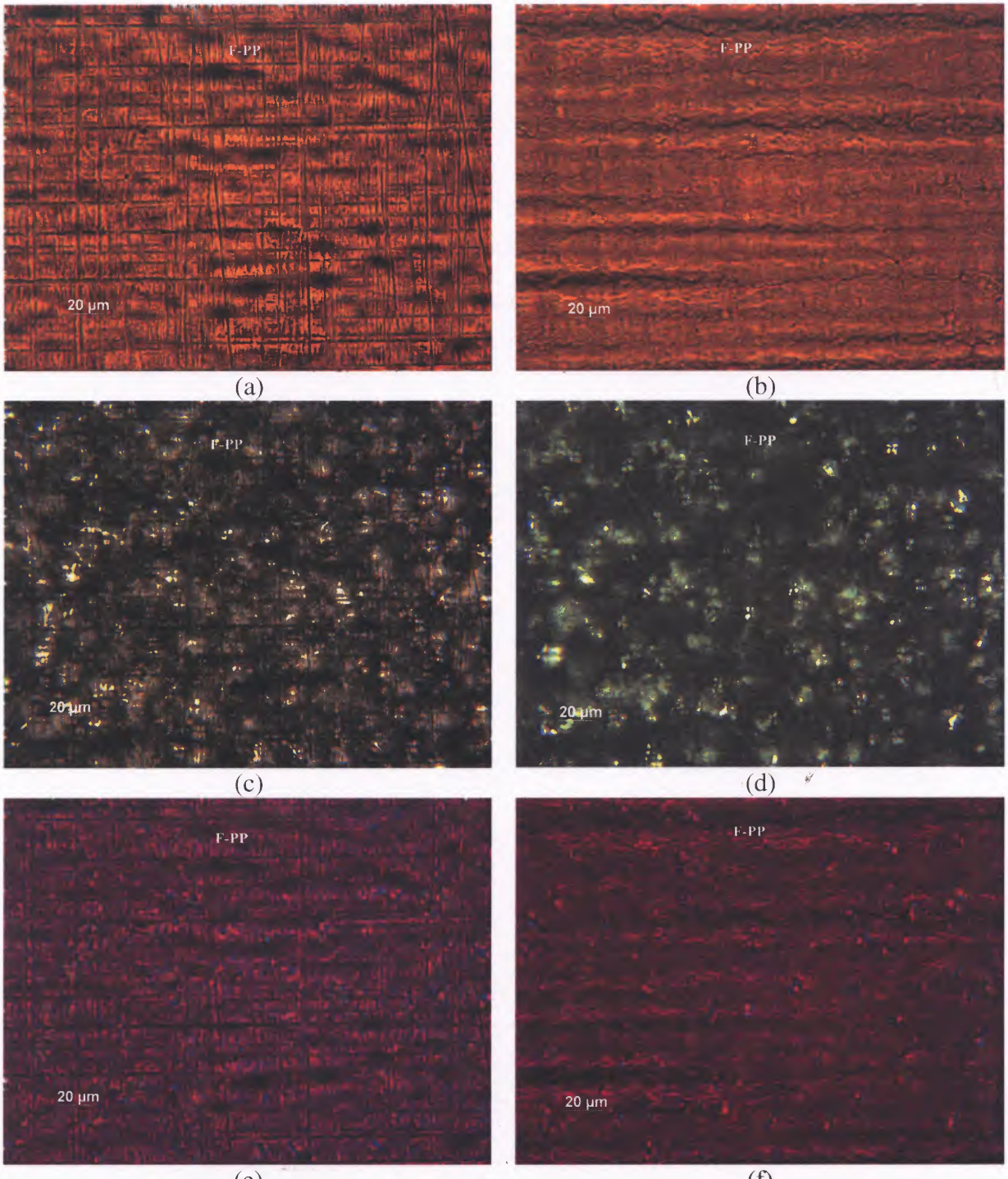

Figure 3.2 Images of spherulites produced at low stress conditions (F-PP): (a), (b) optical microscope images; (c), (d) polarized optical microscope images; (e), (f) polarized optical microscope images with a first order λ-plate. (roll-side (a) (c) (e) and air-side (b) (d) (f))

In polarized optical microscopy, the incident beam from the light source is polarized by passing through polarizer. Since the analyzer (another polarizer) is placed perpendicular to the first polarizer, the intensity of the incident beam will be totally annihilated if the sample shows isotropic optical properties. On the contrary, the incident beam can go through the cross polarizers only when the sample has birefringence properties. Therefore, the circular Maltese cross pattern shown in Figure 3.2(c) and (d) is evidence of the existence of spherulites. The dark strips in the Maltese cross pattern represent the distinct directions of the cross polarizers. The alignment of the dark strips in the Maltese cross pattern and the cross polarization implies that the directions of the ellipsoid uniaxial indicatrices inside the spherulite could be tangential (case II in Figure 3.3(b)) or radial (case III in Figure 3.3(b)). The direction of the dark strips in the spherulites and the direction of the cross polarizers are not aligned in the case of a tilt ellipsoid indicatrix (case I in Figure 3.3(b)). Most polymers with radial growth lamellae exhibit the tangential aligned uniaxial indicatrices as in case II.

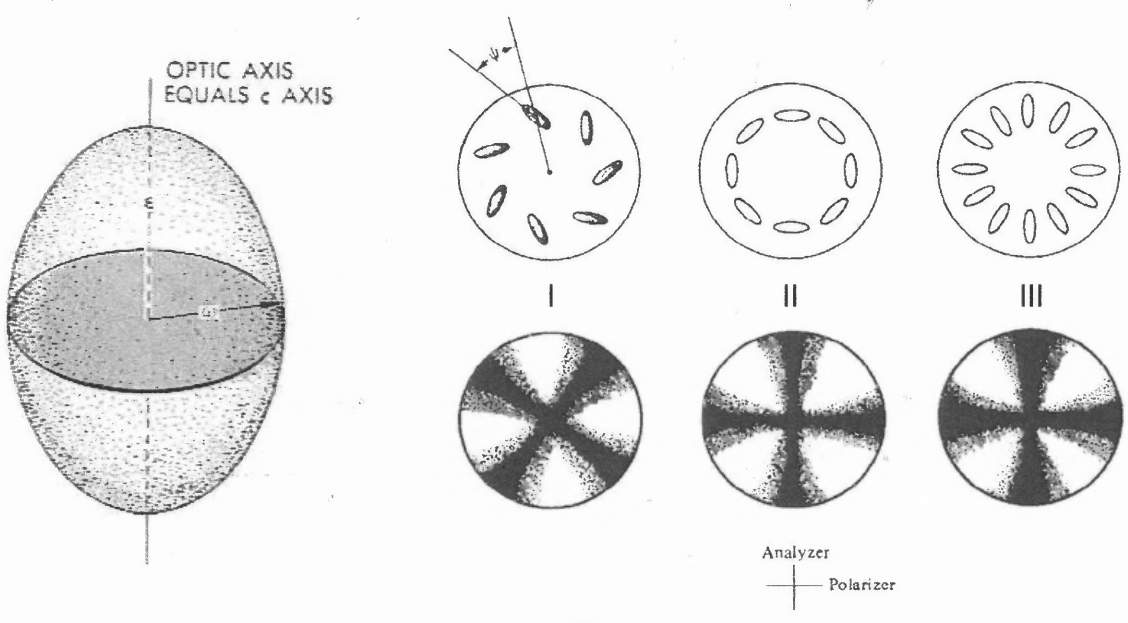

(a) (b)

Figure 3.3 Birefringence properties of spherulites: (a) prolate ellipsoid uniaxial indicatrix, (b) possible alignment for Maltese cross pattern [11].

The birefringence of a spherulite, Δ_s, is defined as $n_r - n_t$ where n_r is the refractive index parallel to the spherulite radius and n_t is the refractive index perpendicular to the radial direction [62]. If the amorphous phase can be assumed as an isotropic medium, Δ_s is only related to the orientation of the crystalline phase in the spherulites. Polymers with radial growth lamellae and tangentially aligned polymer chains (tangential aligned uniaxial indicatrices) show negative birefringence due to the larger n_t (c-axis). A convenient way to determine the birefringence sign is by observing the color change of the spherulite with the help of a sensitive tint plate. The plate is made of gypsum with a precise thickness of 565 nm, and is also called first order λ-plate. A sample of negative birefringence shows a color change with a second- and fourth-quadrant blue spherulite by inserting a first order λ-plate from 45° position as shown in Figure 3.4(a). The inserted first order λ-plate is used to create a path difference of the polarized incident beam, and the birefringence properties of the sample are amplified with a color change; the incident beam is a white light and a slightly shift on its wavelength can cause color changes.

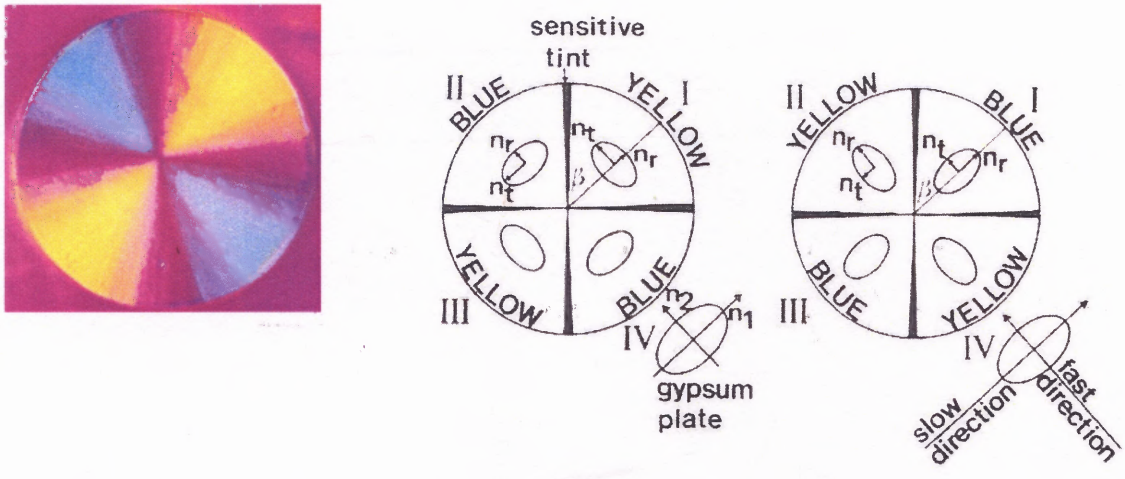

(a) (b)

Figure 3.4 Determination for birefringence signs: (a) a negative spherulite, (b) models for color change with inserting a first order λ-plate [62].

In the case of PP, the birefringence properties of spherulites can be quite interesting due to the presence of T-lamellae. Since T-lamellae are almost perpendicular to the R-lamellae (Figure 1.18(b)), the T-lamellae rich α-PP spherulite (case III in Figure 3.3(b)) shows a similar Maltese cross pattern as R-lamellae rich α-PP spherulite (case II in Figure 3.3(b)). Therefore, the Maltese cross pattern of the F-PP sample shown in Figure 3.2(c) and (d) can only provide the evidence of the existence of spherulitic morphology without the detail of T-lamellae.

The R-lamellae rich α-PP spherulite is similar to other conventional spherulites and exhibits negative birefringence with a second- and fourth-quadrant blue. On the other hand, a T-lamellae rich α-PP spherulite exhibits positive birefringence with a first- and third-quadrant blue as indicated in Figure 3.4(b). According to Norton and Keller [45], an α-spherulite shows positive birefringence sign when the fraction of T-lamellae is more than 1/3 of the total lamellae content. The birefringence properties of PP spherulites with varied crystallization temperature are shown in Table 3.1. They show a complicated formation of crystal forms with rich birefringence properties. The earlier studies were conducted by placing the sample on the hot stage where the sample thickness and temperature change were well-defined. The results might not be able to apply to the melt processing directly; however, the general principle should still be applicable to a film extrusion process.

Table 3.1 Difference Types of Polypropylene Spherulites [62]

type	Crystallographic form	Spherulite birefringence	Crystallization temperature range (°C)
I	α	Weakly positive	<134
II	α	Weakly negative	>138
Mixed	α	Mixed	134-138
III	β	Negative	110-128
IV	β	Negative	128-132

The birefringence property examination of the F-PP sample is shown in Figure 3.2(e) and (f). Interestingly, the spherulites near the surface of the roll-side exhibit a second- and fourth-quadrant blue (negative birefringence) (Figure 3.2(e)) and the spherulites near the surface of the air-side exhibit a first- and third-quadrant blue (positive birefringence) (Figure 3.2(f)). The thickness of the precursor film is about 70 μm and transition from negative to positive birefringence is close to the middle of the sample. In order to avoid the interference from the rough surface of the roll-side, morphological characterization focusing only on the surface of the air-side is useful for the following two reasons.

Firstly, it provides some estimation on the proportion of T-lamellae in the precursor film and can identify the spherulites located inside the film as a result of the transmission mode of the optical microscopy. Secondly, it provides guideline to the setup of the processing conditions for generating T-lamellae rich spherulites. However, these goals can only be achieved when the spherulite size is large enough for the optical microscope examination. The resolution of the observation is also limited by a small spherulite size due to the interference between each spherulite. This is the reason for the presence of the spherulitic morphology having features shown in Figure 3.2(c) and (d).

3.1.2 Effect of Annealing Conditions

The crystallographic configuration of isotactic polypropylene is quite complicated and is highly dependent on processing conditions. Isotactic polypropylene possesses four crystallographic forms: α-form, β-form, γ-form, and smectic form. Each form can be recognized by its well-defined WAXS patterns as shown in Figure 1.17(b). The WAXS spectrum of the F-PP (Figure 3.5(a)) shows a predominant α-form with some traceable amounts of the β-form (β_1: 16.1° (300) and β_2: 23.1° (221)). The absences of the γ-form and the smectic form are as expected since the γ-form can only be found by crystallization under very high pressure and the smectic form is generated under extremely fast cooling conditions.

The cross-hatched lamellar morphology of the F-PP sample is shown in the AFM image of Figure 3.5(b). Even though AFM can provide information of surface morphology without pre-treatment of the sample, it is often used on a sample with a relatively flat surface where the roughness is within a scale of nanometer. For the F-PP sample, the formation of 3-D spherulites generates a surface roughness of a micrometer scale and makes AFM a less desirable method for morphological characterization in this study.

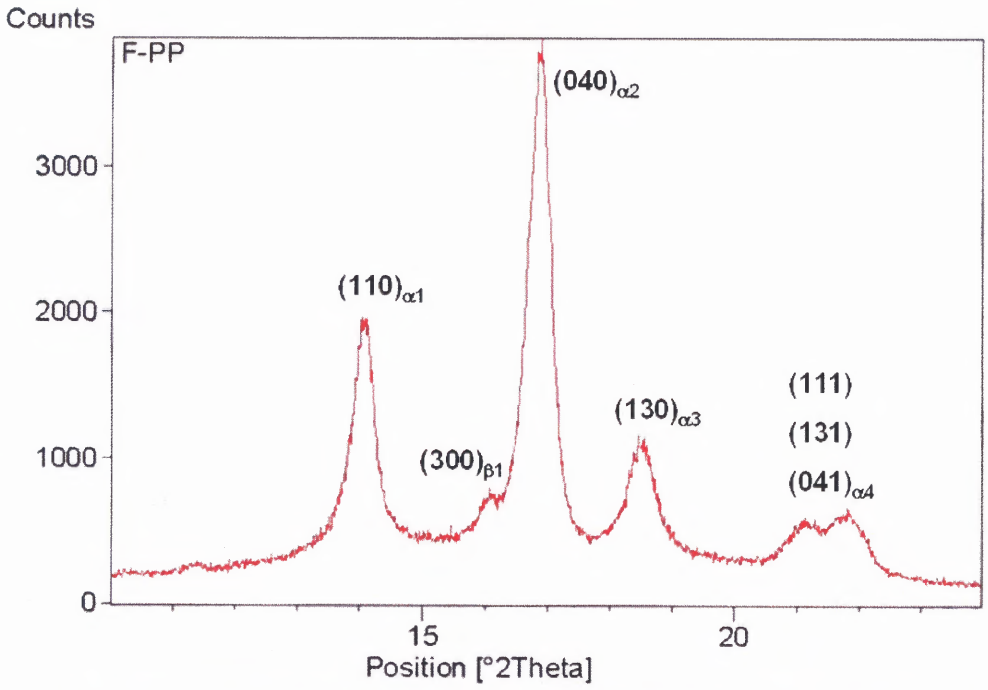

(a)

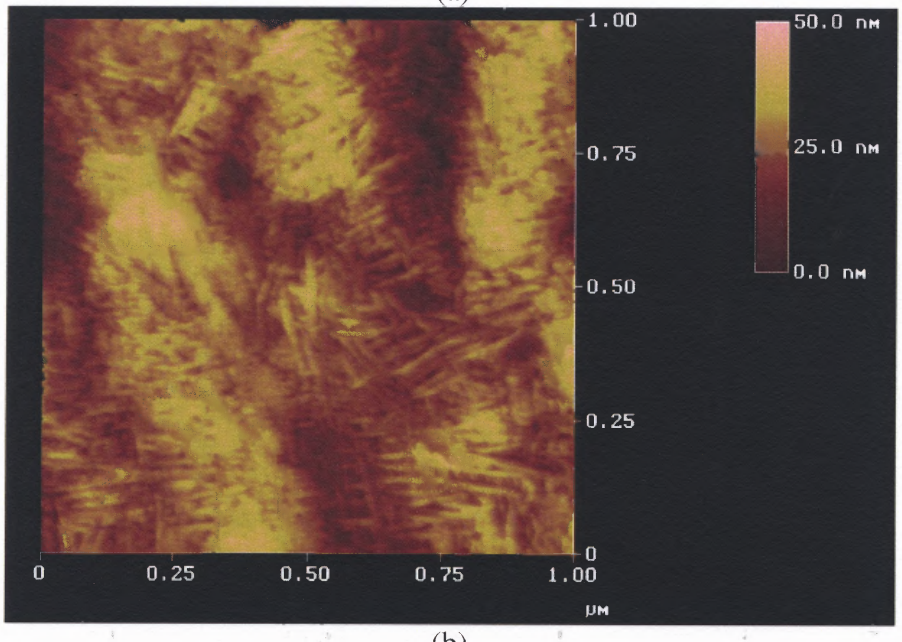

(b)

Figure 3.5 Crystallographic examination of non-annealed PP precursor film: (a) WAXS spectrum; (b) AFM image.

The WAXS spectra of the precursor films with or without annealing are shown in Figure 3.6. There was no significant change of the spectrum of the α-form by annealing. Annealing only improved the crystalline structure, which resulted in sharper and distinct

peaks. The traceable amount of β-form, the (300) peak, disappeared in the F-PP(An 140C) sample. Because the β-form is thermally and mechanically unstable, it transforms into the α-form by heating.

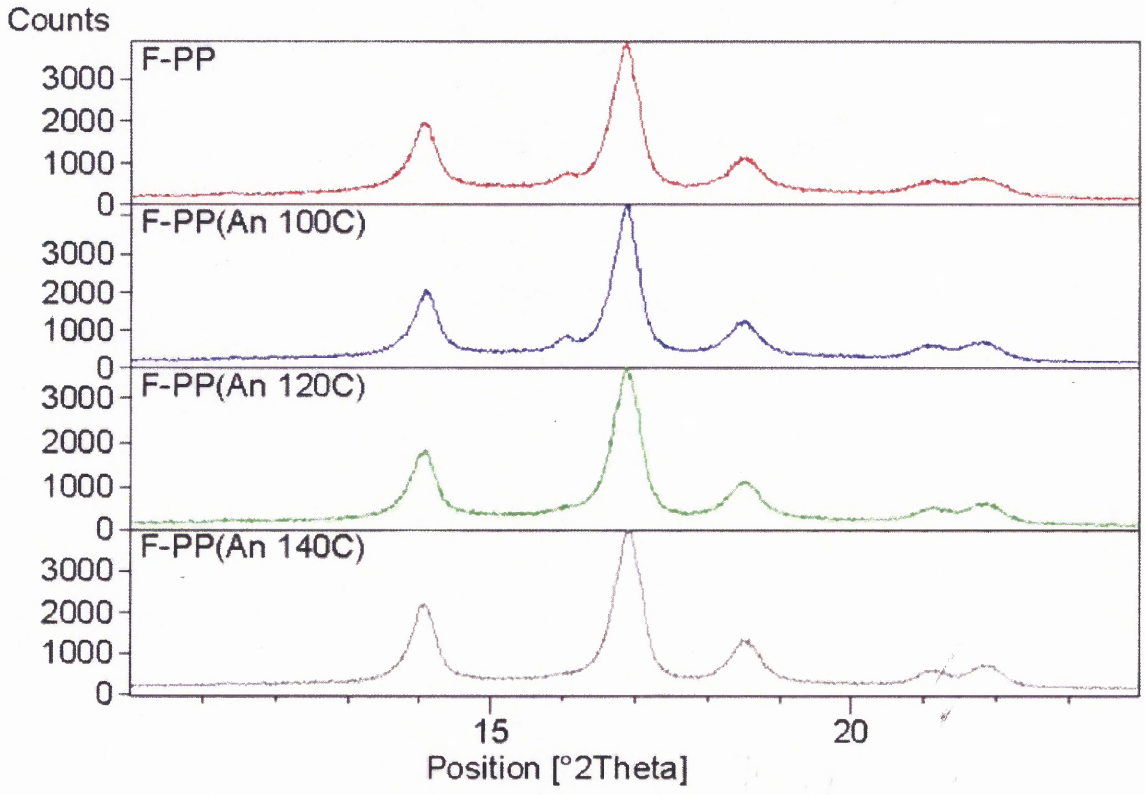

Figure 3.6 WAXS spectra of PP precursor films with or without annealing.

Figure 3.7 shows DSC heating curves of the PP precursor films with and without the annealing treatment. The results of melting temperatures and crystallinity of these samples are summarized in Table 3.2. The melting temperature of F-PP is about 162 °C which is typical for isotactic PP. Annealing changes very little the position of the melting peak. However, the area under the melting peak, an indication of crystallinity, increases with increasing annealing temperature as shown in Table 3.2. A characteristic discontinuity was observed in the thermograms of the annealed samples right before the melting peak.

There have been several studies on the multiple melting peak behavior of PP. Suggested explanations include the presence of β-form [50] or the recrystallization of imperfect crystals during the DSC heating scan [54]. The contribution of the β-form does not appear to be possible in this case because of its small amount as shown in Figure 3.6. The occurrence of β to α transition at a high annealing temperature, in sample F-PP(An 140C), also rules out the possible contribution of the β-form to this discontinuity.

An interesting feature is that the onset of this discontinuity can be related to the annealing temperature (Table 3.2). Similar observations have been reported by Poussin et al. [63] who studied the effect of thermal treatment on PP and suggested that the shoulder represents lamellae thickening during annealing. Alamo et al. [64] and Wu et al. [65] suggested that the low temperature discontinuity is due to the melting of the T-lamellae. In both studies, the appearance of negative birefringence spherulites (R-lamellae rich) was observed when the low temperature discontinuity disappeared. Therefore, the corresponding discontinuity in the annealed sample seems to imply the presence of thickened T-lamellae formed at the high annealing temperature. The thickness of the R-lamellae did not increase by annealing since there was no significant shift in the main melting peak.

Another distinct feature was found by analyzing the glass transition temperature of these samples. Actually, there were two endothermic discontinuities T_1 and T_2 at 0 °C and 40 °C in all samples (Figure 3.7, insert). The first one resembles the glass transition temperature of polypropylene which is about -5 °C, and the second one is not related to melting of the crystalline domains since it would have disappeared with annealing at high temperatures.

The presence of a second relaxation (above T_g) of PP has been shown by Dynamic Mechanical Thermal Analysis (DMTA) [66-68]. The unusual relaxation signal around 50~80

°C is believed to result from crystal-crystal slip in polypropylene. It is known that DMTA is more sensitive than DSC in recognizing relaxation processes such as glass transition. This might be the reason for the lack of data by DSC analysis on this subject. So far, a similar observation by DSC analysis has only been shown by Hedesiu et al. (Figure 5(a) in Ref. [69]) who did not offer a detailed explanation. A possible explanation for this apparent endothermic discontinuity observed in the DSC analysis originated from the concept of rigid-amorphous fraction (RAF). A more detailed discussion on this feature will be followed in Section 3.5.

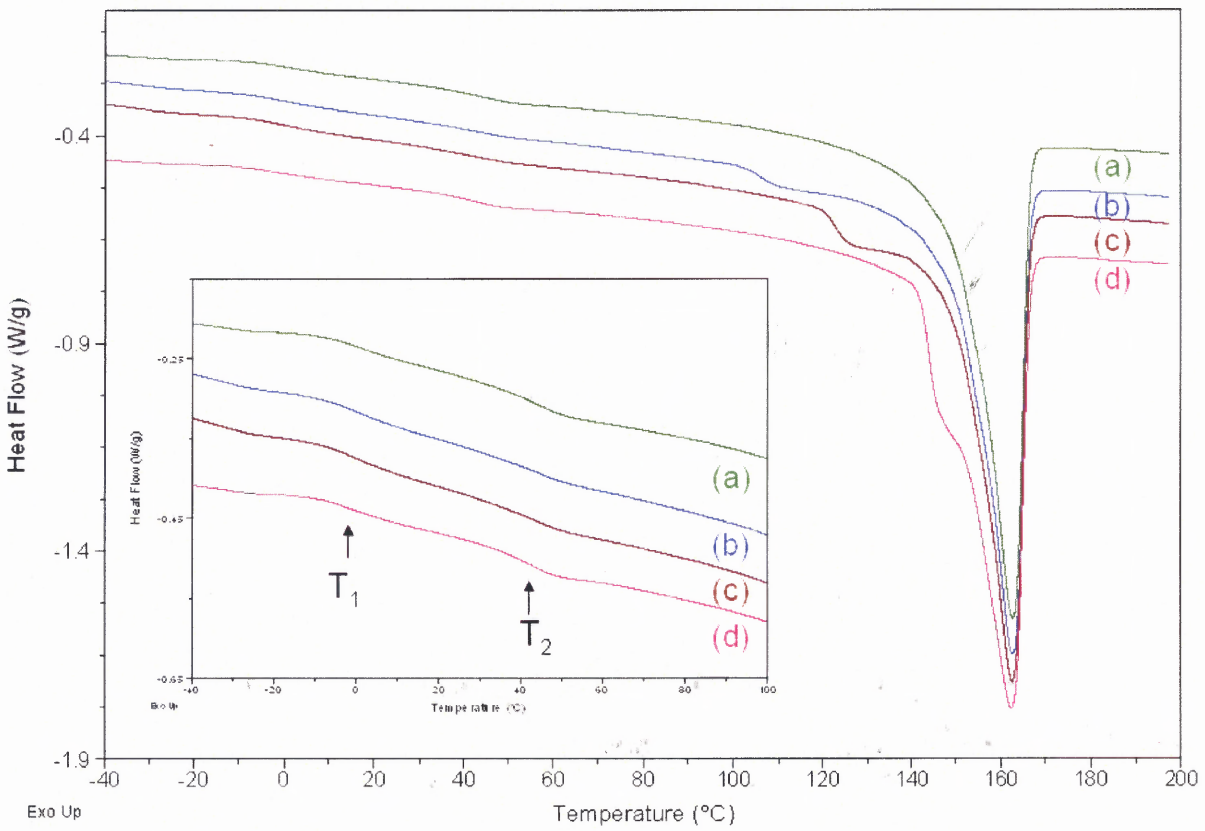

Figure 3.7 DSC heating curves of PP precursor films: (a) F-PP (b) F-PP(An 100C) (c) F-PP(An 120C) (d) F-PP(An 140C).

Table 3.2 Thermal Analysis of PP Precursor Films

Samples	Onset of the discontinuity (°C)	T_m (°C)	Crystallinity (χ_c)
F-PP	NA	161.9	0.43
F-PP(An 100C)	100.6	162.4	0.48
F-PP(An 120C)	119.5	162.2	0.49
F-PP(An 140C)	141.5	161.5	0.51

3.2 Effect of Annealing on PP Stretched Membranes

3.2.1 Morphological Characterization and Mechanical Response

Images of stretched PP membranes are shown in Figure 3.8. All samples could be stretched at 25 °C up to 200% of their original length without breaking. The ductile behavior is due to the low glass transition temperature of PP which is about -5 °C. Typical necking followed by cold drawing is observed in the M-PP, M-PP(An 100C), and M-PP(An 120C) samples ("M" is used to designate stretched membranes). In these samples, the cold drawn region is transparent, and the undrawn region still keeps same features of their precursor films. The width of the cold drawn region is smaller at a higher annealing temperature. By contrast, a distinct opaque membrane is shown in the M-PP(An 140C) sample. The whitened deformed region of M-PP(An 140C) sample covers the entire stretching area, and the width of the center of the deformed region is smaller than in the other samples. Note that the thickness of the M-PP(An 140C) sample was about 30 μm vs. about 15 μm for the other samples. The lower thickness of the stretched membranes with a typical cold drawn feature may be the result of enhanced packing and orientation of the polymer chains.

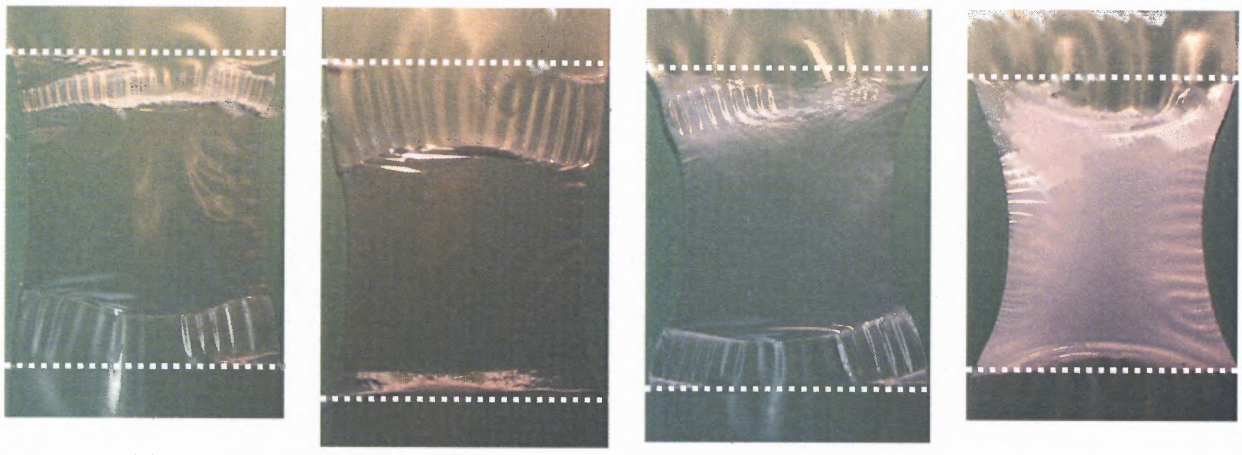

(a) (b) (c) (d)

Figure 3.8 Images of stretched PP membranes: (a) M-PP, (b) M-PP(An 100C), (c) M-PP(An 120C), (d) M-PP(An 140C). (the clamp positions are indicated by white dotted lines.)

Optical microscope images of these samples are shown in Figure 3.9. An elongated morphology is observed in the cold drawn regions of samples M-PP, M-PP(An 100C) and M-PP(An 120C). A much different morphology, however, is shown in sample M-PP(An 140C). The morphological transition of the M-PP(An 140C) sample is consistent with the macroscopic visual observations of Figure 3.8. Samples with typical cold drawn behavior representing the separation and orientation of the lamellar structure are transparent under visible light. On the other hand, the translucent appearance of the M-PP(An 140C) sample in Figure 3.8(d) might be resulting from scattering at the interfaces of microdomains. The domain size of the distinct morphology in the M-PP(An 140C) sample is of about the same scale as for spherulites in the precursor film, Figure 3.2(d). As a result, this distinct morphology might be representing the occurrence of inter-spherulitic deformation.

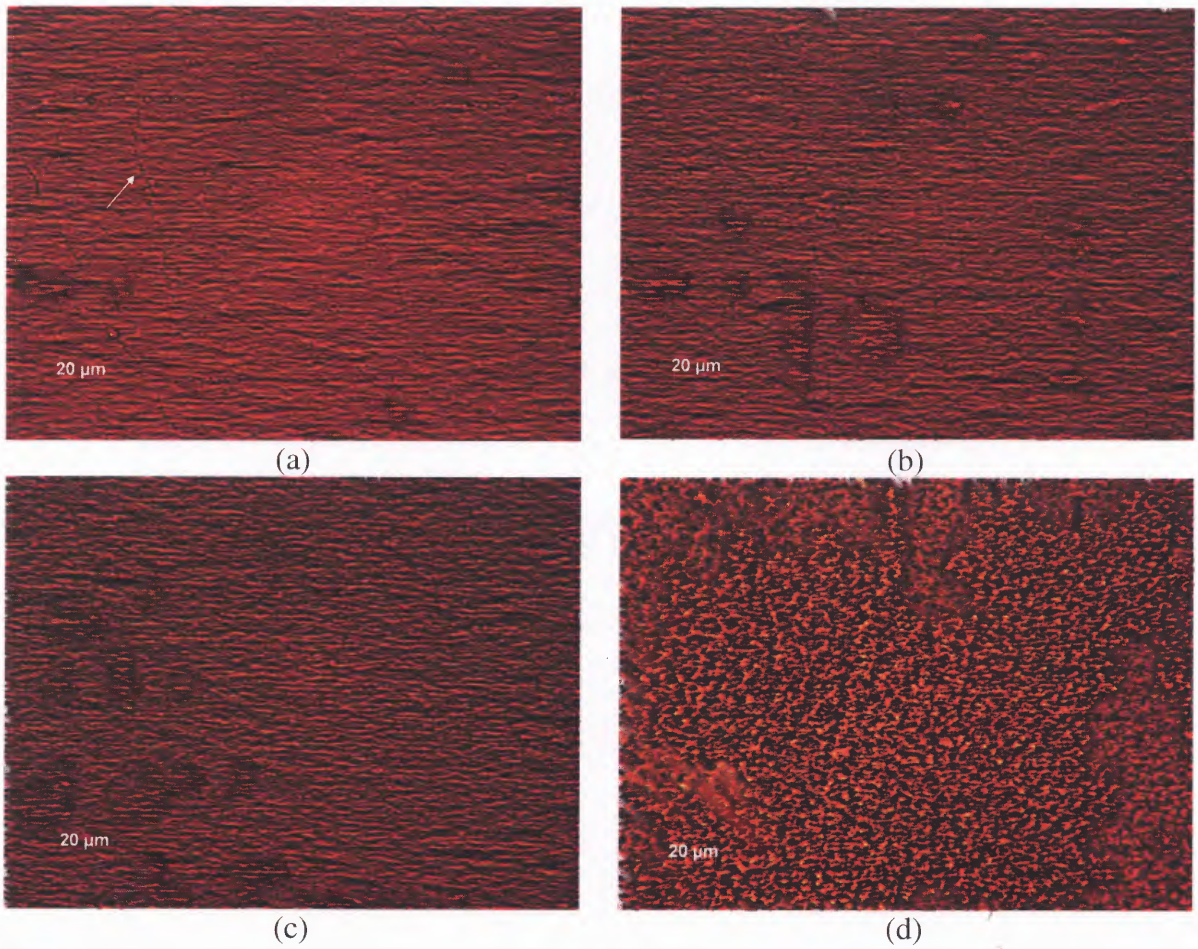

(a) (b)

(c) (d)

Figure 3.9 Optical microscope images of stretched PP membranes (400X): (a) M-PP, (b) M-PP(An 100C), (c) M-PP(An 120C), (d) M-PP(An 140C).

The stress-strain curves of the precursor films during stretching are shown in Figure 3.10. All samples exhibit similar ductile behavior. Furthermore, there is no significant difference in the Young's modulus of all samples. The stress level of the plateau past the yield point increases with annealing temperature. This represents a tougher behavior of the annealed samples due to their enhanced crystalline structure. However, the M-PP(An 140C) sample has a lower yield strain (~11%) than other samples (~15%), (Figure 3.10 insert) which represents a less ductile behavior and increased brittleness. This may be related to the presence of different sites of yielding corresponding to inter- or intra-spherulitic deformations, respectively. For example, the yielding site for the inter-spherulitic

deformation of the annealed samples might be initiated at the spherulitic boundaries due to a more rigid spherulitic structure, and as a result a lower value of yield strain is obtained.

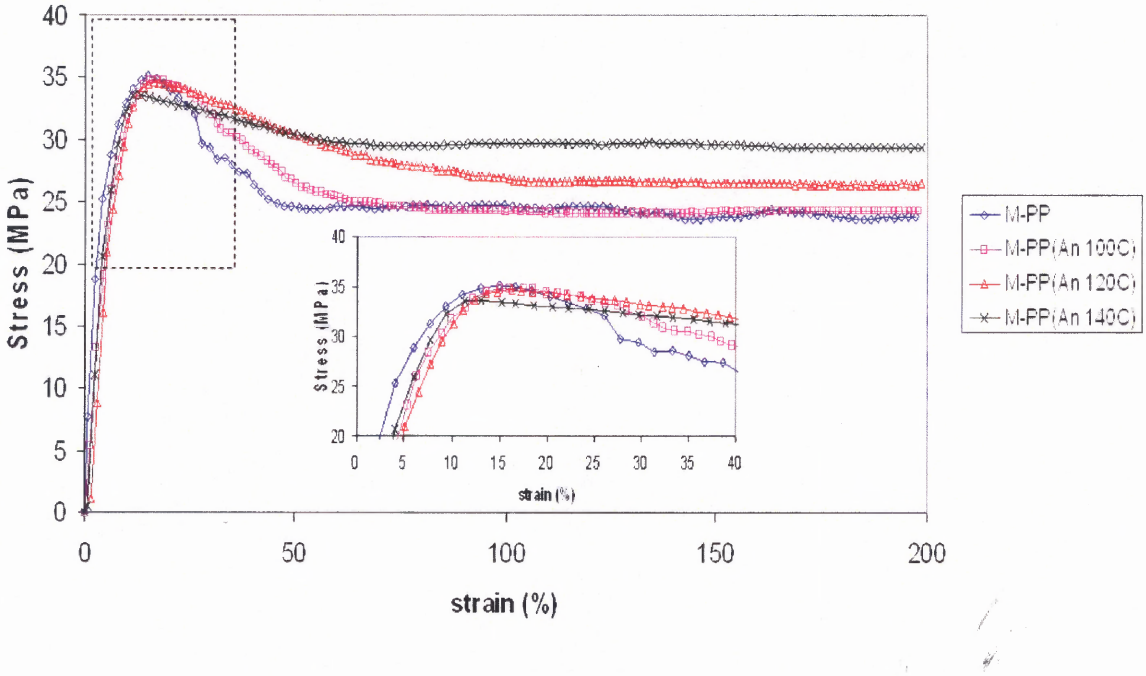

Figure 3.10 Stress-strain curve of stretched PP membranes.

The morphology of the stretched membranes was further examined by SEM. A very thin Au/Pd coating was applied, and the coating conditions were carefully selected in order to reveal the thin lamellar structure. Low magnification SEM images of stretched membranes are shown in Figure 3.11. There is no significant difference between the M-PP, M-PP(An 100C), and M-PP(An 120C) samples. However, a significant morphological difference is observed in the M-PP(An 140C) sample, which shows discrete dark regions surrounded by connected bright regions. The domain sizes of the discrete regions are similar in scale to the spherulite size in the precursor film (Figure 3.2(d)). Further examination of the discrete

regions at higher magnification (Figure 3.12) suggests that the dark discrete regions may contain undeformed lamellae and the bright region may be filled up with lamellar openings. In scanning electron microscopy, a flat surface emits fewer electrons to the detector compared to a rough surface [70]. Therefore, the surface of the undeformed lamellae is smoother and appears to be dark, whereas, the bright region appears to be caused by the uneven lamellar openings. In fact, the cross-hatched lamellar structure of α-PP is observed in all stretched membranes of Figure 3.12. The lamellar openings are almost non-existent in the M-PP and M-PP(An 100C) samples, and smaller in the M-PP(An 120C) sample as compared to the M-PP(An 140C) sample.

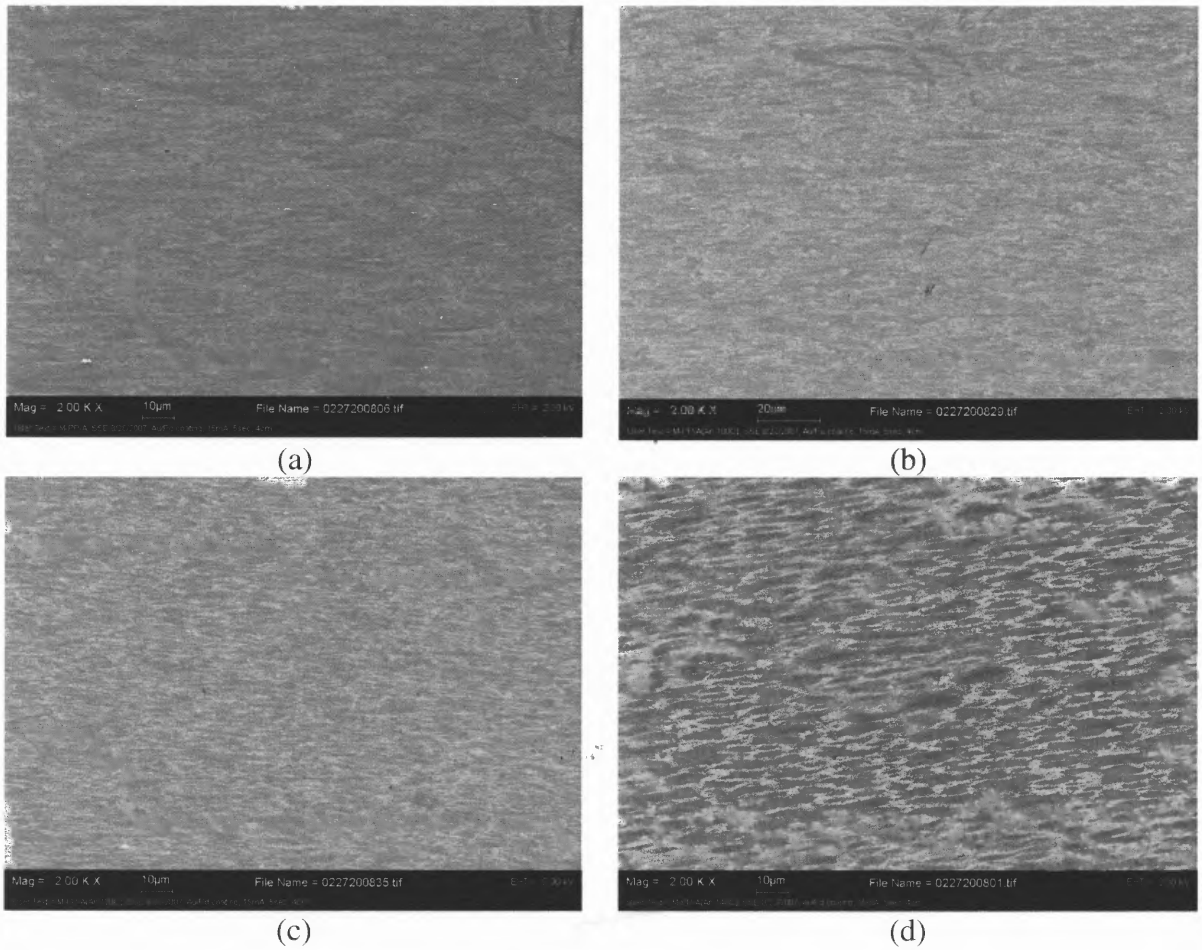

Figure 3.11 SEM images of stretched PP membranes (2000X): (a) M-PP, (b) M-PP(An 100C), (c) M-PP(An 120C), (d) M-PP(An 140C).

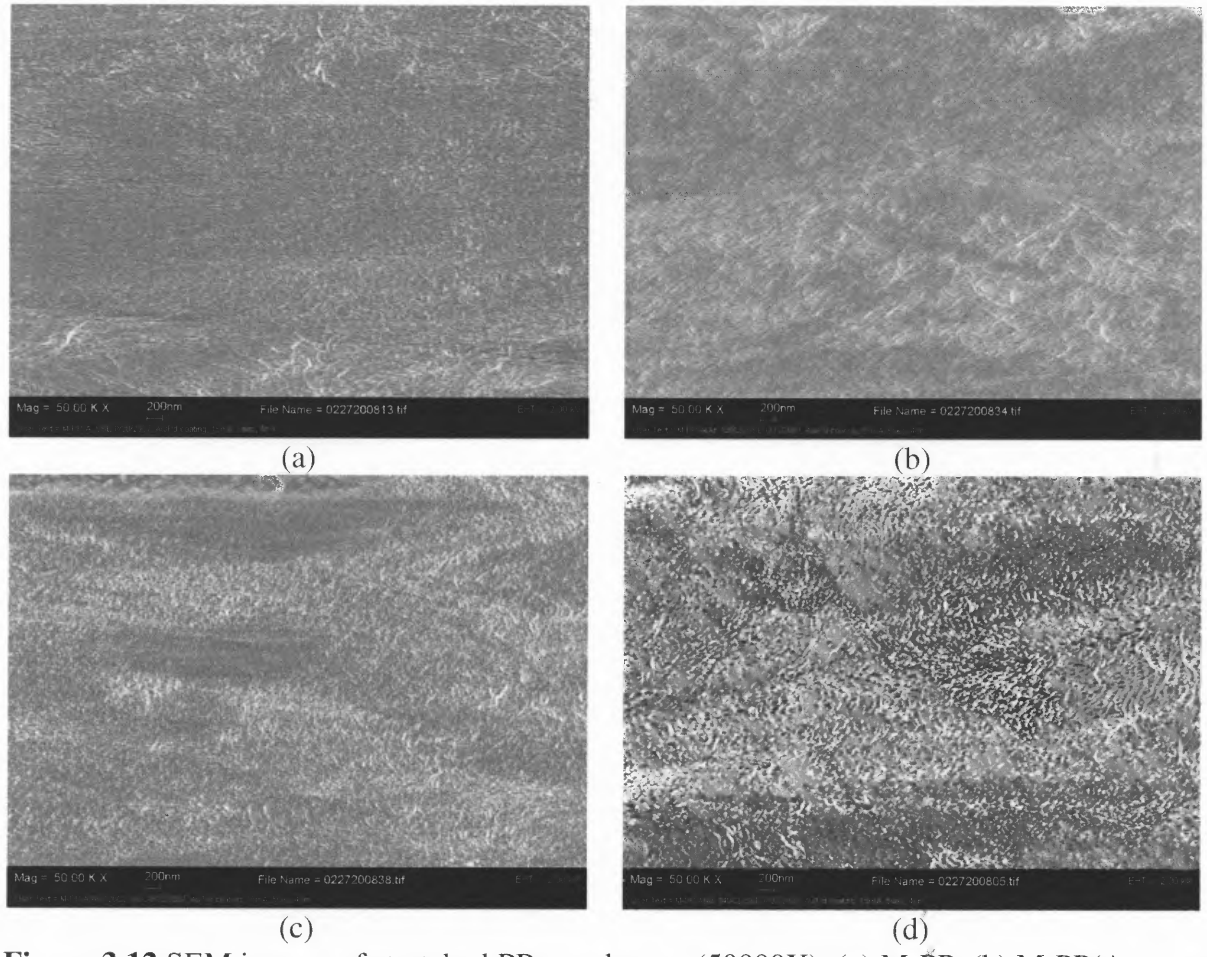

Figure 3.12 SEM images of stretched PP membranes (50000X): (a) M-PP, (b) M-PP(An 100C), (c) M-PP(An 120C), (d) M-PP(An 140C).

A high magnification SEM image highlighting the bright regions is shown in Figure 3.13(a). It appears that the dark regions represent the undeformed spherulites and the bright regions represent the deformed region of the spherulites. Actually, there are two types of bright regions, a radial-like and a ring-like. The radial-like bright region emanates from the center of the dark region, and the ring-like bright region engulfs the dark region. Since the bright regions can be recognized as the lamellar openings, the radial-like pattern would indicate intra-spherulitic deformation and the ring-like pattern suggests inter-spherulitic deformation. The occurrence of each deformation pattern has been reported individually, but the coexistence of them has not been documented. This is important since the anticipated

catastrophic intra-spherulite deformation during cold drawing appears to be halted up by inter-spherulitic deformation. As shown in Figure 3.13(b), the lamellar openings are located between the R-lamellae and the T-lamellae, and the dimensions of these openings are about 50~100nm.

A highlight of debonded morphology around some foreign particles is shown in Figure 3.13(c). The presence of lamellar openings is still evident inside the debonded morphology. A detailed discussion on the effect of debonding will be presented in Section 3.7.

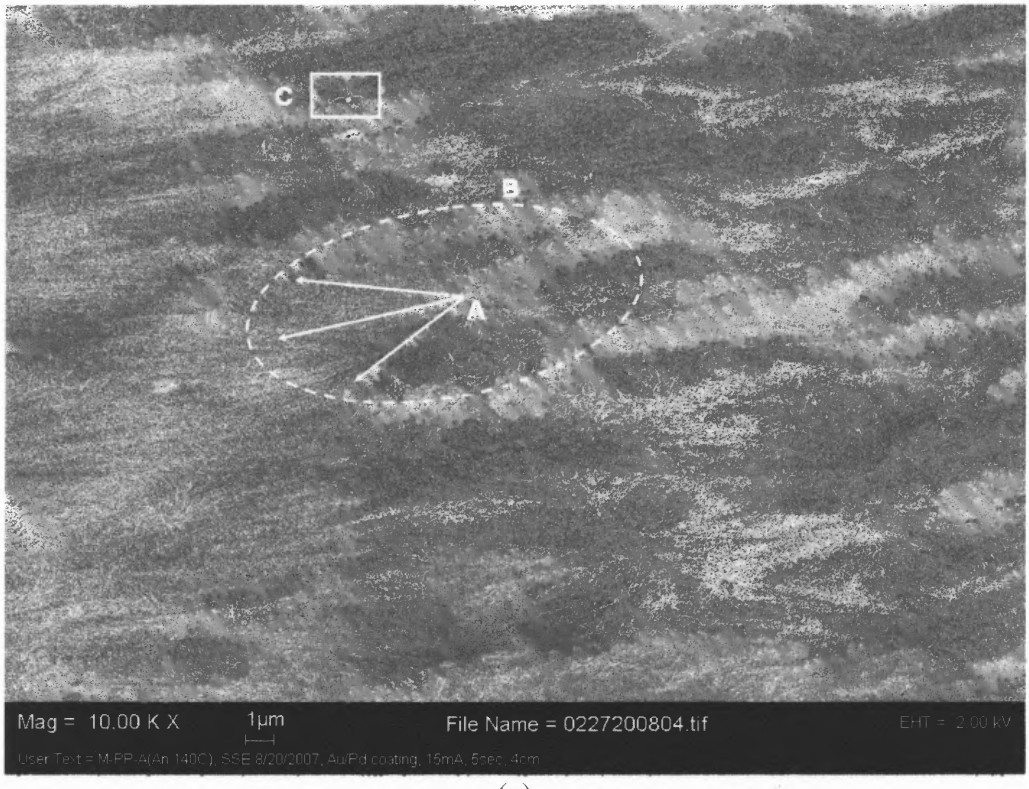

(a)

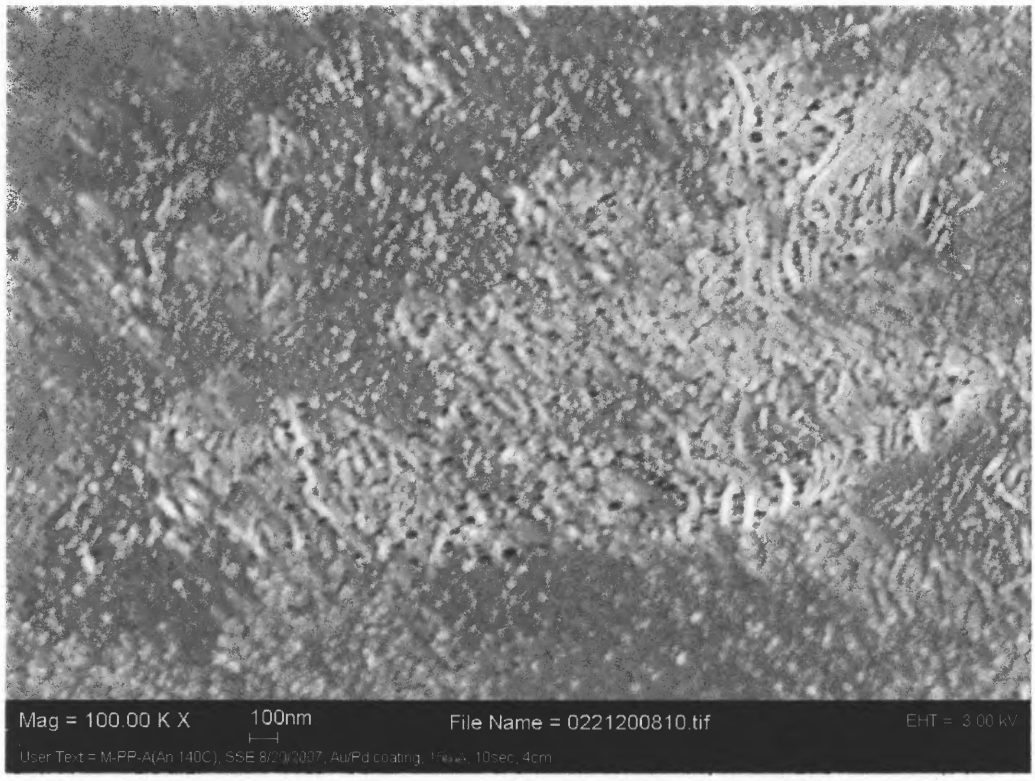

(b)

(c)

Figure. 3.13 SEM images of M-PP(An 140C): (a) spherulitic structure (10000X) (A: radial-like bright region, B: ring-like bright region, C: foreign particle); (b) lamellar opening (100000X), (c) debonding morphology around a foreign particle (100000X).

3.2.2 Crystallographic Characterization

The morphological differences of the M-PP(An 140C) sample were also confirmed by comparing the WAXS spectra of the precursor films and the stretched membranes. The WAXS spectra of PP stretched membranes are shown in Figure 3.14. In comparison to the WAXS spectra of their precursor films (Figure 3.6), a transition was found in the M-PP(An 140C) sample, which is consistent with the observations in the morphological characterization. The WAXS spectra of the stretched membranes exhibit two distinct patterns, a broadened-peak pattern in the M-PP, M-PP(An 100C) and M-PP(An 120C) samples, and a pattern resembling that of the precursor film in the M-PP(An 140C) sample. The reasons for the difference in the WAXS spectra are discussed below:

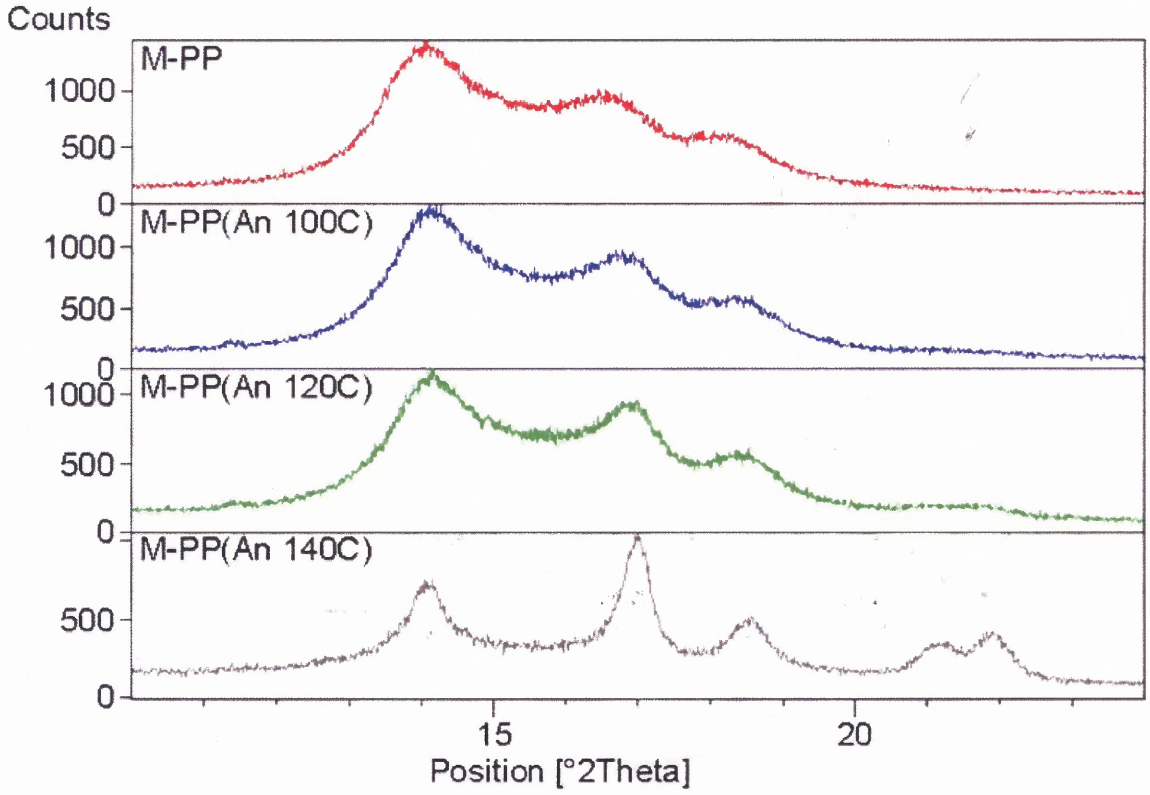

Figure 3.14 WAXS spectra of stretched PP membranes.

The Wide Angle X-ray Scattering apparatus used in this study for one-dimensional examination is also known as a powder diffractometer. A simplified view of this θ-2θ Brag-Brentano setup is shown in Figure 3.15(a). The incident X-ray beam is emitted from the X-ray generator and collected by detector. The sample is stationed and horizontally placed, and the observation is made by spontaneously moving the generator and the detector at an angle θ. In a typical θ-2θ scan, the diffracted incident beam can only be found in the detector when the condition of Bragg's law ($\lambda = 2d\sin\theta$) is satisfied [71]. A sample with a regular d-spacing will only show one sharp signal in the θ-2θ scan. The presence of a peak represents the slightly varied d-space due to the imperfect packing. The tilted surfaces (Figure 3.15(b) and (c)) won't show any signal during the scan since the conditions of Bragg's law can not be matched. As a result, the one-dimensional WAXS examination can only detect a regular d-spacing parallel to the sample surface. In general, in order to detect the entire possible d-spacing in the sample, the sample has to be ground into powder to reach a maximum randomness. This is the reason that this method is also called "powder diffraction".

As mentioned earlier, lamellae grow radially from the center of the spherulite (Figure 1.8(b)), and the spherulite can be regarded as a random sample in powder diffraction. Therefore, the entire crystallographic forms of PP can be detected in the spherulitic samples as shown in Figure 1.17(b). On the other hand, the crystallographic properties of the spherulites become anisotropic when they are deformed and elongated because lamellae are also broken and oriented at the same time. Some of the earlier peaks might not be found due to the resulting anisotropy. In other words, the degree of randomness (or the degree of orientation) of the sample could be described if certain characteristic peaks can be related to the direction of orientation.

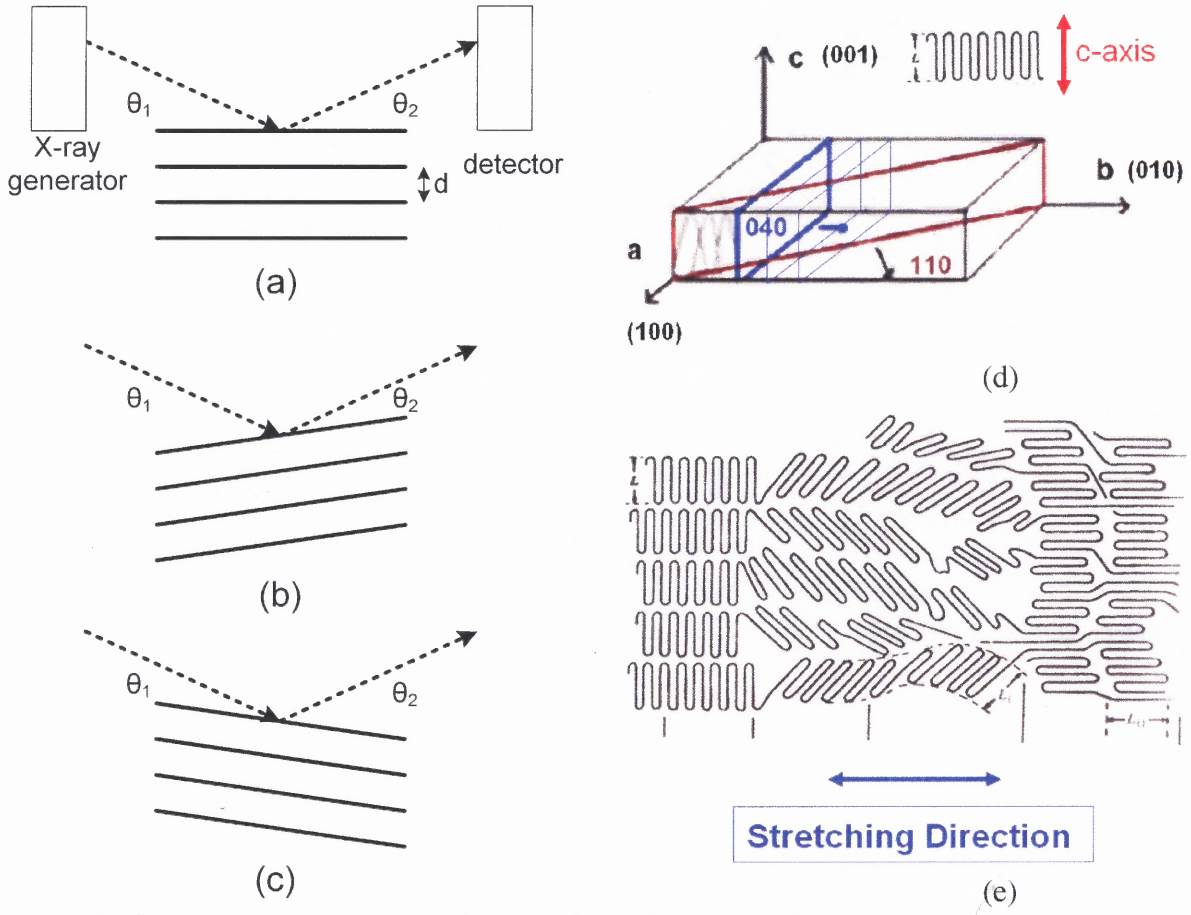

Figure 3.15 Introduction to one dimensional WAXS examination on inter/intra-spherulitic deformation: (a) sample position matched Bragg's law, (b) and(c) sample position does not match Bragg's law, (d) schematic indication of the plane group I (parallel to lamellae packing direction) [15], (e) aligned broken lamellae along stretching direction [21].

The main crystallographic planes of the α-form (Figure 3.5(a)) can be further categorized into two plane groups. The plane group I includes α_1 (110), α_2 (040) and α_3 (130) peaks which are normal to the (001) plane (c-axis) as shown in Figure 3.15(d). The plane group II is the lumped α_4 ((111), (041) and (131)) peak which are inclined to the surface of lamellae [72]. Both plane groups can be detected within the non-oriented spherulitic samples as shown in Figure 3.6.

For all stretched membranes, broader peaks were observed due to the broken lamellae. Furthermore, the plane group II is almost undetectable in the M-PP, M-PP(An

100C) and M-PP(An 120C) samples, but is still apparent in the M-PP(An 140C) sample. Ideally, in a fully oriented sample (c-axis aligned along stretching direction), only the plane group I can be detected since powder diffraction only detects the crystallographic planes parallel to sample surface. In the samples containing deformed spherulites, the broken lamellae are oriented by cold drawing after the occurrence of intra-spherulitic deformation. The appearance of the plane group I is expected since the broken lamellae are oriented along the stretching direction as shown in Figure 3.15(e). At the same time, the absence of the plane group II should become more evident at a highly oriented sample. This is shown in the M-PP, M-PP(An 100C), and M-PP(An 120C) samples.

The presence of the plane group II in the M-PP(An 140C) sample represents a less oriented lamellar structure and a less deformed spherulitic structure. Since all the samples were stretched far beyond their yielding point without breaking, a less deformed spherulitic structure implies the occurrence of inter-spherulitic deformation in the M-PP(An 140C) sample. As a result, the one-dimensional WAXS provide a rapid examination method to distinguish inter-spherulitic and intra-spherulitic deformation.

On the other hand, the presence of T-lamellae should have no influence on the WAXS examination. There are two reasons for that. Firstly, the difference between R-lamellae and T-lamellae is on the lamellar growing direction not on their crystallographic features (Figure 1.18(b)). Secondly, the disappearance of plane group II is due to the alignment of broken lamellae towards the stretching direction, and the occurrence of orientation (initiated by intra-spherulitic deformation and prevented by inter-spherulitic deformation) is rather dependent on the thickness of the lamellae instead of their types. Furthermore, the WAXS examination provides an evidence of inter-spherulitic deformation

within a lamellar scale since the unit cell resides in the lamellae. WAXS examination could be an important characterization tool since morphological observation would be limited as spherulites are becoming smaller as in the case of nucleated polypropylene.

The concept of using the crystallographic differences from WAXS spectra to confirm the occurrence of inter-spherulitic deformation can be further illustrated with the Celgard® 2400 polypropylene membrane. In the Celgard® process, the row lamellae are highly oriented along the stretching direction as shown in Figure 1.8 and Figure 1.10. A comparison of WAXS spectra of sample with spherulitic structure (F-PP, F-PP(An 140C), and M-PP(An 140C)) and oriented structure (M-PP and Celgard® 2400 PP membrane) is shown in Figure 3.16. The well resolved peaks of plane group I in the Celgard® 2400 PP membrane (Figure 3.16) imply a better chain packing morphology within the row lamellar structure.

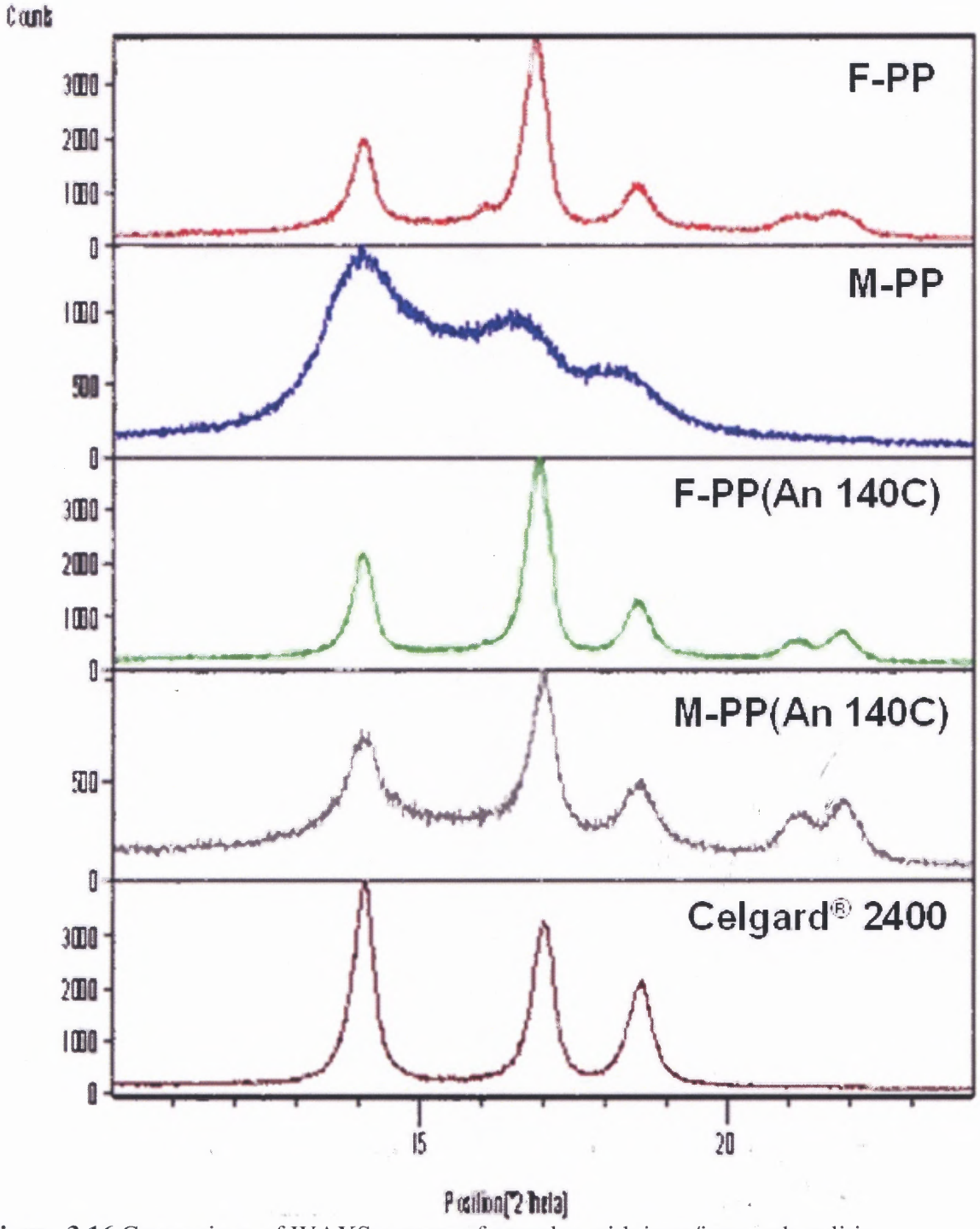

Figure 3.16 Comparison of WAXS spectra of samples with inter/intra-spherulitic deformation. (Celgard® 2400 represents a fully oriented PP films)

3.2.3 Porous Structure Characterization

Based on the morphological and crystallographic analysis of the stretched PP membranes, the concept of initiating inter-spherulitic deformation by enhancing inherent spherulitic integrity has been demonstrated. Furthermore, by taking advantage of the cross-hatched lamellar structure of α-PP, a novel porous structure with pore size around 50 ~ 100 nm appears to have been created by the combination of intra-spherulitic and inter-spherulitic deformation.

Preliminary characterization results of the porous structure are shown in Table 3.3. The pore interconnectivity of stretched membranes was tested by methanol permeation. The bubble point pressure for the test was not high due to the low surface tension of methanol vis-à-vis the critical surface tension of polypropylene. The precursor films were tested first and no permeation was detected up to 24 hours. For the stretched membranes, the methanol flux decreased with increasing annealing temperature, and became practically zero in the M-PP(An 120C) sample. The methanol flux was regained in the M-PP(An 140C) sample. From the previous discussion, the M-PP, M-PP(An 100C), and M-PP(An 120C) samples underwent intra-spherulitic deformation and showed morphological similarity such as a transparent appearance (Figure 3.8) and an elongated morphology (Figure 3.9). As mentioned, the interconnectivity of intra-spherulitic deformation is poor due to its arbitrary location in spherulites, and should show less permeability in the absence of large defects. The reason for the high methanol flux in the non-annealed M-PP sample might be due to the presence of cracks developed during stretching, which are indicated by an arrow in Figure 3.9(a). The declining methanol flux with increasing annealing temperature is the result of fewer defects in the samples with improved crystalline structure. On the other hand, the M-PP(An 140C) sample underwent mostly inter-spherulitic deformation. There were no cracks

shown under the optical microscope (Figure 3.9(d)). The interconnectivity of lamellar openings could increase significantly by the combination of intra- and inter-spherulitic deformations. Thus, the regained methanol flux in the M-PP(An 140C) sample appears to be the result of lamellar openings linked up by inter-spherulitic deformation.

Table 3.3 Thermal Analysis and Methanol Permeation of PP Precursor Films and Stretched Membranes

Properties	T_m (°C)	Crystallinity (χ_c)	*Methanol permeation (l/m^2hr)[a]
Precursor films (F)			
F-PP	161.9	0.43	No permeation
F-PP(An 100C)	162.4	0.48	No permeation
F-PP(An 120C)	162.2	0.49	No permeation
F-PP(An 140C)	161.5	0.51	No permeation
Stretched membranes (M)			
M-PP	162.0	0.42	9.4 ± 3.6
M-PP(An 100C)	162.6	0.46	4 ± 2.3
M-PP(An 120C)	162.9	0.48	<0.1
M-PP(An 140C)	163.1	0.49	4.5 ± 1

* The methanol permeation results were based on the average of four measurements.

The porosity of the stretched membranes (Table 3.4) can be estimated through crystallinity results from DSC heating scans. The crystallinity differences between precursor films and their stretched membranes were not significant, which indicates that most of the crystalline structure is preserved after stretching. The measured sample mass (M_M) is always lower than the estimated mass (M_{cal}). The difference between M_M and M_{cal} indicates the presence of voids in the stretched membranes. The porosity of the M-PP, M-PP(An 100C), and M-PP(An 120C) samples is about 0.02~0.06. The low porosity in these cold drawn samples is the result of polymer chains packing and orientation which is also shown from the

morphological and crystallographic analysis. Polymer chain packing and orientation, however, is interrupted by inter-spherulitic deformation. Those less deformed spherulites (Figure 3.13(a)) might prevent the lamellar openings from collapsing, and maintain interconnectivity of the porous structure, as shown in the M-PP(An 140C) sample with a porosity about 0.18.

Table 3.4 Porosity Estimation of Stretched PP Membranes

Properties	*χ_c	ρ_{cal} (g/cm^3)	**t (μm)	V_M (mm^3)	M_M (mg)	V_{cal} (mm^3)	Porosity (ε)
M-PP	0.42	0.893	15	26.7	22.6	25.3	0.06
M-PP(An 100C)	0.46	0.897	15	26.7	23.5	26.2	0.02
M-PP(An 120C)	0.48	0.899	16	28.5	24.9	27.7	0.03
M-PP(An 140C)	0.49	0.900	31	55.2	42.1	46.8	0.18

* Crystallinity measurement to calculate porosity was based on one sample having methanol permeation value close to the averaged value shown in Table 3.3.
** "t" is the thickness of stretched membrane.

3.2.4 α-form Orientation Index for PP Stretched Membranes

As shown in previous sections, the intra/inter-spherulitic deformation can be detected morphologically (on a spherulite scale) and crystallographically (on a lamellar scale). With intra-spherulitic deformation, spherulites are deformed and elongated; therefore, lamellae are also oriented along the stretching direction. A highly oriented lamellar structure is expected in the cold-drawn region. On the contrary, spherulites are much less deformed with inter-spherulitic deformation and lamellae are capable of maintaining their isotropy within the spherulites. Based on the discussion in section 3.2.2, the presence of plane group II (the lump α_4) in the stretched membranes can provide a qualitative evidence for the occurrence of inter-spherulitic deformation. The quantitative description of this observation is as follows.

A quantitative characterization of the lamellar orientation using WAXS spectra was suggested by Trotignon et al. [50]. The α-form orientation index (A) is defined as follows:

$$A = \frac{h\alpha_1}{h\alpha_1 + h\alpha_4} \tag{3.1}$$

where $h\alpha_1$ and $h\alpha_1$ are the heights of the corresponding crystalline peaks taken from the amorphous background. A = 1 in a fully oriented sample because there is no α_4 peak in the WAXS spectrum. According to their results [73], A = 0.57 for an isotropic sample.

A comparison of the A values of the precursor films and the corresponding stretched membranes is shown in Table 3.5 for a given set of stretching conditions (R_S = 12.7 cm/min, E_S = 200%, and T_S = 25 °C). The A value for the non–annealed F-PP sample is 0.82, and slightly decreased with increasing annealing temperature (A = 0.81 of the F-PP(An 100C) sample and A = 0.80 for the F-PP(An 140C) sample). The somewhat high orientation index of the precursor films indicates pre-orientation of the chains induced by the extrusion process, and rearrangement of these chains at the high annealing temperature. The A value of the non-annealed stretched membrane (M-PP) was 0.98 which indicates a nearly fully oriented sample and is consistent with the morphological observations. Annealing temperatures of 100 °C and 120 °C did not promote inter-spherulitic deformation at the investigated stretching conditions since A = 0.99 for the annealed stretched membrane M-PP(An 100C) and A = 0.92 for the M-PP(An 120C) sample. However, a higher annealing temperature of 140 °C did trigger inter-spherulitic deformation which is shown in the M-PP(An 140C) sample with an A value of 0.62 representing a high degree of an isotropy of the lamellar structure even of the film was stretched up to 200% of its original length. This value

is lower than that of its precursor film F-PP(An 140C), and may have resulted from pre-oriented lamellae within the spherulites that were able to rebound and restore to a more isotropic status due to the loosened spherulitic boundary during inter-spherulitic deformation.

The results of crystallinity and porosity of the stretched membranes are also summarized in Table 3.5 Annealing at 140 °C results in the highest crystallinity for both unstretched and stretched samples. The porosity of the stretched samples, M-PP, M-PP(An 100C), and M-PP(An 120C) samples is low, about 0.02~0.06. However, a higher porosity (0.18) is observed in the M-PP(An 140C) sample. The low porosity of the samples with a high α-form orientation index represents the result of chain orientation and packing in these stretched membranes. On the other hand, the higher porosity of the sample with a low α-form orientation index indicates that the porous structure (lamellar openings) was preserved by the less-deformed spherulites.

Table 3.5 The α-form Orientation Index (A) and Porosity of PP Precursor Films and Stretched Membranes.

Samples	Stretching conditions			A	Crystallinity (χ_c)	Porosity (ε)
	E_S (%)	R_S (cm/min)	T_S (°C)			
F-PP				0.82	0.43	-
F-PP(An 100C)				0.81	0.48	-
F-PP(An 120C)				0.80	0.49	-
F-PP(An 140C)				0.80	0.51	-
M-PP	200	12.7	25	0.98	0.42	0.06
M-PP(An 100C)	200	12.7	25	0.99	0.46	0.02
M-PP(An 120C)	200	12.7	25	0.92	0.48	0.03
M-PP(An 140C)	200	12.7	25	0.62	0.49	0.18

3.3 Effect of Extension Ratio on PP Stretched Membranes

The effect of extension ratio on the intra-spherulitic and inter-spherulitic deformations was investigated by stretching the precursor films F-PP and F-PP(An 140C) at extension ratios ranging from 100% to 600% at R_S = 12.7 cm/min and T_S = 25 °C. Results are shown in Table 3.6. Some noteworthy images of the stretched membranes are shown in Figure 3.17. A typical cold-drawn behavior was observed in the non-annealed stretched membranes showing transparent cold-drawn and non-cold-drawn regions. The proportion of the cold-drawn region increases and that of the non-deformed region decreases with increasing extension ratio as shown in Figures 3.17(a) and (b). For the annealed stretched membranes, an opaque appearance within the stretched region is observed (Figures 3.17(c) and (d)). The width in the middle of these samples decreased with increasing extension ratio.

Table 3.6 The α-form Orientation Index (A), Crystallinity and Porosity of PP Membranes Stretched at Different Stretching Ratios.

Samples	Stretching conditions			A	Crystallinity (χ_c)	Porosity (ε)
	E_S (%)	R_S (cm/min)	T_S (°C)			
M-PP	100	12.7	25	0.98	0.42	0.04
M-PP	200	12.7	25	0.98	0.42	0.06
M-PP	300	12.7	25	0.98	0.41	0.02
M-PP	400	12.7	25	0.99	0.41	0.03
M-PP	500	12.7	25	1.00	0.42	0.02
M-PP	600	12.7	25	1.00	0.41	0.02
M-PP(An 140C)	100	12.7	25	0.58	0.50	0.22
M-PP(An 140C)	200	12.7	25	0.62	0.49	0.18
M-PP(An 140C)	300	12.7	25	0.74	0.49	0.11
M-PP(An 140C)	400	12.7	25	0.76	0.48	0.09
M-PP(An 140C)	500	12.7	25	0.87	0.47	0.08
M-PP(An 140C)	600	12.7	25	0.91	0.47	0.06

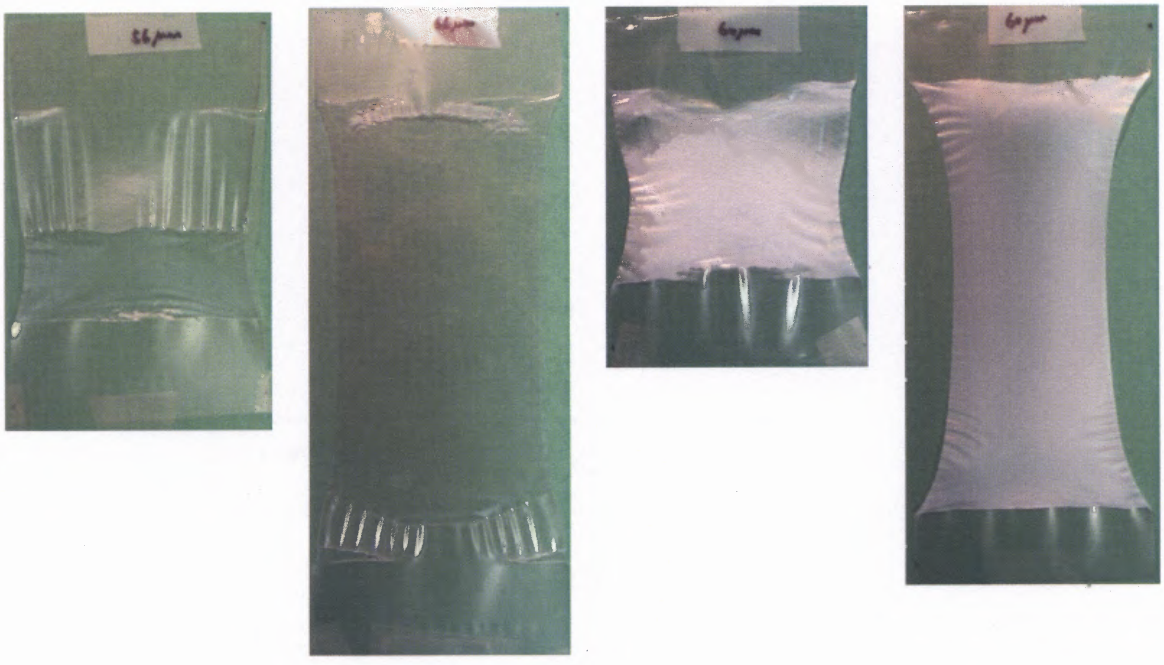

(a) (b) (c) (d)

Figure 3.17 Images of membranes stretched at different E_S: (a) M-PP (E_S 100%), (b) M-PP (E_S 400%), (c) M-PP(An 140C) (E_S 100%), (d) M-PP(An 140C) (E_S 400%). Stretching conditions were R_S 12.7 cm/min and T_S 25 °C.

Figure 3.18 plots the α-form orientation index versus extension ratio. The A values of the non-annealed samples were about 1. As mentioned in previous sections, the cold-drawing behavior represents lamellae breaking and alignment along the stretching direction. The higher extension ratio simply created more cold-drawn regions, and the lamellae in these regions remained highly oriented. By contrast, the A values of the annealed samples increased with increasing extension ratio. The A value of the annealed stretched sample at 100% extension ratio was only 0.58; this low value suggests the recovery of pre-oriented spherulites in the earlier stage of inter-spherulitic deformation. Note that the annealed sample could be stretched up to 600% of its original length without fracture. This indicates that the residual lamellae at the separated spherulitic boundary were strong enough to prevent sample rupture. The spherulites of inter-spherulitic deformation started to orient with increasing

extension ratio which implied the occurrence of intra-spherulitic deformation at the late stage of stretching. As a result, the A value of the annealed stretched sample at 600% extension ratio was 0.91 which was close to that of the fully oriented sample.

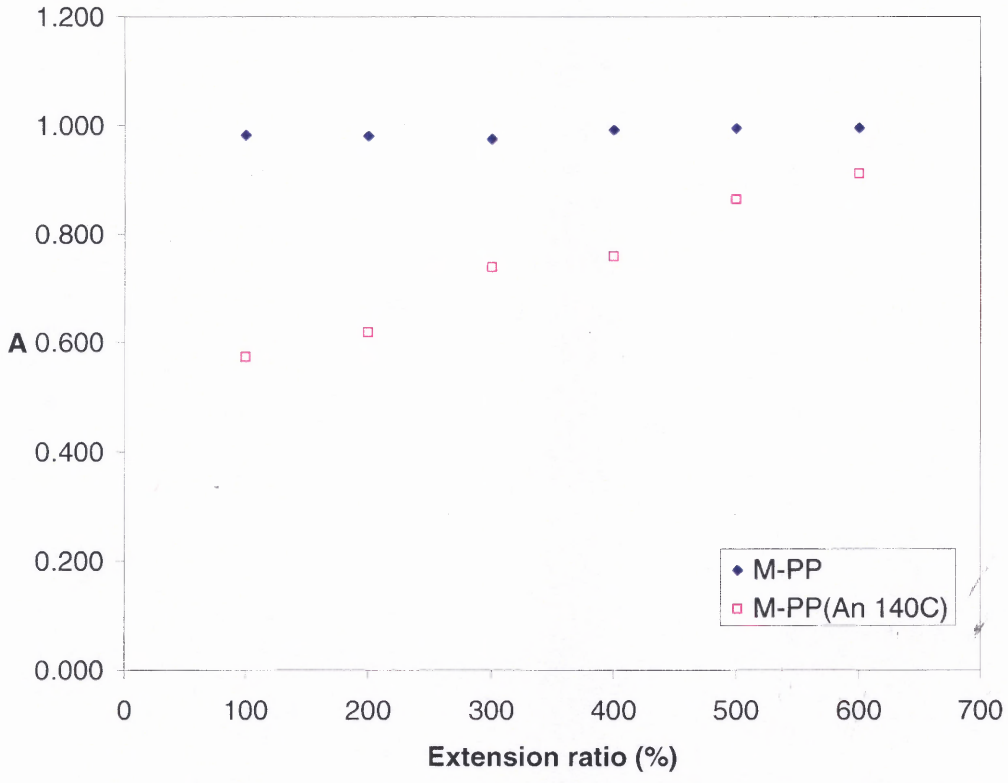

Figure 3.18 α-form orientation index (A) of membranes stretched at different E_S. Stretching conditions were R_S 12.7 cm/min and T_S 25 °C.

The porosity of samples produced at different extension ratios is shown in Figure 3.19. The porosity of non-annealed samples was about 0.02~0.06, and did not show a significant change with extension ratio. Since increasing the extension ratio of the non-annealed samples only enlarged the cold-drawn region which was already fully oriented, a similar porosity is expected. The porosity of the annealed samples decreased with increasing extension ratio, which is consistent with the opposite trend for the α-form orientation index

(Figure 3.18). Thus, the highest porosity attained so far was about 0.18 at an extension ratio of 100%. However, a low extension ratio is not necessarily a good strategy to improve porosity, since the unevenly deformed region at a low extension ratio (Figure 3.17(c)) could limit the membrane area available for permeation.

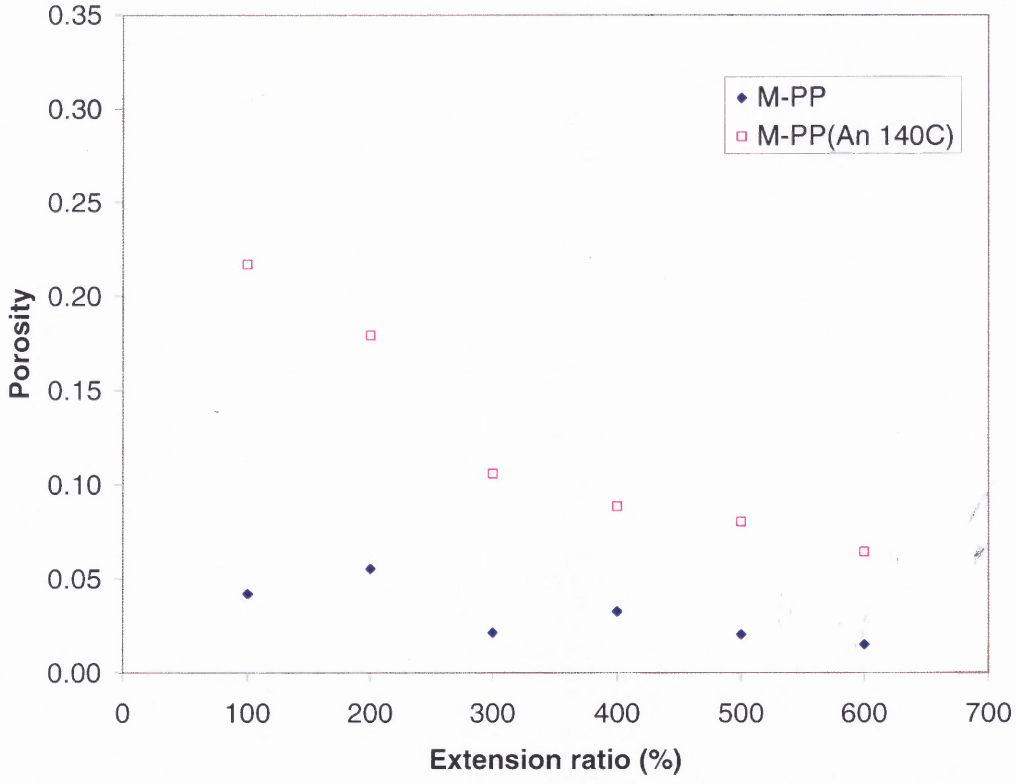

Figure 3.19 Porosity of membranes stretched at different E_S. Stretching conditions were R_S 12.7 cm/min and T_S 25 °C.

3.4 Effect of Stretching Rate on PP Stretched Membranes

The effect of stretching rate on intra- and inter-spherulitic deformations was investigated by stretching the precursor films F-PP and F-PP(An 140C) at a stretching rate ranging from 0.25 cm/min to 50.8 cm/min with E_S = 200% and T_S = 25 °C. Results are shown in Table 3.7. The effect of stretching rate on the α-form orientation index is shown in Figure 3.20.

The non-annealed samples showed high A values within the investigated range. For the annealed samples, intra-spherulitic deformation was only evident at the highest stretching rate (R_S = 50.8 cm/min). An apparent inter-spherulitic deformation with low A values was found at other stretching rates.

Table 3.7 The α-form Orientation Index (A) and Porosity of PP Membranes Stretched at Different Stretching Rates (Stretching Temperature 25 °C).

Samples	Stretching conditions			A	Crystallinity (χ_c)	Porosity (ε)
	E_S (%)	R_S (cm/min)	T_S (°C)			
M-PP	200	50.8	25	0.99	0.41	0.02
M-PP	200	25.4	25	0.99	0.42	0.03
M-PP	200	12.7	25	0.98	0.42	0.06
M-PP	200	2.54	25	0.99	N/M*	N/M
M-PP	200	1.27	25	0.98	N/M	N/M
M-PP	200	0.25	25	0.98	N/M	N/M
M-PP(An 140C)	200	50.8	25	0.98	0.47	0.03
M-PP(An 140C)	200	25.4	25	0.69	0.48	0.04
M-PP(An 140C)	200	12.7	25	0.62	0.49	0.18
M-PP(An 140C)	200	2.54	25	0.63	N/M	N/M
M-PP(An 140C)	200	1.27	25	0.67	N/M	N/M
M-PP(An 140C)	200	0.25	25	0.72	N/M	N/M

*N/M is not measured due to uneven surface of the sample at very slow stretching rate.

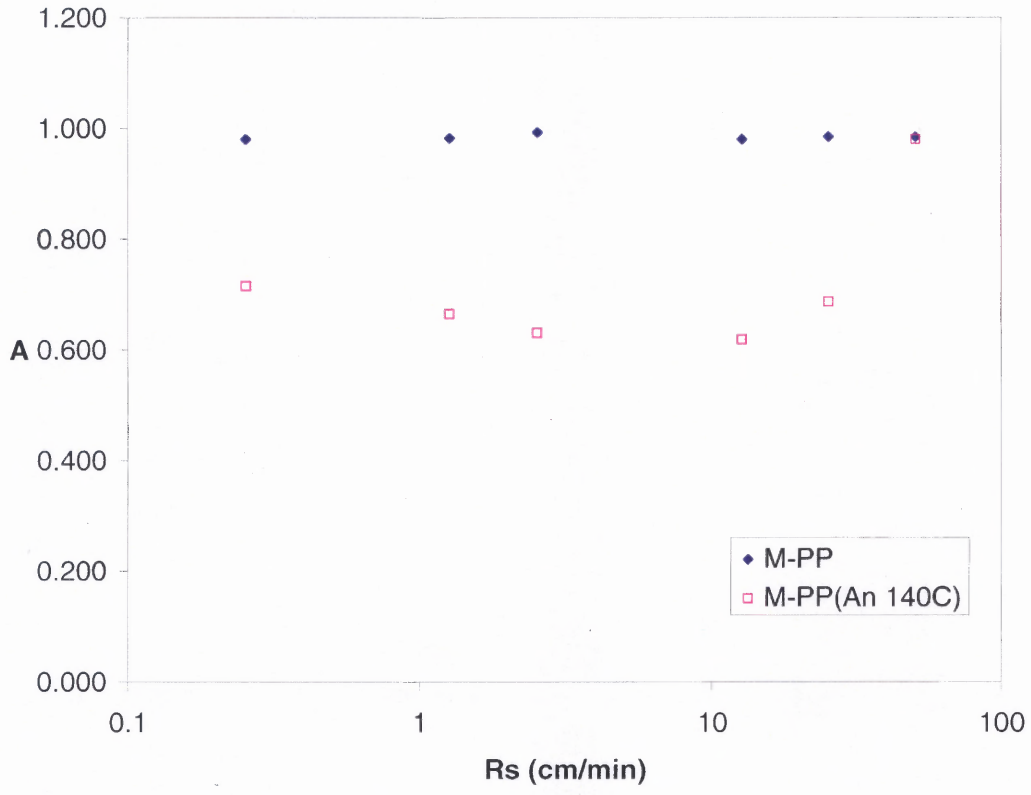

Figure 3.20 α-form orientation index (A) of membranes stretched at different R_S. Stretching conditions were E_S 200% and T_S 25 °C.

In general, polymers show ductile behavior at low stretching rates and brittle behavior at high stretching rates. In this study, even though all samples showed a ductile behavior with no sign of fracture, differences in (apparently) similar ductile behaviors can be distinguished from their microstructures. The ductile behavior of the non-annealed samples is the result of lamellae breaking and orientation inside the spherulites. However, the ductile behavior shown in the samples with inter-spherulitic deformation may be due to the presence of tough residual lamellae at the separated spherulitic boundary. Inter-spherulitic deformation should be more pronounced at a low stretching rate, since the generated stress could be transmitted to a weak site, such as a spherulite boundary. On the other hand, intra-spherulitic deformation would be more favored to occur at a high stretching rate.

The porosity of the samples produced at different stretching rates (Table 3.7) confirms the results from the WAXS analysis. The porosity of the annealed samples increased with decreasing stretching rate. A low porosity (0.03) of the annealed sample at the highest stretching rate (R_S = 50.8 cm/min) is attributed to the intra-spherulitic deformation. Since the surface of the stretched membranes became uneven at stretching rates lower than 2.54 cm/min, porosity at low stretching rates could not be measured. Thus, there is an apparent limitation in using low stretching rates to promote inter-spherulitic deformation. The localized effects on specific weak sites, such as the boundaries around larger spherulites that also endure higher stress, become predominant at much lower stretching rates resulting in an unevenly deformed structure.

3.5 Effect of Stretching Temperature on PP Stretched Membranes

A low stretching temperature of -20 °C was chosen to observe the mechanical response of the precursor films below the T_g of PP (about -5 °C). Brittle fracture images of samples stretched at 12.5 cm/min are shown in Figures 3.21(a) and (b). Based on the results shown in Figures 3.8(a) and (d), a cold-drawn appearance was also expected at stretching temperatures higher than 25 °C (At an increasing temperature above T_g, the amorphous phase is more flexible, and the broken crystalline phase can be oriented more easily). The image of the non-annealed sample stretched at 70 °C is shown in Figure 3.21(c). Interestingly, even though it was still transparent, it did not have the same appearance as the typical cold-drawn pattern shown in Figure 3.8(a). In fact, it had a narrower width in the middle of the deformed region which resembled the appearance of the annealed sample shown in Figure 3.8(d). On the other hand, since the inter-spherulitic region contains a high proportion of amorphous phase due to the

irregularly impinged lamellae, a high stretching temperature should make them more vulnerable to deformation, and as a result, promote inter-spherulitic deformation. The opaque appearance of the annealed sample stretched at 25 °C (Figure 3.8(d)) was expected to be enhanced at a higher stretching temperature. However, a less opaque appearance is observed in Figure 3.21(d). Surprisingly, at the high stretching temperature, the non-annealed (Figure 3.22(a)) and annealed samples (Figure 3.22(b)) showed similar WAXS spectra with well divided peaks and a small amount of α_4 peak. These inconsistent results of the effect of temperature were further investigated by thermal analysis of the precursor films.

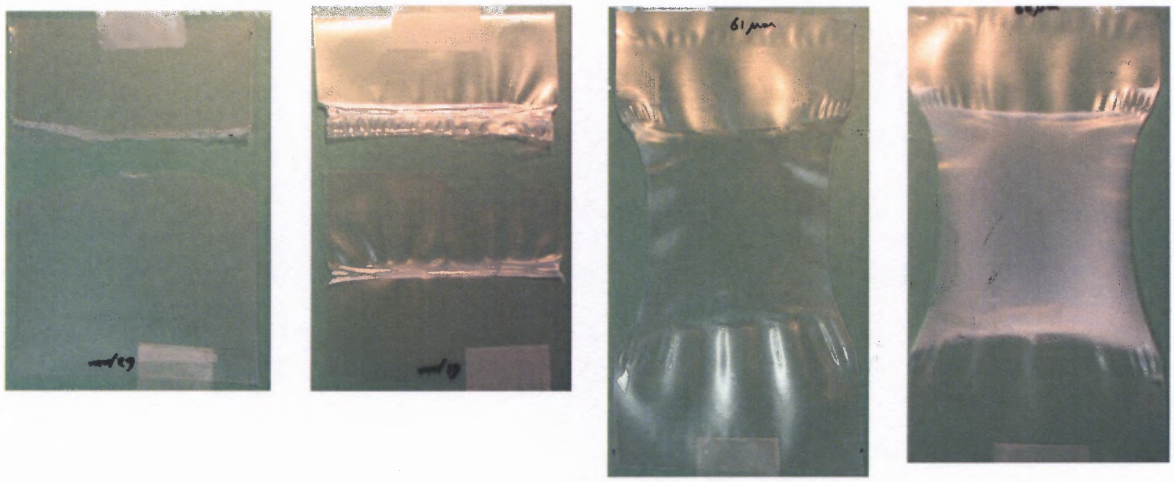

(a) (b) (c) (d)

Figure 3.21 Images of membranes stretched at different T_S: (a), (b) Images of M-PP and M-PP(An 140C) at T_S -20 °C respectively; (c), (d) Images of M-PP and M-PP(An 140C) at T_S 70 °C respectively. Stretching conditions were E_S 200% and R_S 12.7 cm/min.

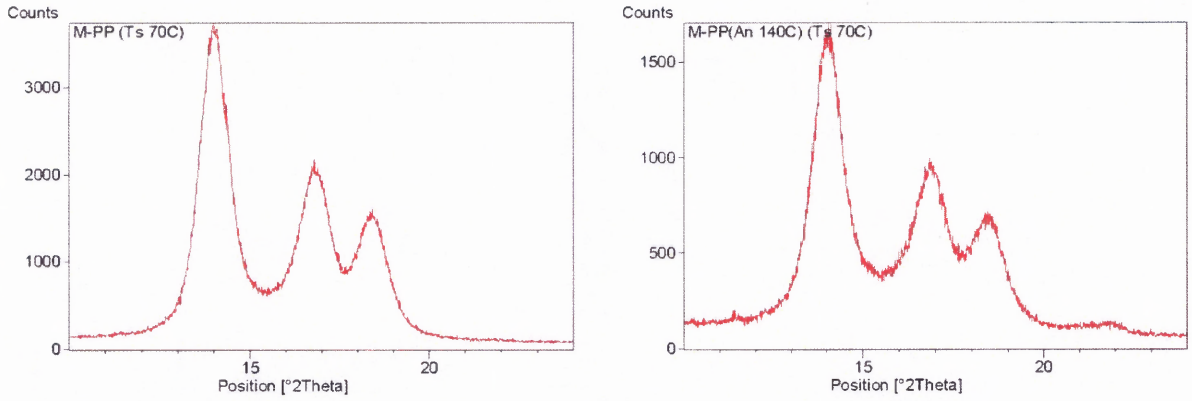

Figure 3.22 Crystallographic examinations of inter/intra spherulitic deformation: (a) M-PP, (b) M-PP(An 140C). Stretching conditions were E_S 200%, R_S 12.7 cm/min, and T_S 70 °C.

The results of DSC heating scans of the F-PP and F-PP(An 140C) samples are represented in Figure 3.23. For both samples, a clear melting peak at 162 °C is evident, which represents the melting temperature of the major lamellae. For the F-PP(An 140C) sample, a shoulder with an onset temperature of 141.5 °C is observed which represents the thickening of lamellae by the annealing process; the onset temperature is corresponding to the annealing temperature. Similar features are also found in the F-PP(An 100C) and F-PP(An 120C) samples (Figure 3.7).

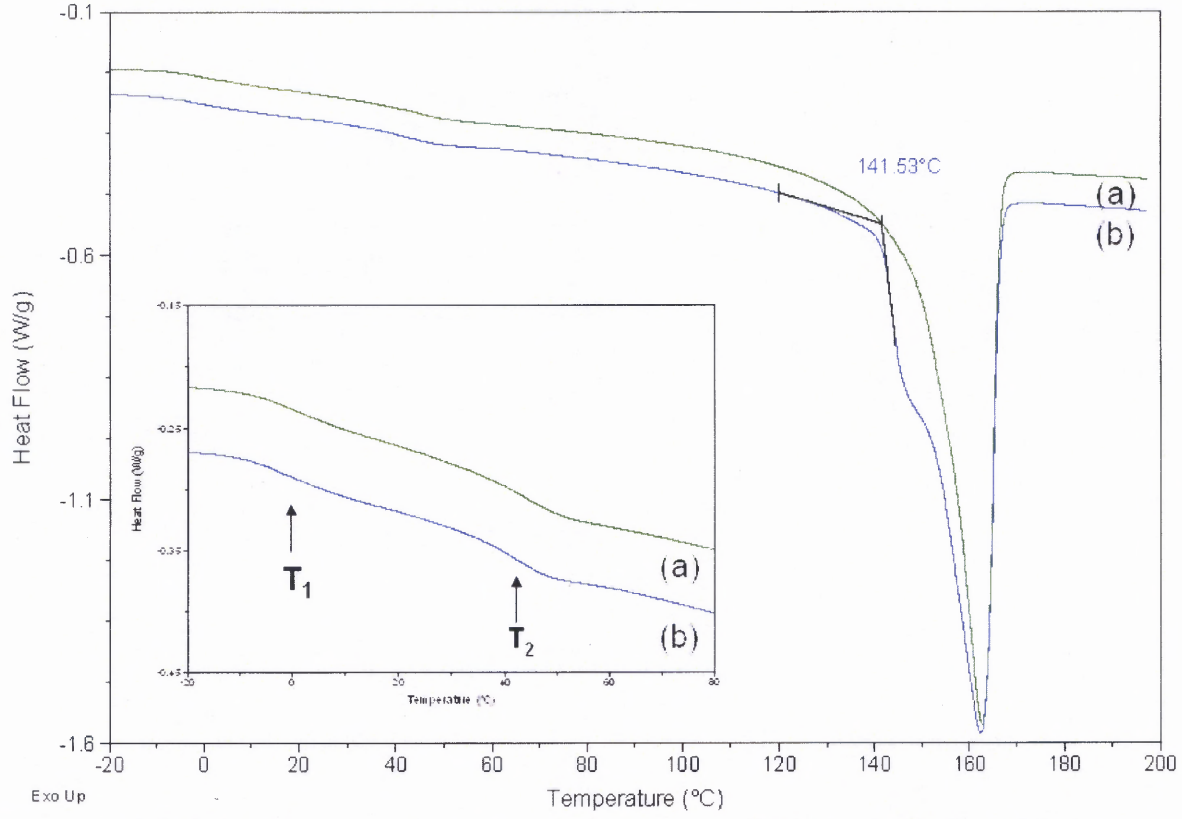

Figure 3.23 DSC heating scan of precursor films (first heating): (a) F-PP, (b) F-PP(An 140C).

As mentioned in Section 3.1.2, a distinct feature of two endothermic discontinuities T_1 and T_2 at 0 °C and 40 °C respectively, was found in both samples (Figure 3.23, insert). In fact, the two discontinuities were found in all precursor films (annealed or non-annealed) (Figure 3.7, insert). After keeping the samples at 230 °C for 10 minutes to erase their thermal history, cooling down to -50 °C and heating for a second time, a single discontinuity is shown at -5 °C (Figure 3.24, insert), and a melting peak at 160 °C (Figure 3.24). The onset of F-PP(An 140C) disappeared in the second heating (Figure 3.24(b)). Thus, it is reasonable to assume that the T_1 of the first scan represented the conventional T_g of polypropylene (-5 °C), and that T_2 is not related to melting of the crystalline domains since it would have

disappeared with annealing at high temperatures. The presence of a second relaxation (above T_g) of PP could be explained with the concept of the rigid-amorphous fraction (RAF).

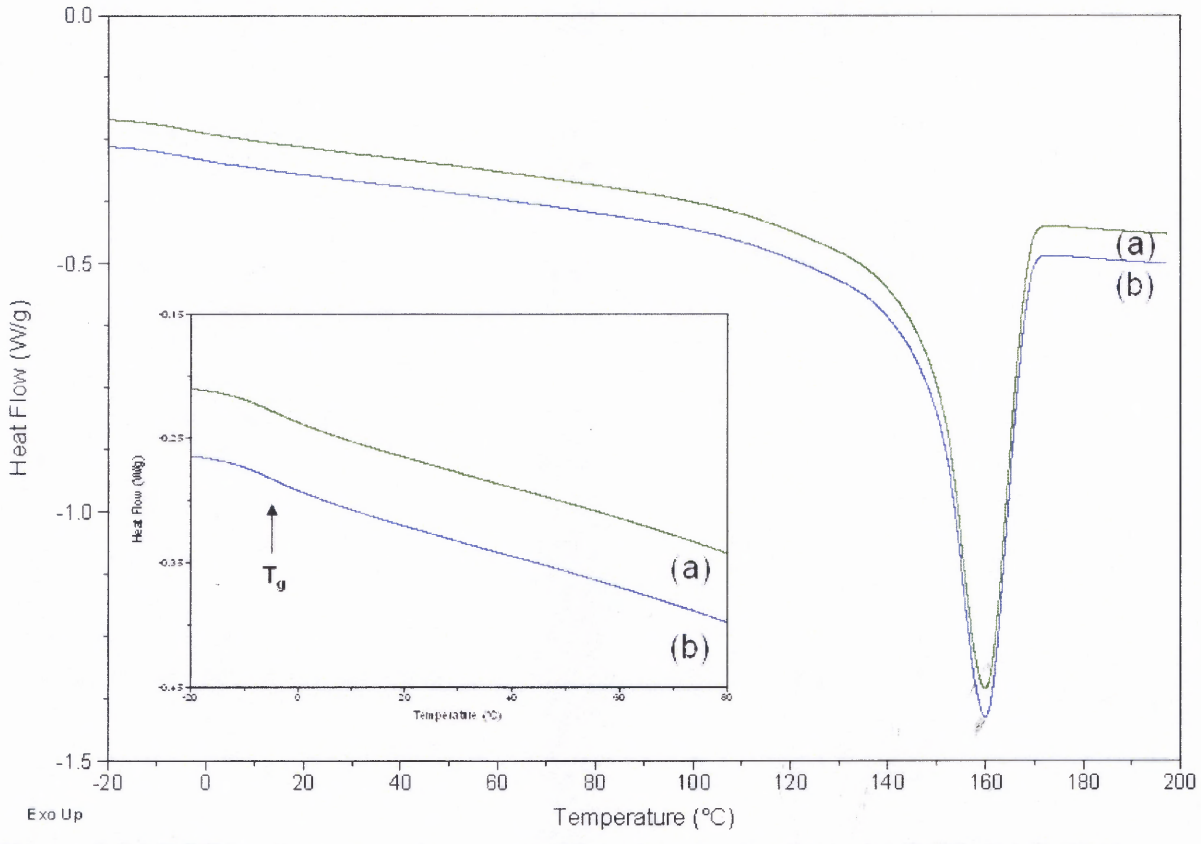

Figure 3.24 DSC heating scan of precursor films (second heating): (a) F-PP, (b) F-PP(An 140C).

The existence of RAF in semicrystalline polymers has been studied for two decades [74, 75]. Since polymer chains are continuous across the amorphous phase and crystalline phase, RAF is an interfacial amorphous layer between these phases, whose chain mobility is restricted due to the locking segments at the crystalline phase (lamellae) (Figure 3.25(a)). As a consequence, the existence of RAF results in an increase in glass transition temperature or its broadening. There is little RAF at the spherulitic boundary due to the more mobile entrant chains from the non-stacked impinged lamellae [76] (Figure 1.8(b)). The amount of

amorphous phase corresponding to the second endothermic discontinuity suggests that RAF is built up inside the spherulites, where the amorphous phase between lamellar stacks should be more restricted due to the intermeshed morphology of R-lamellae and T-lamellae. The resultant confinement by the lamellar structure could be emphasized by the amorphous region surrounded by R-lamellae and T-lamellae that could be called lamellar "wells" (Figure 3.25(b)). The expected high proportion of T-lamellae in the spherulites of the precursor film may be related to fast cooling during the extrusion process.

The effect of stretching temperature on the deformation mechanism of the PP precursor films with significant amount of RAF can then be explained as follows: (1) As the stretching temperature is below T_g, the samples fracture in a brittle manner due to the frozen amorphous phase. (2) As the stretching temperature is between T_g and T_2, the spherulite boundary is flexible but the "lamellar wells" are still rigid due to the high proportion of RAF trapped by T-lamellae and R-lamellae. In the case of weak lamellae (non-annealed sample), the lamellae around the "lamellar wells" are broken and aligned toward the stretching direction. The RAF alone is not strong enough to hold up the morphology. As a result, a typical cold-drawn appearance is shown. However, in the case of strong lamellae (annealed sample), the combined strength of lamellae and RAF is sufficiently high to hold up the "lamellar wells" and the spherulitic morphology; as a result, inter-spherulitic deformation is taken place. (3) As the stretching temperature is higher than T_2, the entire amorphous region is flexible, and the effect of RAF is minimized. The "lamellar wells" can not provide the strength to sustain the morphology. The lamellae could break down or slip from the lamellar knots, which would depend on the strength of the lamellae. As a result, the annealed lamellae can still be oriented without catastrophic cold-drawn deformation.

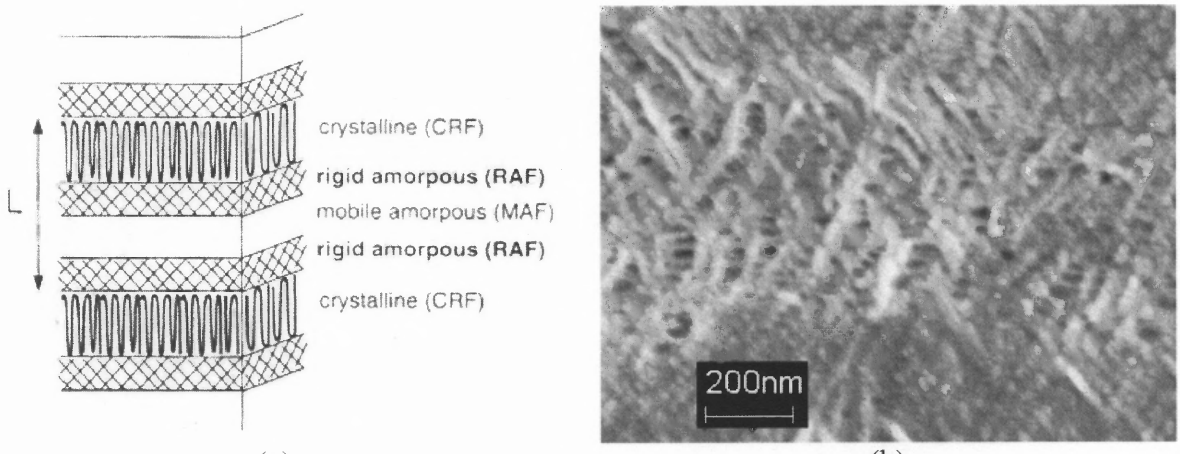

(a) (b)

Figure 3.25 Origin of enhanced RAF in PP precursor films (a) concept of RAF [74] (b) lamellar "well" in the cross-hatched α-PP as a possible source for enhanced RAF.

Figure 3.26 shows the effect of the stretching rate on the α-form orientation index at a stretching temperature of 70 °C. All non-annealed and annealed samples appear highly oriented. Compared to Figure 3.14 where annealed samples showed low orientation at low stretching rates at 25 °C, the results support the proposed role of RAF in preventing intra-spherulitic deformation. The combination of RAF with enhanced strength lamellae seems to form a criterion for initiating inter-spherulitic deformation. The results of α-form orientation index, crystallinity and porosity of samples stretched at 70 °C are summarized in Table 3.8.

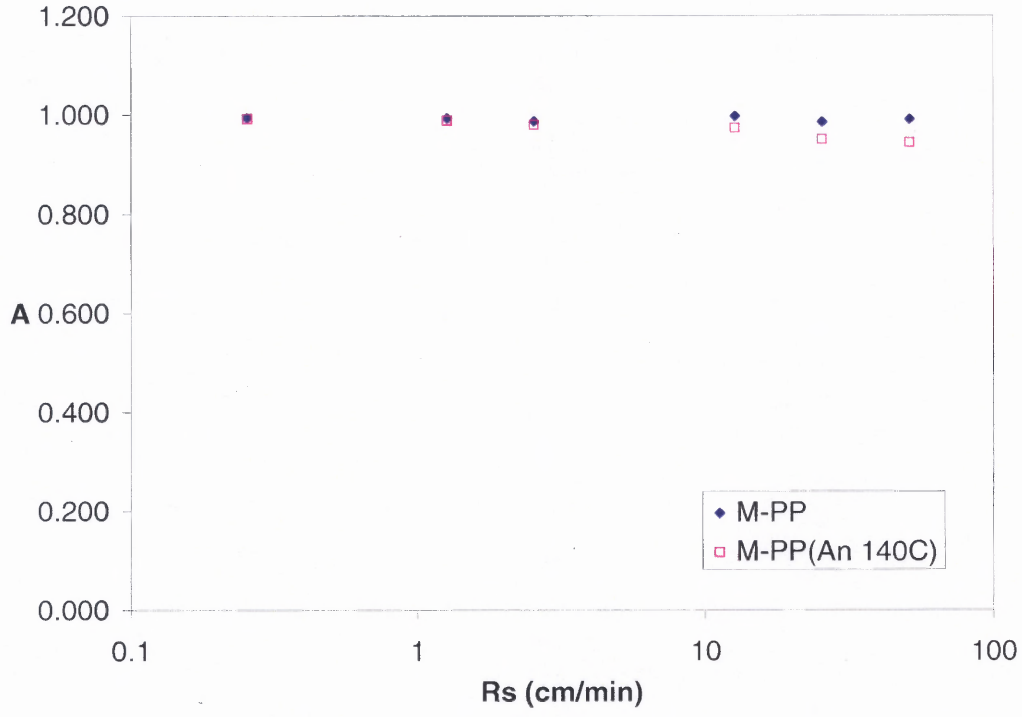

Figure 3.26 α-form orientation index (A) of membranes stretched at different R_S. Stretching conditions were E_S 200% and T_S 70 °C.

Table 3.8 The α-form Orientation Index (A) and Porosity of PP Membranes Stretched at Different Stretching rates (Stretching Temperature 70 °C)

Samples	Stretching conditions			A	Crystallinity (χ_c)	Porosity (ε)
	E_S (%)	R_S (cm/min)	T_S (°C)			
M-PP	200	50.8	70	0.99	0.41	0.03
M-PP	200	25.4	70	0.99	0.42	0.01
M-PP	200	12.7	70	1.00	0.41	0.02
M-PP	200	2.54	70	1.00	N/M*	N/M
M-PP	200	1.27	70	0.99	N/M	N/M
M-PP	200	0.25	70	0.99	N/M	N/M
M-PP(An 140C)	200	50,8	70	0.95	0.49	0.07
M-PP(An 140C)	200	25.4	70	0.95	0.50	0.04
M-PP(An 140C)	200	12.7	70	0.98	0.50	0.05
M-PP(An 140C)	200	2.54	70	0.98	N/M	N/M
M-PP(An 140C)	200	1.27	70	0.99	N/M	N/M
M-PP(An 140C)	200	0.25	70	0.99	N/M	N/M

*N/M is not measured due to uneven surface of the sample at very slow stretching rate.

3.6 Modification I: Nucleated Polypropylene

3.6.1 Precursor Films Characterization

The concept of utilizing inter-spherulitic deformation for creating polypropylene microporous membrane has been validated in the previous discussion. In the proposed method, an important step is to generate strong spherulites in order to utilize the stretching process to create an interconnected porous structure along spherulitic boundaries. Under the inter-spherulitic deformation regime, the size of the spherulite plays an important part for the permeability of the membrane. A modification aimed at reducing spherulite size with a cross-hatched lamellar morphology can be achieved by using α-nucleated polypropylene (PPN). The extrusion conditions of the PPN precursor films were the same as those of the PP precursor films due to their similar rheological characteristics. These PPN precursor films were also subjected to annealing before stretching.

The optical microscope images of the F-PPN sample are shown in Figure 3.27. The polarized optical microscope image of F-PPN does not show any spherulite signs of the spherulite with the Maltese cross pattern (Figure 3.27(b)). This is due to the interference from very small spherulites. Based on the observation of the F-PP sample (Figure 3.2(b) and (d)), the spherulite size can be estimated from the size of the granular-like morphology shown in the optical microscope image. In this case, the granular-like morphology of the F-PPN sample that indicates the spherulite size should be less than 5 μm (Figure 3.27(a)).

The WAXS spectra of the F-PPN samples with or without annealing are shown in Figure 3.28. A clear crystallographic α-form is shown in all precursor films, which is similar to the F-PP samples shown in Figure 3.6. However, the traceable amount of β-form shown in the F-PP sample does not appear in the F-PPN sample, which indicates that the nucleating

agent used in the PPN and can only trigger the formation of the α-form crystal. On the other hand, the weak α_4 peak of the F-PPN samples implies a pre-oriented spherulitic structure in the precursor film which might be due to the early crystallization triggered by the nucleating agent.

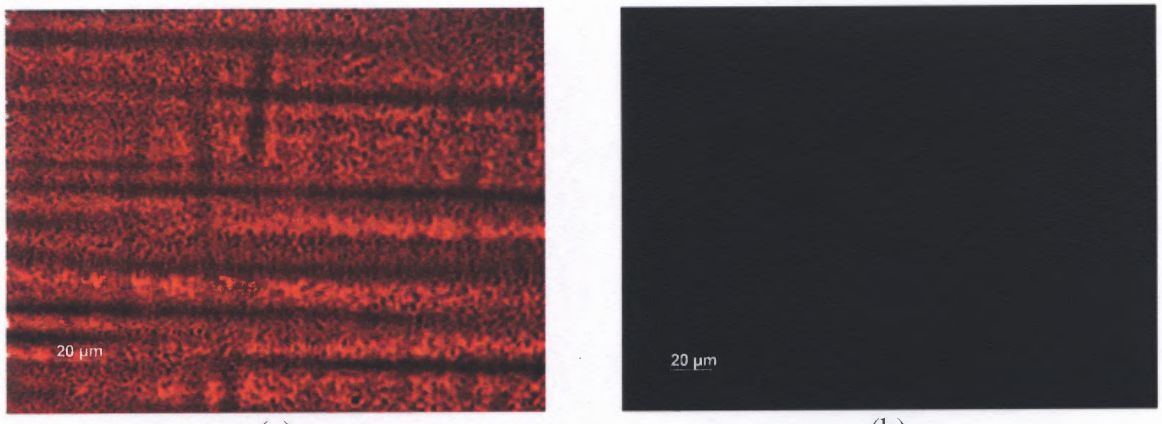

(a) (b)

Figure 3.27 Images of spherulites produced at low stress conditions (F-PPN) (400X): (a) optical microscope images, (b) polarized optical microscope images.

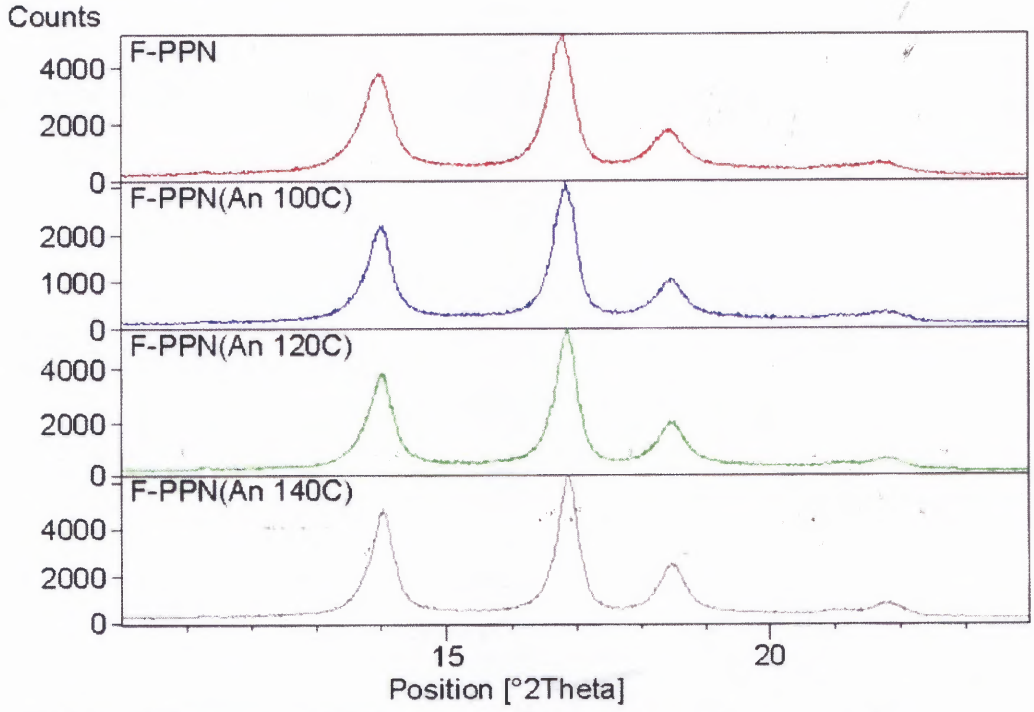

Figure 3.28 WAXS spectra of PPN precursor films with or without annealing.

Figure 3.29 shows DSC heating curves of the PPN precursor films with and without the annealing treatment. The results of melting temperatures and crystallinity of these samples are summarized in Table 3.9. The melting temperature of F-PPN is about 157 °C, and is close to that of F-PP sample. Annealing increases crystallinity, however, the main melting peak is almost unchanged. The slightly lower melting temperature and crystallinity of F-PPN samples might be due to the effect of less perfect packing. It is known that the crystallization temperature of the nucleated PP is higher than that of the non-nucleated PP. The crystallization temperature of PPN is about 130 °C and that of PP is about 113 °C (Figure 3.30). In PPN, the number of nucleating sites is increased dramatically and the growth of lamellae is limited by their interference from one another.

Similarly to the F-PP samples, a discontinuity appears in all F-PPN samples and the onset of the discontinuity is related to the annealing temperature. As previous discussion in Section 3.1.2, this discontinuity represents the result of lamellae thickening during annealing. In addition, the existence of a second endothermic discontinuity (T_2) is also shown in the F-PPN samples (Figure 3.29, insert). This provides another proof for the presence of the amplified RAF due to the cross-hatched lamellar morphology of α-form.

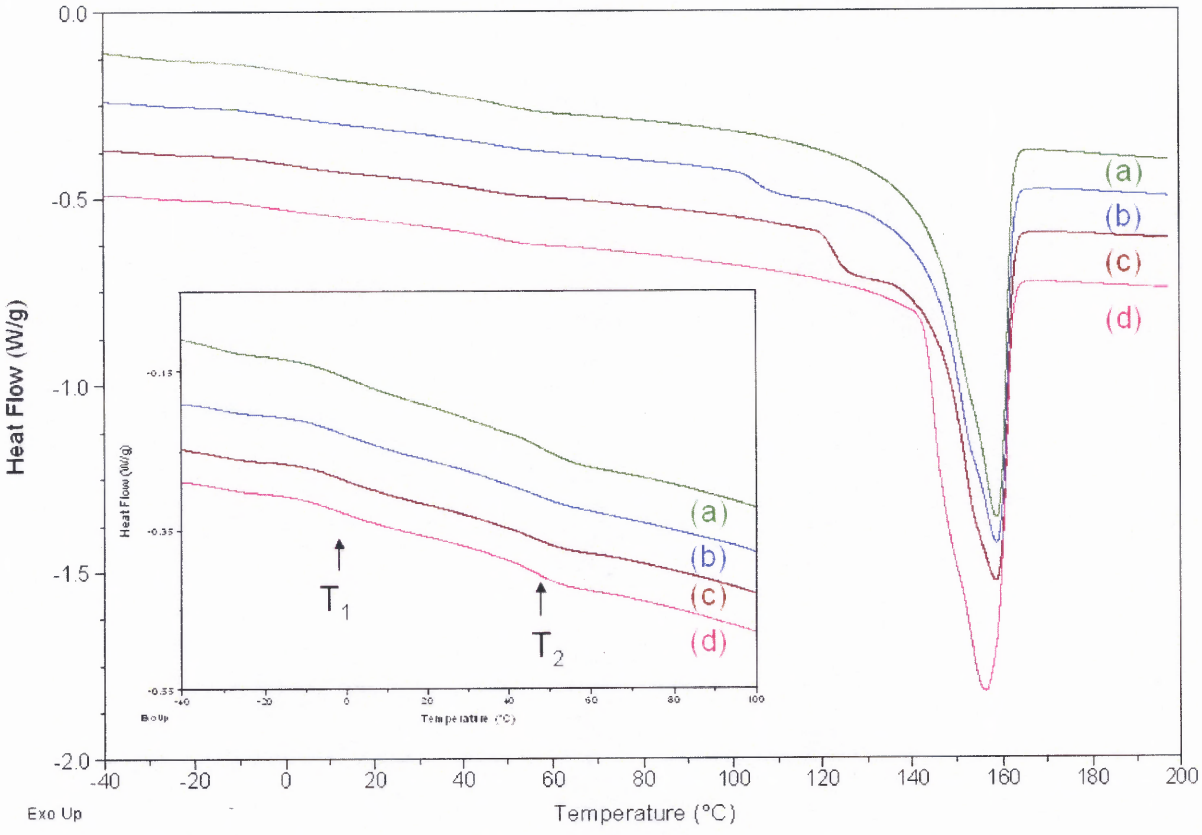

Figure 3.29 DSC heating curves of PPN precursor films: (a) F-PPN, (b) F-PPN(An 100C), (c) F-PPN(An 120C), (d) F-PPN(An 140C).

Table 3.9 Thermal Analysis of PPN Precursor Films

Samples	Onset of the discontinuity (°C)	T_m (°C)	Crystallinity (χ_c)
F-PPN	NA	157.9	0.43
F-PPN(An 100C)	101.9	158.0	0.44
F-PPN(An 120C)	120.2	157.5	0.46
F-PPN(An 140C)	142.9	156.4	0.49

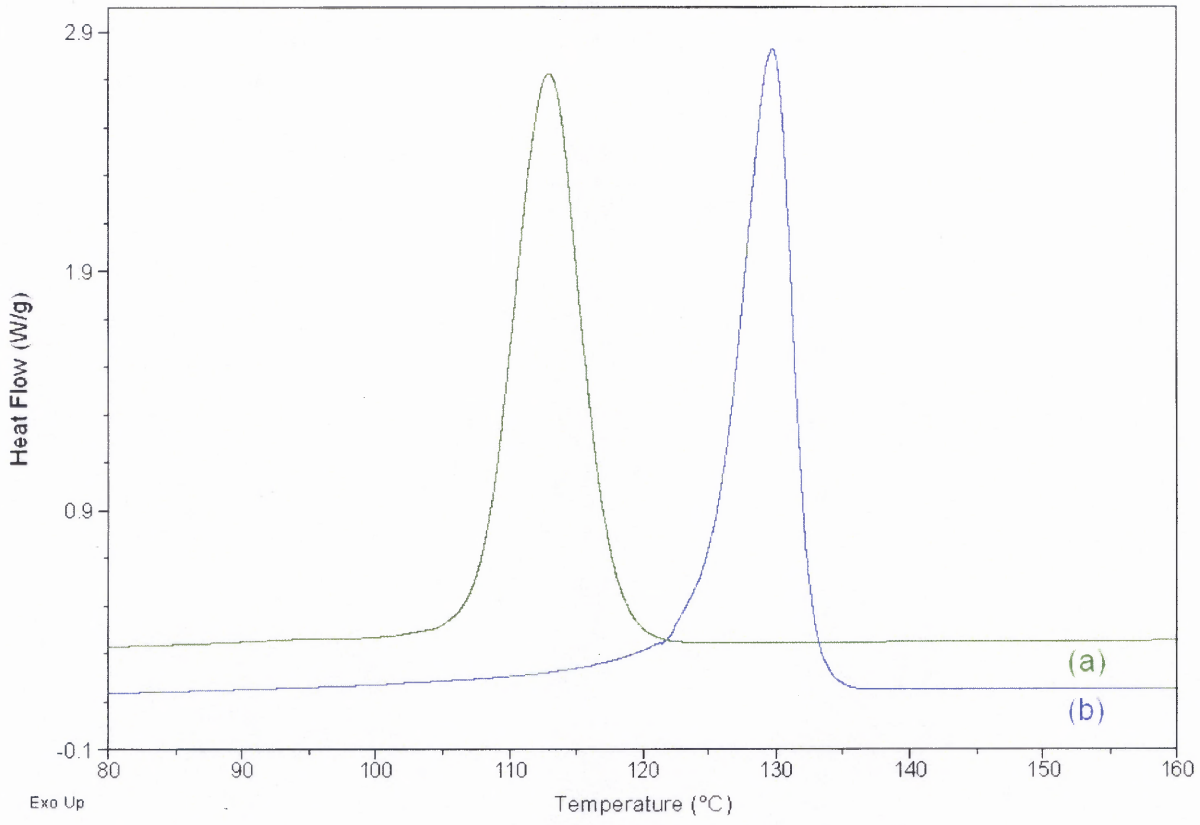

Figure 3.30 DSC cooling curves of PPN precursor films: (a) PP, (b) PPN.

3.6.2 Stretched Membranes Characterization

From the characterization of the precursor films, the F-PPN samples exhibit very similar lamellar characteristics as those in the F-PP samples except of their smaller spherulite size. The stretching conditions of M-PPN samples were the same as those in the M-PP samples, i.e. R_S = 12.7 cm/min, E_S = 200%, and T_S = 25 °C. The macroscopic visual images of stretched PPN membranes are shown in Figure 3.31. A transition of the membrane appearance with increasing annealing temperatures (from transparent to opaque) is observed, which resembles that of the stretched PP membranes shown in Figure 3.8. As discussed earlier, opacity seems to represent the occurrence of inter-spherulitic deformation. However,

a morphological examination of the stretched membrane by optical microscope (Figure 3.32) did not show this difference due to the presence of very small spherulites.

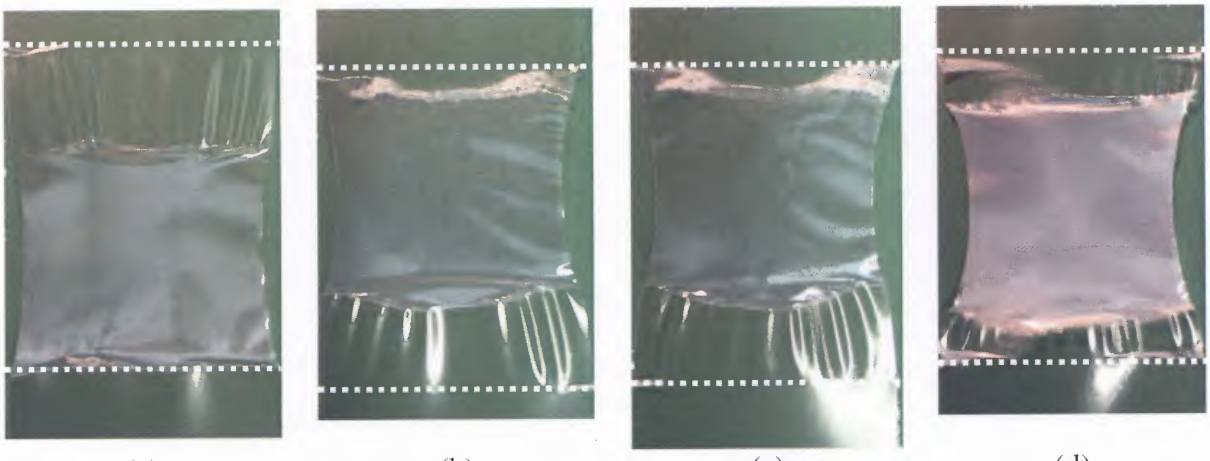

(a) (b) (c) (d)

Figure 3.31 Images of stretched PPN membranes: (a) M-PPN, (b) M-PPN(An 100C), (c) M-PPN(An 120C), (d) M-PPN(An 140C), (the clamp positions are indicated by white dotted lines)

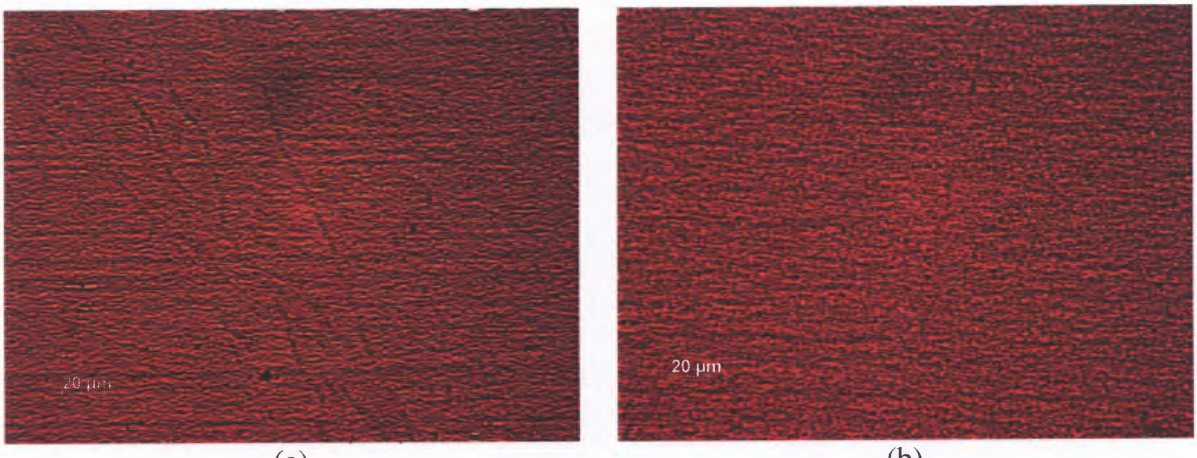

(a) (b)

Figure 3.32 Optical microscope images of PPN stretched membranes (400X): (a) M-PPN, (b) M-PPN(An 140C).

SEM images of M-PPN(An 140C) are shown in Figure 3.33. Discrete dark regions surrounded by continuous bright ones are shown in Figure 3.33(a), and this seems to confirm the occurrence of inter-spherulitic deformation. The lamellar openings (pores) are evident in

Figure 3.33(b), and the dimensions of these pores (50~100 nm) are about the same as in the M-PP(An 140C) sample (Figure 3.13(b)).

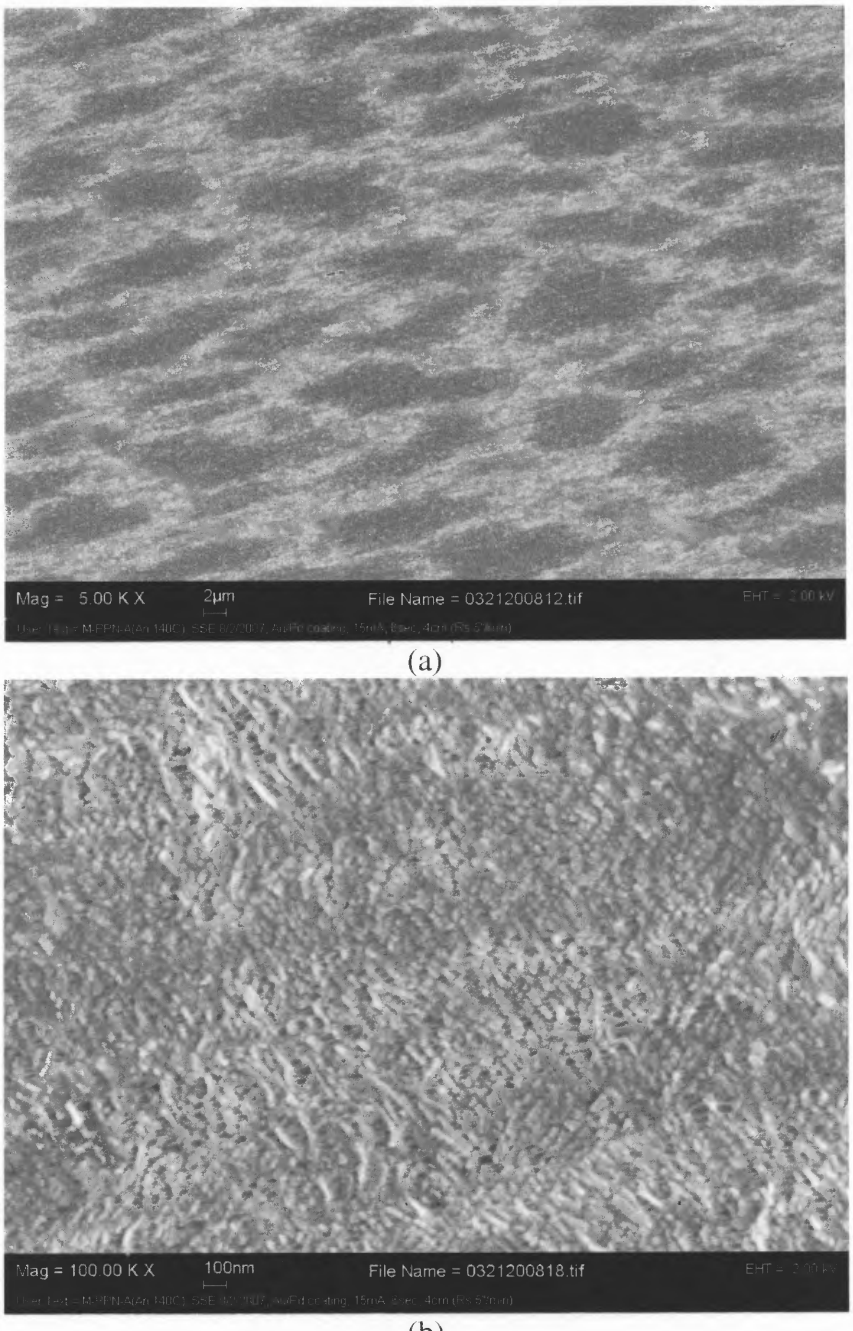

(a)

(b)

Figure 3.33 SEM images of M-PPN(An 140C). (a) 5000X. (b) 100000X.

The occurrence of inter-spherulitic deformation in the M-PPN(An 140C) sample can be confirmed by WAXS examination as shown earlier for the M-PP(An 140C) sample through the presence of the α_4 peak. Crystallographic examination is particularly useful in this case since morphological examination would be limited by the small spherulite size with non-distinct spherulite boundaries. Furthermore, crystallographic examination detects the transition on a lamellar scale of the entire sample, and is not influenced by other characteristics present on the sample surface. The WAXS spectra of the PPN samples are shown in Figure 3.34. The presence of the α-form is evident in the PPN precursor films (Figure 3.28). The transition of the membrane appearance (from transparent to opaque) in Figure 3.31 implies the occurrence of inter-spherulitic deformation in the M-PPN(An 140C) sample. As expected, the α_4 peak appears only in the M-PPN(An 140C) sample. The disappearance of the α_4 peak in the M-PPN, M-PPN(An 100C) and M-PPN(An 120C) samples is consistent with the oriented appearance shown in Figure 3.31.

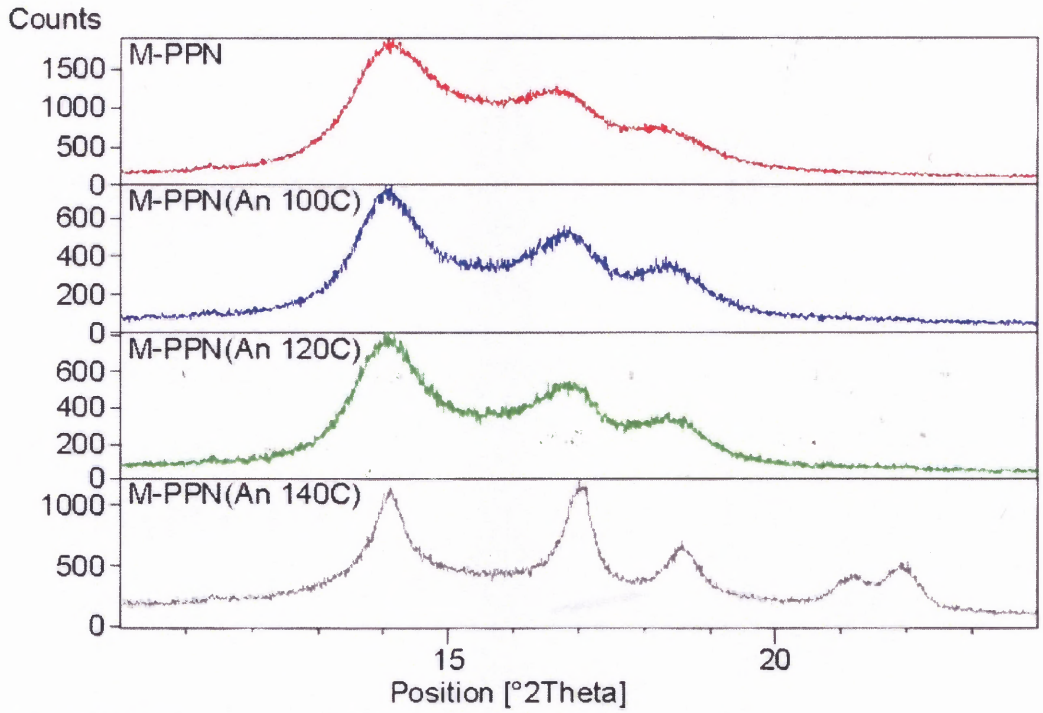

Figure 3.34 WAXS spectra of PPN stretched membranes.

Thermal analysis and methanol permeation results of the PPN samples are shown in Table 3.10. Similarly to the trend observed in the PP samples (Table 3.3), the crystallinity increased with increasing annealing temperature, and slightly decreased after stretching. Interestingly, there was almost no methanol permeation in the oriented PPN samples (M-PPN, M-PPN(An 100C) and M-PPN(An 120C)) as also observed in the M-PP(An 120C) sample (Table 3.3). This may imply that the formation of the cracks which caused high methanol permeation in the other oriented PP samples (M-PP and M-PP(An 100C)) is limited in the case of PPN samples. On the other hand, a dramatic increase in methanol permeation was found in the M-PPN(An 140C) sample. The porosity estimations of stretched PPN membranes shown in Table 3.11 are also increased dramatically to 0.29 due to the occurrence of inter-spherulitic deformation.

The results of methanol permeation of M-PP samples can be better comprehended by comparing with M-PPN samples. The comparison by using α-form orientation index and methanol permeation is shown in Figure 3.35. The occurrence of inter-spherulitic deformation can be identified from the low A values of the M-PP(An 140C) (Figure 3.35(a)) and M-PPN(An 140C) (Figure 3.35(c)) samples. The high A values of other samples represent the predominant intra-spherulitic deformation. The separated lamellar structure of intra-spherulitic deformation can not be utilized as effective porosity because of the random location of the pores after fibrillation. Therefore, the regained methanol permeation in the M-PP(An 140C) sample and the significant increase in permeation of the M-PPN(An 140C) sample are based on same mechanism, i.e. the inter-spherulitic deformation.

Table 3.10 Thermal Analysis and Methanol Permeation of PPN Precursor Films and Stretched Membranes

Properties	T_m (°C)	Crystallinity (χ_c)	*Methanol permeation (l/m^2hr)[a]
Precursor films (F)			
F-PPN	157.9	0.43	No permeation
F-PPN(An 100C)	158.0	0.44	No permeation
F-PPN(An 120C)	157.5	0.46	No permeation
F-PPN(An 140C)	156.4	0.49	No permeation
Stretched membranes (M)			
M-PPN	161.9	0.41	<0.1
M-PPN(An 100C)	158.9	0.42	<0.1
M-PPN(An 120C)	158.1	0.44	<0.1
M-PPN(An 140C)	158.6	0.46	18.7 ± 2.2

* The methanol permeation results were based on the average of four measurements.

Table 3.11 Porosity Estimation of Stretched PPN Membranes

Properties	*χ_c	ρ_{cal} (g/cm^3)	**t (μm)	V_M (mm^3)	M_M (mg)	V_{cal} (mm^3)	Porosity (ε)
M-PPN	0.41	0.892	17	30.3	26.1	29.1	0.04
M-PPN(An 100C)	0.42	0.893	18	32.1	28.2	31.3	0.02
M-PPN(An 120C)	0.44	0.895	16	28.5	24.1	26.8	0.06
M-PPN(An 140C)	0.46	0.897	33	58.8	41.3	45.7	0.29

* Crystallinity measurement to calculate porosity was based on one sample having methanol permeation value close to the averaged value shown in Table 3.10.
** "t" is the thickness of stretched membrane.

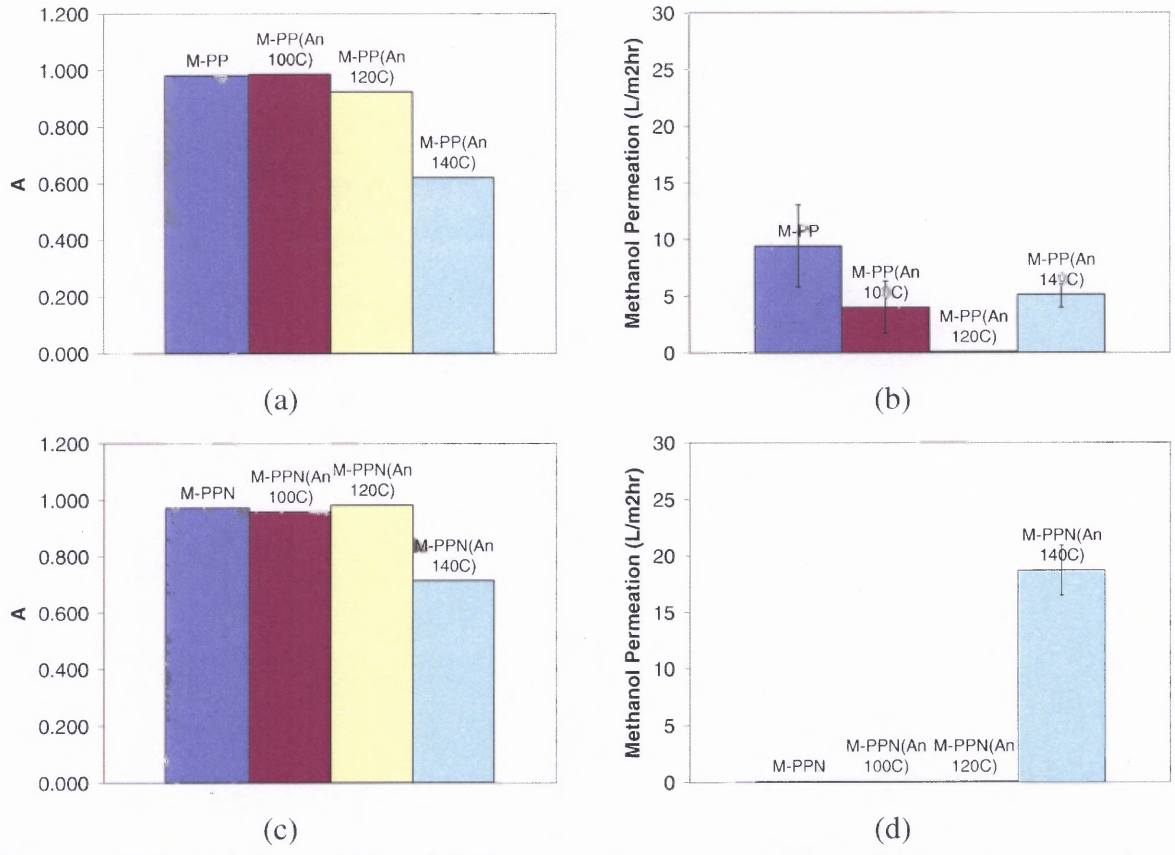

Figure 3.35 Comparison of PP and PPN stretched membranes: (a) α-form orientation index of M-PP samples, (b) methanol permeability of M-PP samples, (c) α-form orientation index of M-PPN samples, (d) methanol permeability of M-PPN samples.

The effect of stretching ratio on the M-PPN and M-PPN(An 140C) samples is shown in Figure 3.36 and Figure 3.37, and the porosity of these membranes is summarized in Table 3.11. A surprising similarity between the PP and the PPN systems validate the previous discussion on the selecting of processing conditions for inter-spherulitic deformation.

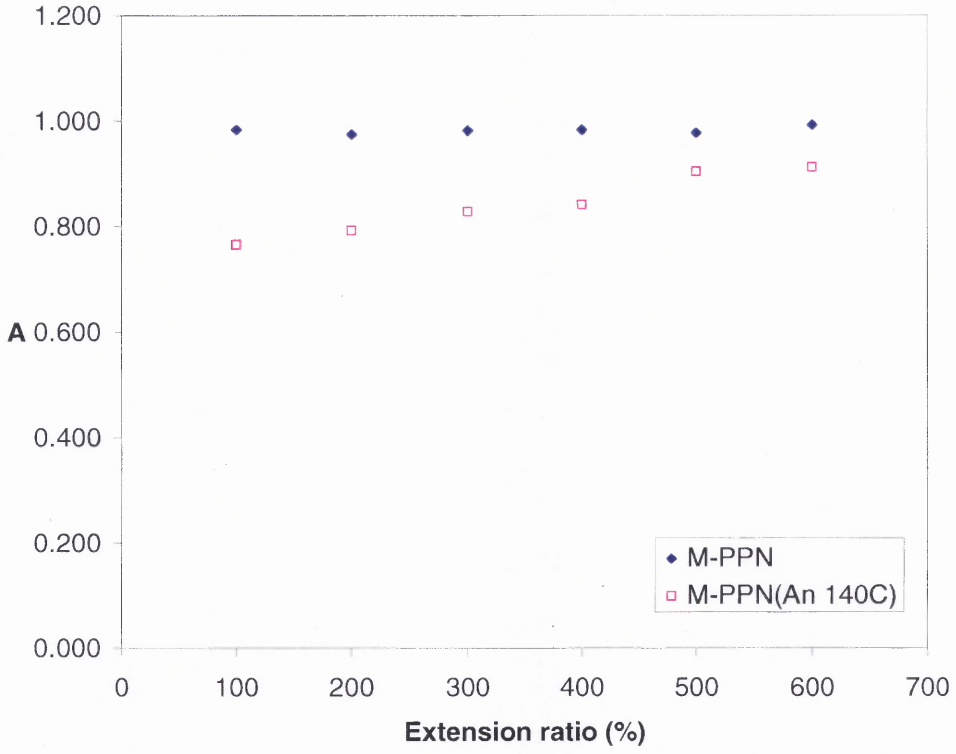

Figure 3.36 α-form orientation index (A) of PPN membranes stretched at different E_S. Stretching conditions were R_S 12.7 cm/min and T_S 25 °C.

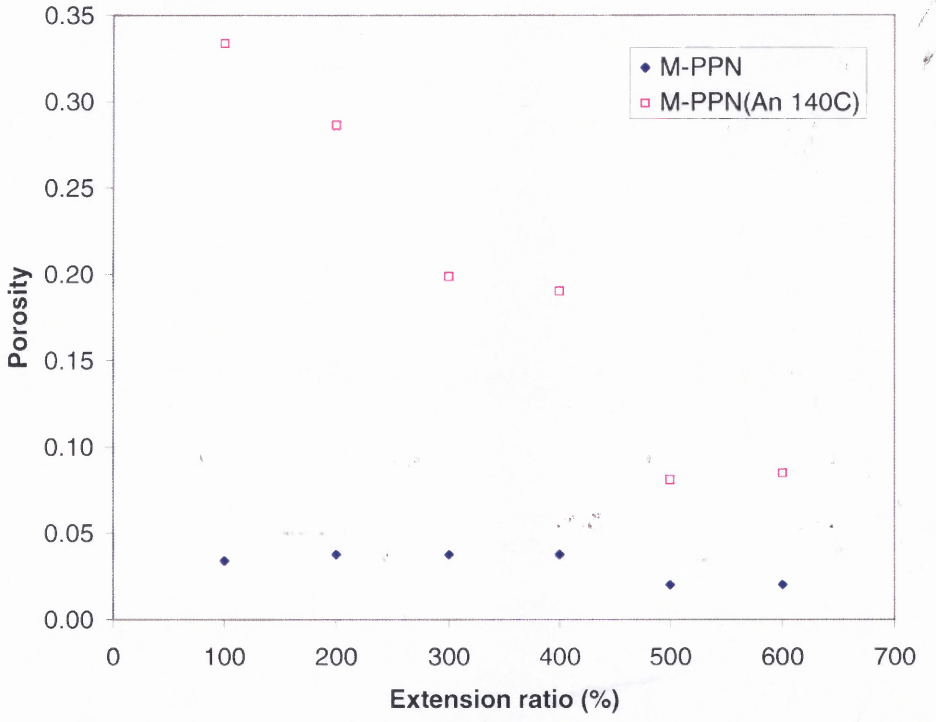

Figure 3.37 Porosity of PPN membranes stretched at different E_S. Stretching conditions were R_S 12.7 cm/min and T_S 25 °C.

Table 3.12 The α-form Orientation Index (A) and Porosity of PPN Membranes Stretched at Different Stretching Ratios.

Samples	Stretching conditions			A	Crystallinity (χ_c)	Porosity (ε)
	E_S (%)	R_S (cm/min)	T_S (°C)			
M-PPN	100	12.7	25	0.98	0.40	0.03
M-PPN	200	12.7	25	0.98	0.40	0.04
M-PPN	300	12.7	25	0.98	0.39	0.04
M-PPN	400	12.7	25	0.98	0.40	0.04
M-PPN	500	12.7	25	0.98	0.39	0.02
M-PPN	600	12.7	25	0.99	0.40	0.02
M-PPN(An 140C)	100	12.7	25	0.77	0.45	0.33
M-PPN(An 140C)	200	12.7	25	0.79	0.44	0.29
M-PPN(An 140C)	300	12.7	25	0.83	0.45	0.20
M-PPN(An 140C)	400	12.7	25	0.84	0.44	0.19
M-PPN(An 140C)	500	12.7	25	0.91	0.44	0.08
M-PPN(An 140C)	600	12.7	25	0.91	0.44	0.08

The stress-strain curves of the M-PP(An 140C) and M-PPN(An 140C) samples along the machine (MD) and transverse directions (TD) are shown in Figure 3.38. Both membranes have high MD tensile strength and lower TD tensile strength. Along the MD, the M-PPN(An 140C) sample is stronger than the M-PP(An 140C) sample but fails at the lower strain (90% versus 120%). Along the TD, both samples show similar ductile behavior and can be drawn up to 500% of their original length. These results seem inconsistent with the assumption of better biaxial mechanical properties due to spherulitic morphology. However, the presence of a spherulitic structure in the PP and PPN stretched membranes is evident from the low α-form orientation index (Figure 3.14 and Figure 3.34). The low strength in the TD might be due to the presence of pre-oriented spherulitic structures as showing by the relatively high α-form orientation index in the precursor films (Figure 3.6 and Figure 3.28). As a result, the different tensile strength values in MD and TD show the importance of generating a less pre-oriented spherulitic morphology to ensure better biaxial mechanical properties.

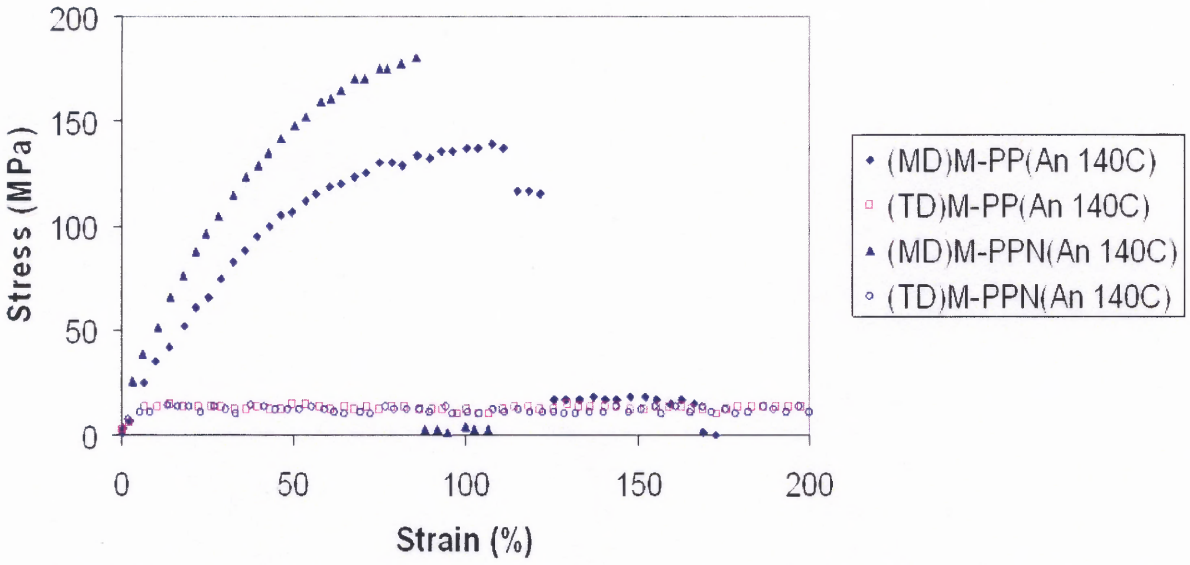

Figure 3.38 Stress-strain curve of the M-PP(An 140C) and M-PPN(An 140C) samples along machine direction (MD) and transverse direction (TD). (the sample gap was 1.3 cm, and the sample was stretched by 2.5 cm/min at 25 °C).

3.7 Modification II: Immiscible blend

Modification II of the proposed membrane fabrication method is to create a permeation shortcut by utilizing a debonded morphology around foreign particles as shown in Figure 3.13(c). The population of the foreign particles can be increased dramatically by adding an artificial impurity such as an immiscible polymer or inorganic fillers. There are two reasons for choosing PS as a second phase. Firstly, PS has relatively high glass transition temperature (100 °C) and is less-deformable during room temperature stretching conditions. Secondly, the PP/PS viscosity ratio is about unity over a wide range of shear rates, which meets the requirements for good dispersion [60]. The PP/PS 90/10 blend was mixed by dry blending, and a twin screw intermeshing extruder was used to improve the quality of compounding. The PPN/PS 90/10 blend was compounded under the same conditions due to the similar rheological properties of PPN to PP. The SEM images of the fracture surfaces of pellets of

PP/PS and PPN/PS blends shown in Figure 3.39 indicate a fine PS phase with a size of about 1μm that is well-dispersed in both systems. The blends were then extruded into films, annealed and stretched at the same conditions used in the PP and PPN systems.

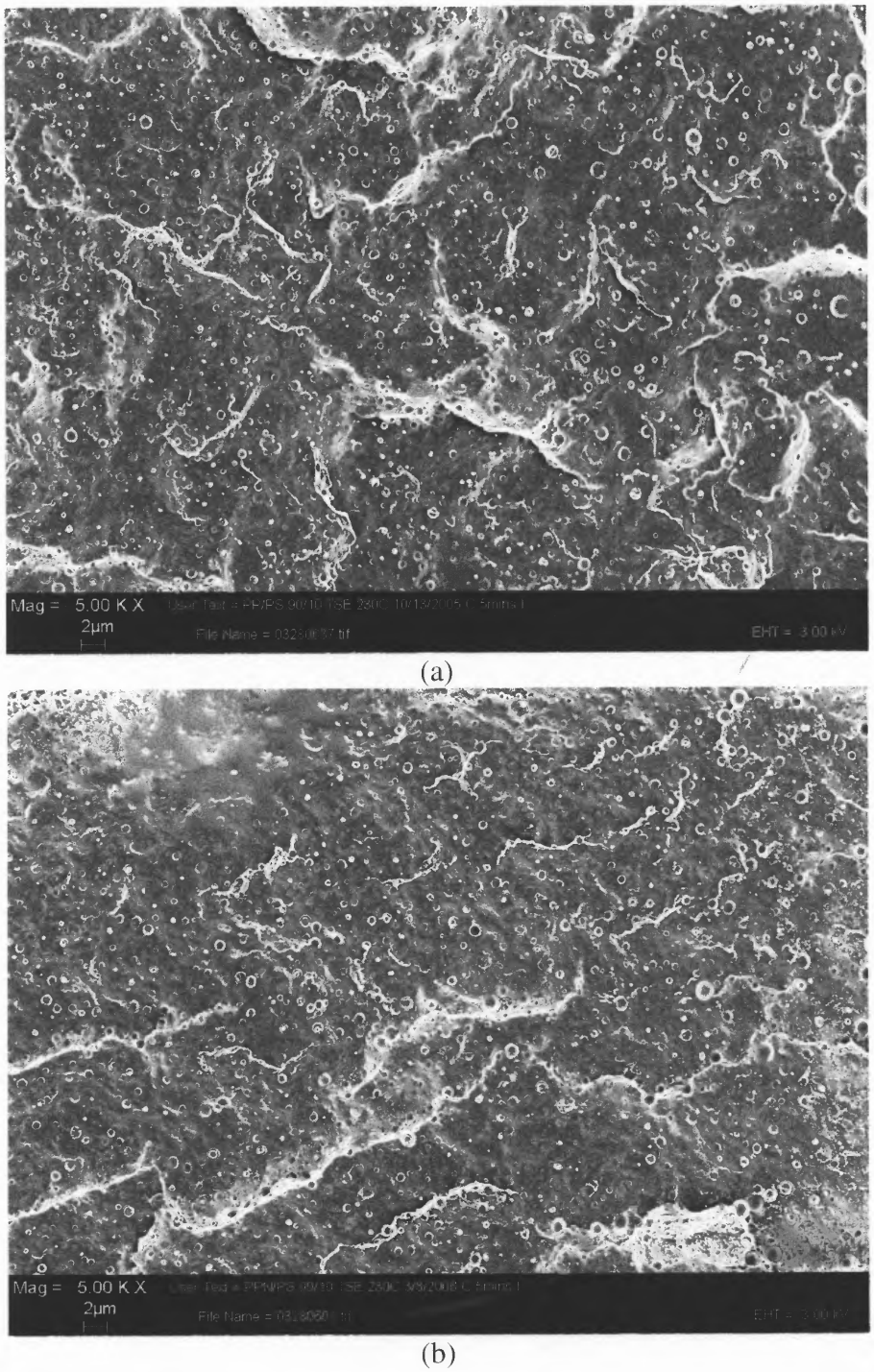

Figure 3.39 SEM image of fracture surface of immiscible blends (5000X): (a) PP/PS 90/10 by weight, (b) PPN/PS 90/10 by weight.

SEM images of the PP/PS and PPN/PS stretched membranes are shown in Figure 3.40. The highlights of debonding morphology are shown in Figure 3.41. From previous discussions, inter-spherulitic deformation only occurs in the precursor films annealed at 140 °C. In all samples, a debonded morphology around the dispersed PS phase is evident. The degree of debonding depends on the size of dispersed phase as a result of the stress concentration around the dispersed phase. Furthermore, the occurrence of premature debonding around the larger dispersed phase restricts the occurrence of debonding around other smaller dispersed domains. Thus, a narrow size distribution of the dispersed phase seems to be important to ensure a uniform debonded morphology.

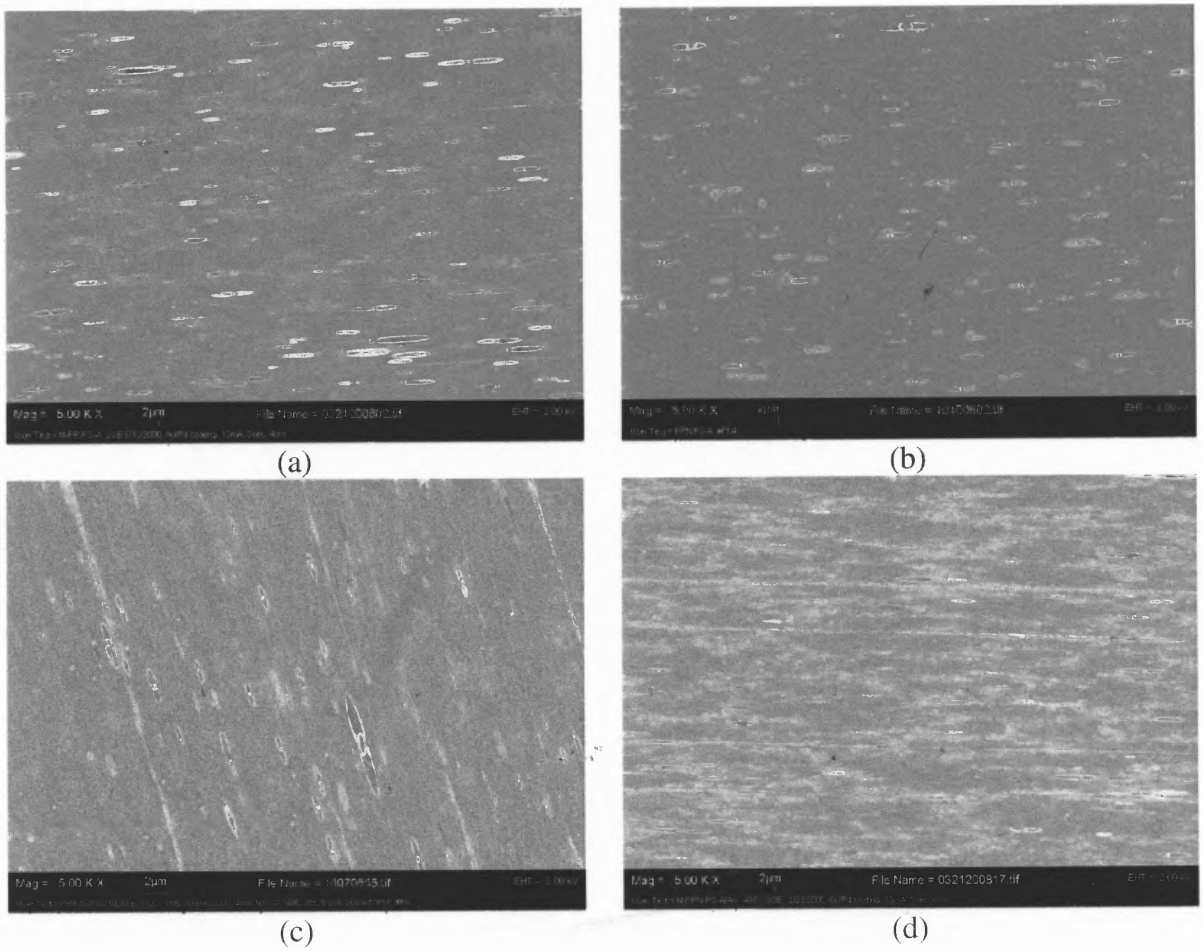

Figure 3.40 SEM images of stretched membrane prepared with immiscible blends (5000X): (a) M-PP/PS, (b) M-PP/PS(An 140C), (c) M-PPN/PS, (d) M-PPN/PS(An 140C) .

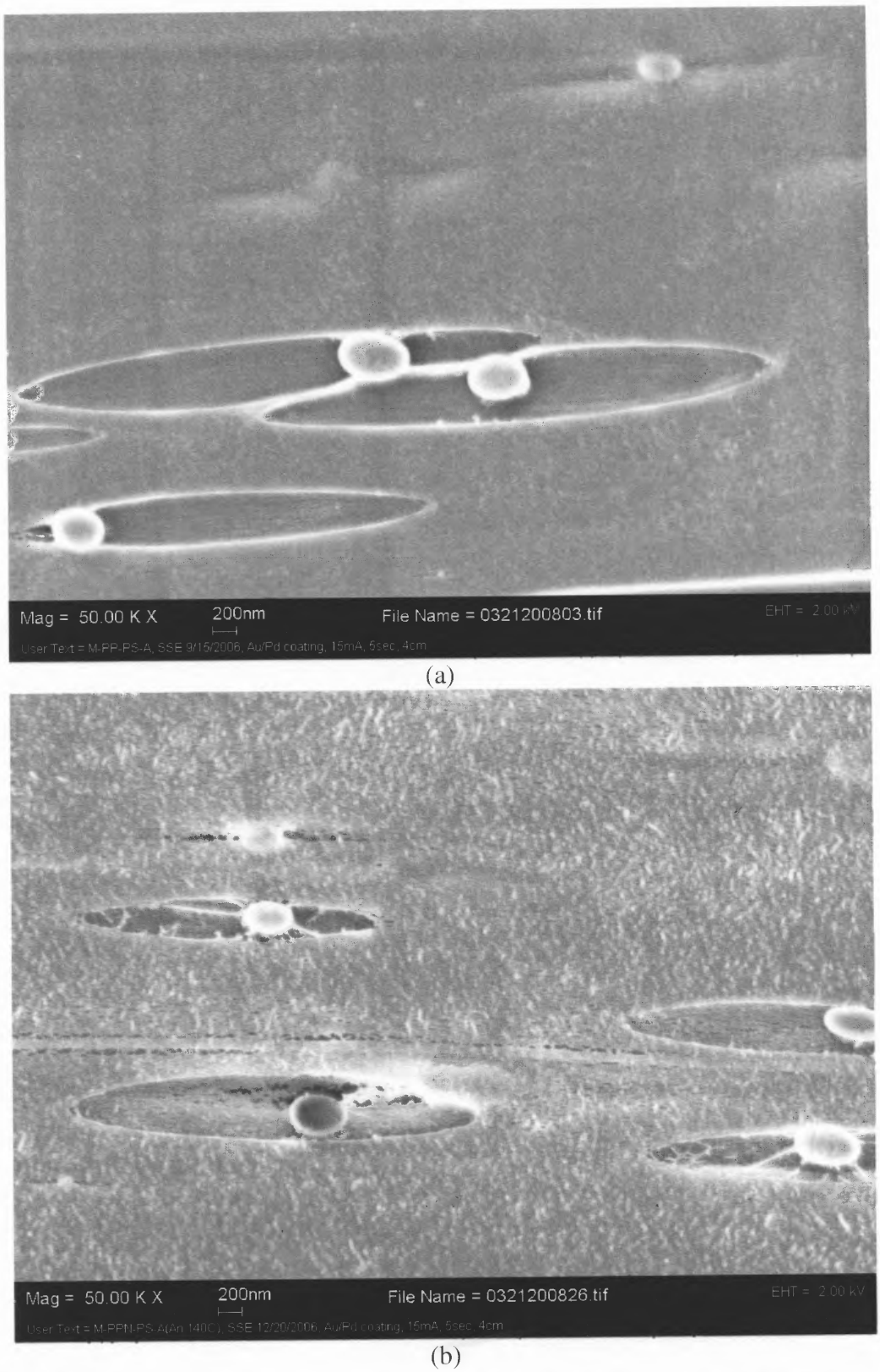

Figure. 3.41 SEM images of debonded morphology (50000X): (a) M-PP/PS, (b) M-PP/PS(An 140C).

Debonding affects the deformation of the PP matrix phase in several ways. A precursor film made of an immiscible blend is shown in Figure 3.42(a). In the stretched membranes (Figures 3.42(b), (c) and (d)), a blank matrix represents the occurrence of intra-spherulitic deformation (this resembles the non-permeable membrane) and a mesh matrix represents the occurrence of inter-spherulitic deformation (this resembles the highly permeable membrane of the sample annealed at 140 °C). The debonded morphology is only useful when inter-spherulitic deformation is assured.

Case I (Figure 3.42(b) represents good-adhesion between matrix and dispersed phase. The presence of the dispersed phase increases the stress level in the membrane during the stretching process and promotes the occurrence of inter-spherulitic deformation. Therefore, there is no permeation short-cut in this case. Case II (Figure 3.42(c) represents poor-adhesion between matrix and dispersed phase (this is often the case in an immiscible blend). The formation of debonded morphology compensates for the energy absorbed by stretching and limits the occurrence of inter-spherulitic deformation, and as a result, limits the permeability of membrane. Case III (Figure 3.42(d) represents a combination of debonded morphology and inter-spherulitic deformation. The membrane should have high permeability and still show confined porous structure as the loading of dispersed phase lowing than percolation threshold.

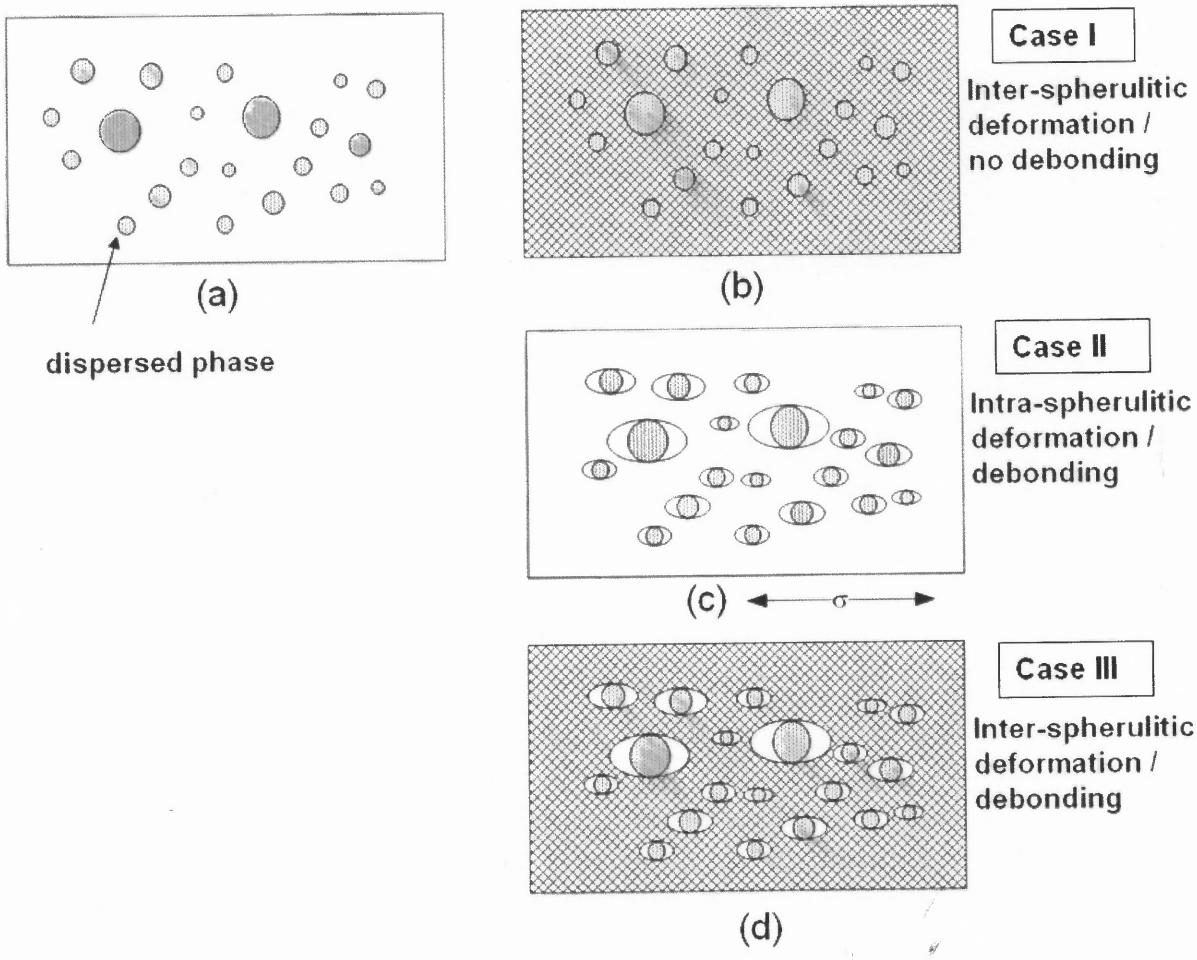

Figure 3.42 Schematic representation of debonding and inter/intra- spherulitic deformation.

The WAXS spectra of the stretched membranes based on the PP/PS blend are shown in Figure 3.43. The presence of PS does not affect the WAXS spectrum due to its amorphous nature. The results of the precursor blend films are similar to those of the α-form predominant PP films. The results of the stretched blend membranes show a weak signal for plane group II even if the sample was annealed at 140 °C (Figures 3.41(d) and (f)), which implies the lack of inter-spherulitic deformation. This might be due to the effect of energy compensation by the occurrence of debonding.

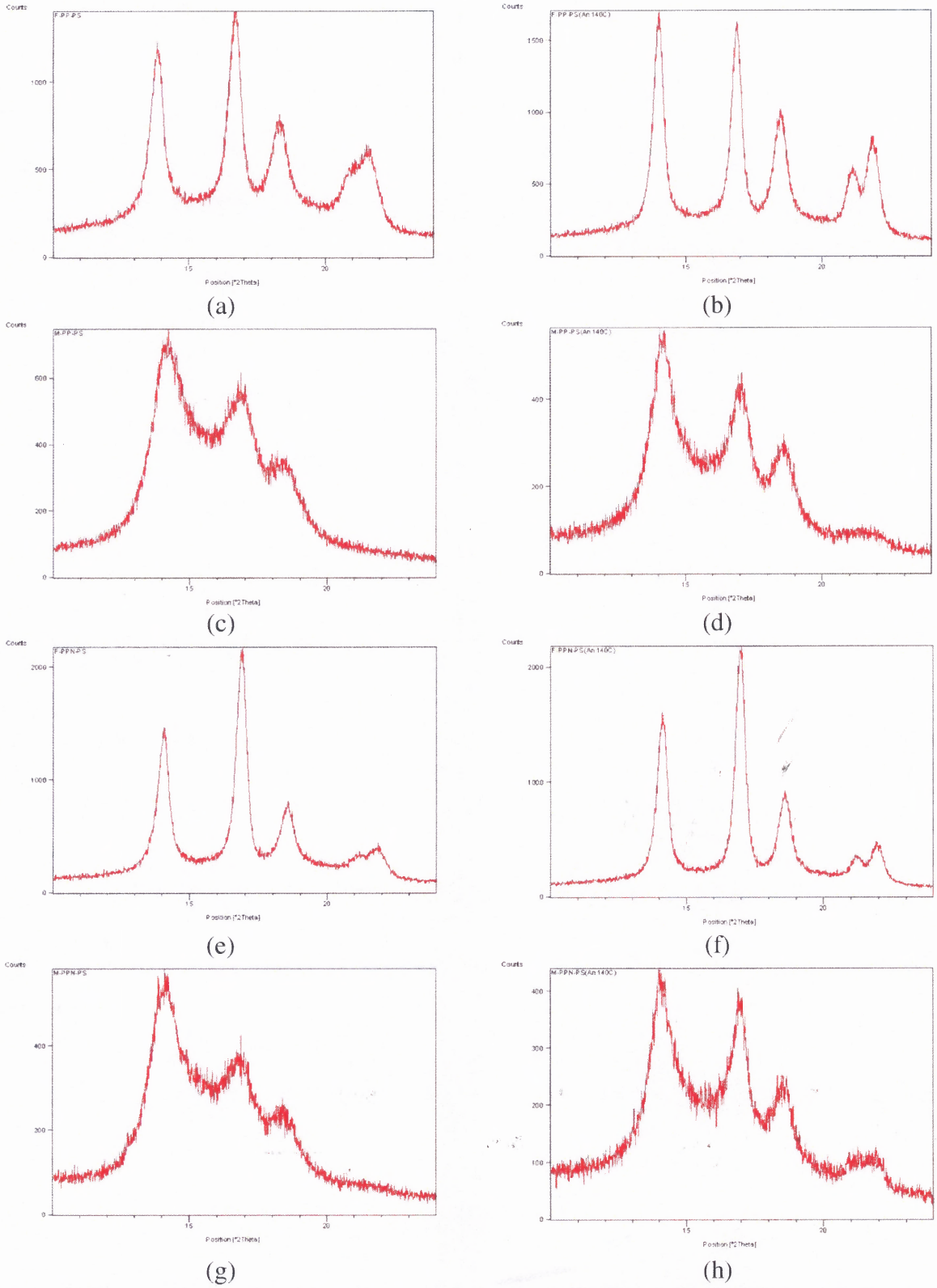

Figure 3.43 WAXS spectra of immiscible blends: (a) F-PP/PS, (b) F-PP/PS(An 140C), (c) M-PP/PS, (d) M-PP/PS(An 140C), (e) F-PPN/PS, (f) F-PPN/PS(An 140C), (g) M-PPN/PS, (h) M-PPN/PS(An 140C).

The α-form orientation index and methanol permeation of the stretched blend membranes are shown in Figure 3.44. Comparing with the results of the PP films (Figure 3.35), a higher orientation observed in the blends has relatively high methanol permeation. In this case, the methanol permeation which represents the membrane interconnectivity is quite complicated due to the interaction between debonding and intra/inter-spherulitic deformation. The results of the membrane characterization are summarized in Table 3.13 and Table 3.14. In general, the porosity of M-PP/PS and M-PPN/PS samples are higher than those of the M-PP and M-PPN samples due to the debonded morphology. However, no clear conclusion on the effect of annealing on porosity can be drawn at this moment. The relatively low methanol permeation in the M-PP/PS and M-PP/PS(An 140C) samples (Figure 3.42(b)) might represent the combination of debonding with a limited intra/inter-spherulitic deformation. On the other hand, the high methanol permeation in the M-PPN/PS(An 140C) sample might represent the optimum combination of these structures as shown in Figure 3.42(d).

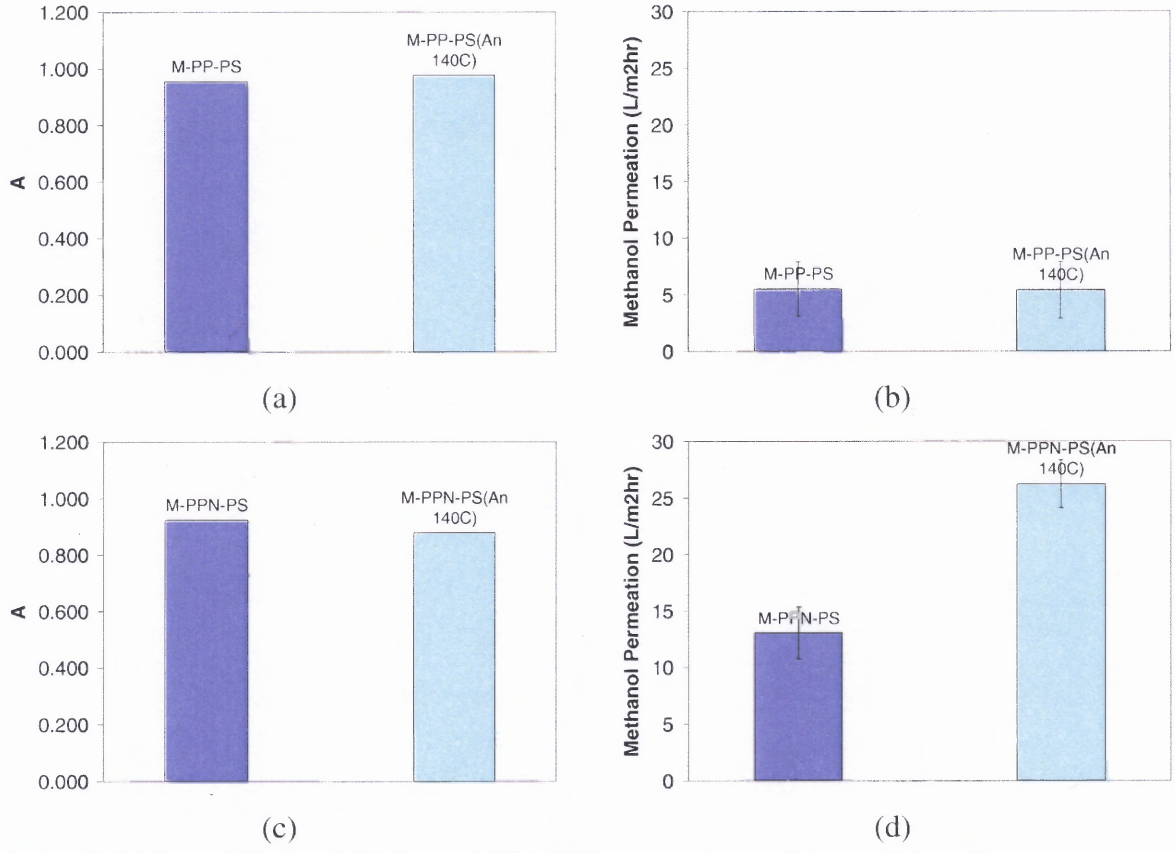

Figure 3.44 Comparison of PP/PS and PPN/PS stretched membranes: (a) α-form orientation index of M-PP/PS samples, (b) methanol permeability of M-PP/PS samples, (c) α-form orientation index of M-PPN/PS samples, (d) methanol permeability of M-PPN/PS samples.

Table 3.13 Thermal Analysis and Methanol Permeation of PP/PS and PPN/PS Precursor Films and Stretched Membranes

Properties	T_m (°C)	Crystallinity (χ_c)	*Methanol permeation (l/m^2hr)[a]
Precursor films (F)			
F-PP/PS	161.0	0.41	No permeation
F-PP/PS(An 140C)	160.4	0.49	No permeation
F-PPN/PS	157.8	0.45	No permeation
F-PPN/PS(An 140C)	156.2	0.49	No permeation
Stretched membranes (M)			
M-PP/PS	163.7	0.41	3.4 ± 1.1
M-PP/PS(An 140C)	163.2	0.46	2.3 ± 0.7
M-PPN/PS	161.9	0.43	13.6 ± 1.7
M-PPN/PS(An 140C)	159.3	0.49	26.9 ± 0.8

* The methanol permeation results were based on the average of four measurements.

Table 3.14 Porosity Estimation of Stretched PP/PS and PPN/PS Membranes

Properties	*χ_c	ρ_{cal} (g/cm^3)	**t (μm)	V_M (mm^3)	M_M (mg)	V_{cal} (mm^3)	Porosity (ε)
M-PP/PS	0.41	0.893	32	57.0	37.1	41.4	0.38
M-PP/PS(An 140C)	0.46	0.897	32	57.0	39.8	44.6	0.28
M-PPN/PS	0.43	0.895	20	35.6	25.2	27.9	0.27
M-PPN/PS(An 140C)	0.49	0.900	25	44.5	30.2	33.3	0.33

* Crystallinity measurement to calculate porosity was based on one sample having methanol permeation value close to the averaged value shown in Table 3.13.
** "t" is the thickness of stretched membrane.

The thermal analysis of the blend precursor film, F-PP-PS(An 140C) is shown in Figure 3.45. The results of F-PP and F-PP(An 140C) are also shown for comparison. A discontinuity related to its annealing temperature is obvious in the F-PP/PS(An 140C) sample (Figure 3.45(c)). Since PP and PS are immiscible, it is expected the DSC heating scan will show two distinct glass transition temperatures for PP (-5 °C) and PS (100 °C), respectively. On the other hand, an endothermic discontinuity (T_2) around 40 °C which represents the enhanced RAF due to the T-lamellae is also expected. In fact, all featured endothermic discontinuities are observed in the first heating scan (Figure 3.45(c), insert). Furthermore, the expected disappearance of T_2 in the second heating is also observed in Figure 3.46.

From previous discussions, the T_2 indicates the presence of enhanced RAF by the T-lamellae and the position of T_2 should represent the degree of confinement of the RAF. The higher T_2 in the F-PP/PS(An 140C) sample than those in the F-PP and F-PP(An 140C) samples (Figure 3.45, insert) implies a more confined RAF in the blend. Since the stretching temperature should be limited in-between T_g of PP and T_2 in order to trigger inter-spherulitic deformation, a higher T_2 in the blend implies an alternative towards the expansion of the range of suitable stretching temperatures.

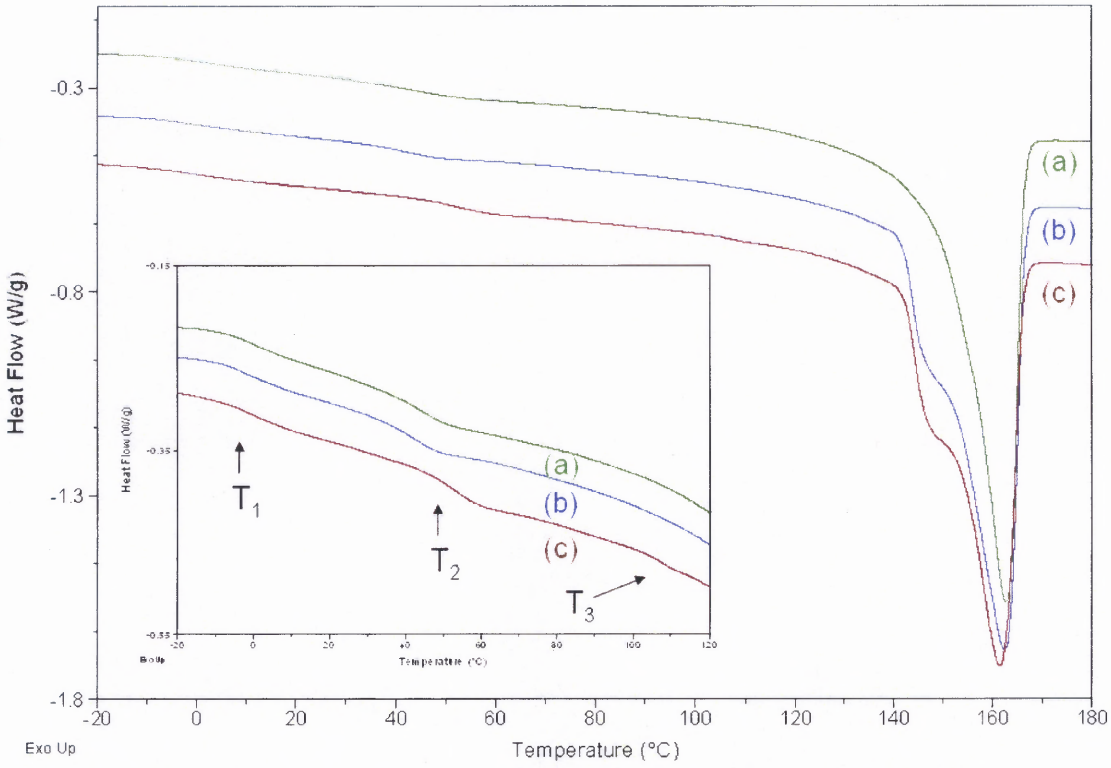

Figure 3.45 DSC heating scan of precursor films (first heating): (a) F-PP, (b) F-PP(An 140C), (c) F-PP/PS(An 140C).

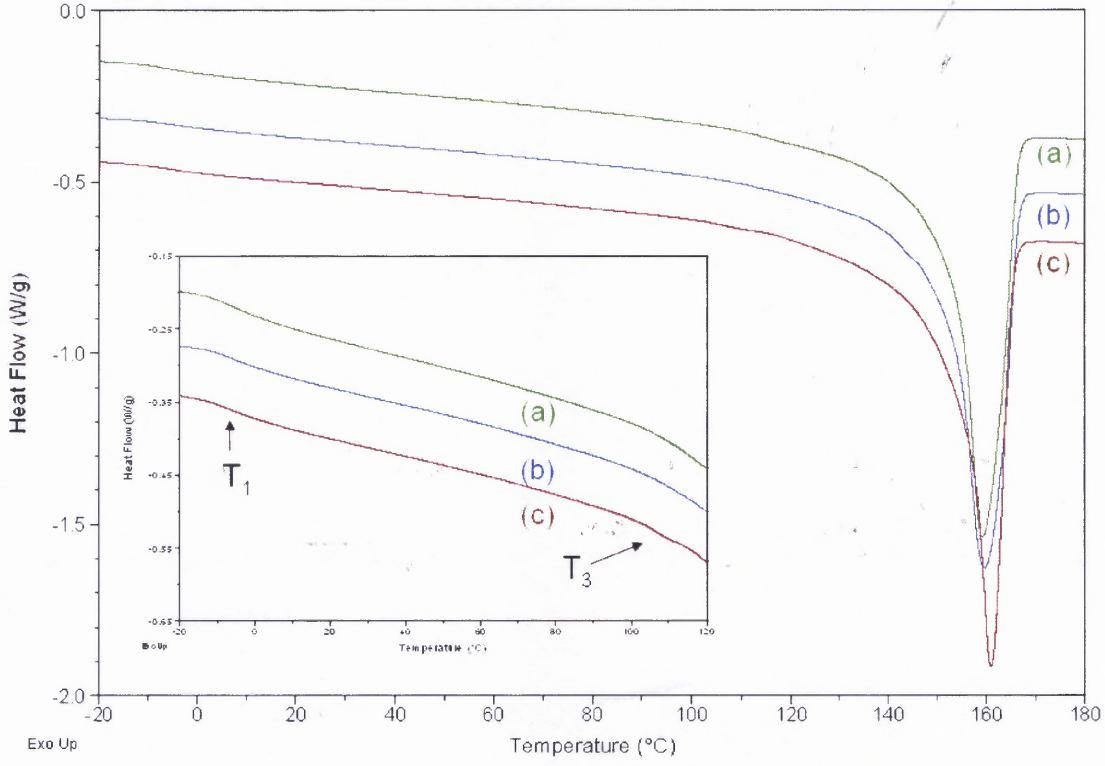

Figure 3.46 DSC heating scan of precursor films (second heating): (a) F-PP, (b) F-PP(An 140C), (c) F-PP/PS(An 140C).

CHAPTER 4

CONCLUSIONS AND RECOMMENDATIONS

4.1 Conclusions

A novel solventless microporous membrane fabrication method via spherulitic deformation of PP has been described in this study. The spherulitic structure in the precursor films was created under low-stress extrusion conditions. A porous structure was generated by annealing and stretching following the extrusion process. Polypropylene was selected due to its unique cross-hatched lamellar morphology of α-form. By taking advantage of the feature of tangential lamellae, a microporous structure was created by combining intra-spherulitic and inter-spherulitic deformation. A tangential lamellae-rich spherulite was created and identified with a positive birefringence sign. A sequential annealing process improved the crystalline structure, and in particular the thickness of the tangential lamellae.

The inter/intra spherulitic deformation was identified morphologically by optical and scanning electron microscopy. A stretched membrane with additional inter-spherulitic deformation appears to have higher porosity and better pore interconnectivity than other membranes containing only intra-spherulitic deformation. A less deformed spherulitic structure appears to prevent the lamellar openings from totally collapsing and maintain the interconnectivity. A simple WAXS examination can provide a quick methodological characterization of the inter-spherulitic deformation. The microscopic evidences representing the occurrence of intra/inter spherulitic transition on a spherulitic scale can also be detected on a lamellar scale by WAXS examination. A highly oriented sample showed a high value of

showed a low value of α-form orientation index. Porosity measurements of the stretched membranes showed a consistent correlation with their α-form orientation index. A highly interconnected solvent-resistant porous membrane having a pore size in the range of 50~100 nm and an estimated porosity of 0.18 was developed in the non-nucleated PP samples of this study.

There are two potential modifications to the proposed novel membrane fabrication process in order to improve the membrane performance. The first modification is to reduce the spherulite size by using nucleated polypropylene. The presence of smaller spherulites in the membrane produced under the same conditions from α-nucleated PPN samples resulted in higher methanol permeability and an estimated porosity of 0.29. The second modification is to utilize interfacial debonding between two different phases to enhance permeability. The debonded structure could be created by using an immiscible polymer blend system or a polymer containing fillers. The selection of PS as a second phase was based: a) on its relatively high T_g and, hence, low deformability during the room temperature stretching, and b) the viscosity ratio of PP/PS of about unity over a wide range of shear rates, which meets the requirements for good dispersion. High permeability was also observed in the membrane made from the immiscible blend. However, the formation of debonded morphology compensates for energy absorbed by stretching and limits inter-spherulitic deformation.

The post-processing boundary conditions for utilizing intra/inter spherulitic deformation to create microporous membranes by lamellar separation have been delineated. The investigated conditions included: annealing temperature, extension ratio, stretching rate, and stretching temperature. A fixed set of extrusion conditions was chosen for producing precursor films with similar spherulitic properties. The increasing extension ratio did not

change the microstructure of the deformed region in the intra-spherulitically deformed sample where the proportion of the cold-drawn region increased and that of the non-deformed region decreased with increasing extension ratio. However, the microstructure of the inter-spherulitically deformed sample can be modified by orientation with increasing extension ratio. In this study, the residual lamellae at the separated spherulitic boundaries were strong enough to prevent sample rupture. Inter-spherulitic deformation became more pronounced at slow stretching rates, since the stress generated by stretching would have time to be transmitted to the weak sites, such as the spherulite boundaries. On the other hand, intra-spherulitic deformation was more favored at a fast stretching rate.

At high stretching temperatures, the expected typical cold-drawn appearance was not evident in the non-annealed sample, and a less opaque appearance was found in the annealed sample. These unexpected behaviors are believed to be related to the rigid amorphous fraction (RAF) trapped inside the cross-hatched lamellar morphology of the α-PP. DSC thermal analysis of the precursor films showed two distinct endothermic discontinuities; the first was at 0 °C (T_1) and the other was at 40 °C (T_2). T_1 is believed to be the conventional T_g of polypropylene, and T_2 represents the significant amount of RAF trapped within the "lamellar wells" where the amorphous phase is surrounded by R-lamellae and T-lamellae. The effect of RAF is minimized at stretching temperatures higher than T_2, and the amorphous phase in the "lamellar wells" can not provide sufficient strength to sustain the lamellar morphology. The lamellae could break down or slip from the lamellar knots, and the annealed lamellae can still be oriented without catastrophic cold-drawn deformation. The presence of a second endothermic discontinuity (T_2) is also shown in the PPN and PP/PS

samples. The higher T_2 in the PP/PS sample imply an alternative toward expansion of the range of suitable stretching temperatures.

4.2 Recommendations

An important part of this work is to illustrate the concept of using a spherulitic morphology to create controllable porous structures. Approximate processing criteria for initiating inter-spherulitic deformation and subsequent characterization methods have been explored. The preliminary results on two modifications (reduced spherulite size and utilization of an interfacial debonding morphology) have also been included. There are some interesting topics that could be pursued as a future work.

Firstly, the effect of the orientation on the spherulitic morphology in the extruded precursor films is important. The presence of spherulitic morphology with low-orientation morphology is critical to ensure biaxial mechanical properties in the stretched membranes. At the same time, reproduction of T-lamellae-rich α-spherulites has to be maintained. Secondly, the annealing conditions are critical and should be investigated in detail. An *in-situ* annealing step during precursor film extrusion could be useful for continuous production. Thirdly, WAXS provides a quick examination on the occurrence of inter-spherulitic deformation and a systematic and rapid characterization of the pore structure could be used as a feedback to regulate the processing conditions. Finally, a multiple-step stretching and biaxial stretching could be used to enhance membrane performance.

On the other hand, an optimization on the nucleating by adding an α-nucleating agent could be very useful. The efficiency of nucleating can be regulated by the types and concentrations of α-nucleating agents. Furthermore, the effect of stress concentration due to

the dispersed domains in the immiscible blend and the corresponding debonded morphology needs to be addressed in order to maximize the membrane performance.

APPENDIX A

PORE SIZE CHARACTERIZATION

As mentioned in previous sections, the stretched membranes with high permeability (M-PP(An 140C) and M-PPN(An 140C)) were obtained due to the inter-spherulitic deformation. The pore size of these porous membranes appeared to be about 50 ~ 100 nm from SEM micrographs (Figure 3.13(b)). Even though the porous structure beneath the membrane surface can somehow be revealed by the debonded morphology shown in Figure 3.13(c), the issue of pore size and pore size distribution needs to be addressed in greater detail.

A preliminary study for pore size characterization was carried on by particle rejection tests using zein protein [77] and polystyrene (PS) latex microspheres [78]. The nominal size of zein protein is about 3 nm and the size of PS latex microsphere suspensions (from Duke Scientific, Fremont, CA) were 30 nm (5003A) and 300 nm (5030A). The experimental setup for rejection test is similar to those used in methanol permeation test except the feed solution contained diluted particles. The α-zein protein was dissolved in 70% ethanol solution and the PS latex microspheres were suspended in methanol. The usage of 70% ethanol solution and methanol solution through microporous membranes did not show much difference in the solvent flux during the rejection test. A VARIAN Cary 50 UV-visible spectrophotometer (Varian, Palo Alto, CA) was used to determine the concentration of the permeant. The results of rejection test of membranes with inter-spherulitic deformation and their pore features are summarized in Table A.1.

Table A.1 Porosity, Methanol Permeation and Rejections of Zein Protein and PS Latex (300nm) Particles of PP and PPN Based Stretched Membranes.

Samples	Porosity (ε)	Methanol permeation (l/m^2hr)	Rejection (%) of zein protein (D = 3 nm)	Rejection (%) of PS latex (D = 300 nm)
M-PP(An 140C)	0.18	4.5 ± 1	2	95
M-PPN(An 140C)	0.29	18.7 ± 2.2	1	95
M-PP/PS(An 140C)	0.28	2.3 ± 0.7	2	90
M-PPN/PS(An 140C)	0.33	26.9 ± 0.8	2	95

As expected, the zein rejection of these membranes was low and the PS latex (300 nm) rejection of them was quite high, which is consistent with the observation from SEM micrographs. A traceable amount of PS latex detected in the permeant might be due to the residual PS latex deposited on the collecting tube. On the other hand, the results of PS latex (30 nm) rejection of these membranes are not shown in Table A.1 due to inconsistencies in measurement. The inconsistency of PS latex (30 nm) was observed due to the shifting peak in UV spectra (Figure A.1). This might be due to agglomeration of the PS latex (30 nm). However, this inconsistency was not significant in the larger PS latex (300 nm). A systematic experiment on agglomeration of PS latex microsphere needs to be conducted since the estimated pore size is about 50 ~ 100 nm based on SEM observation.

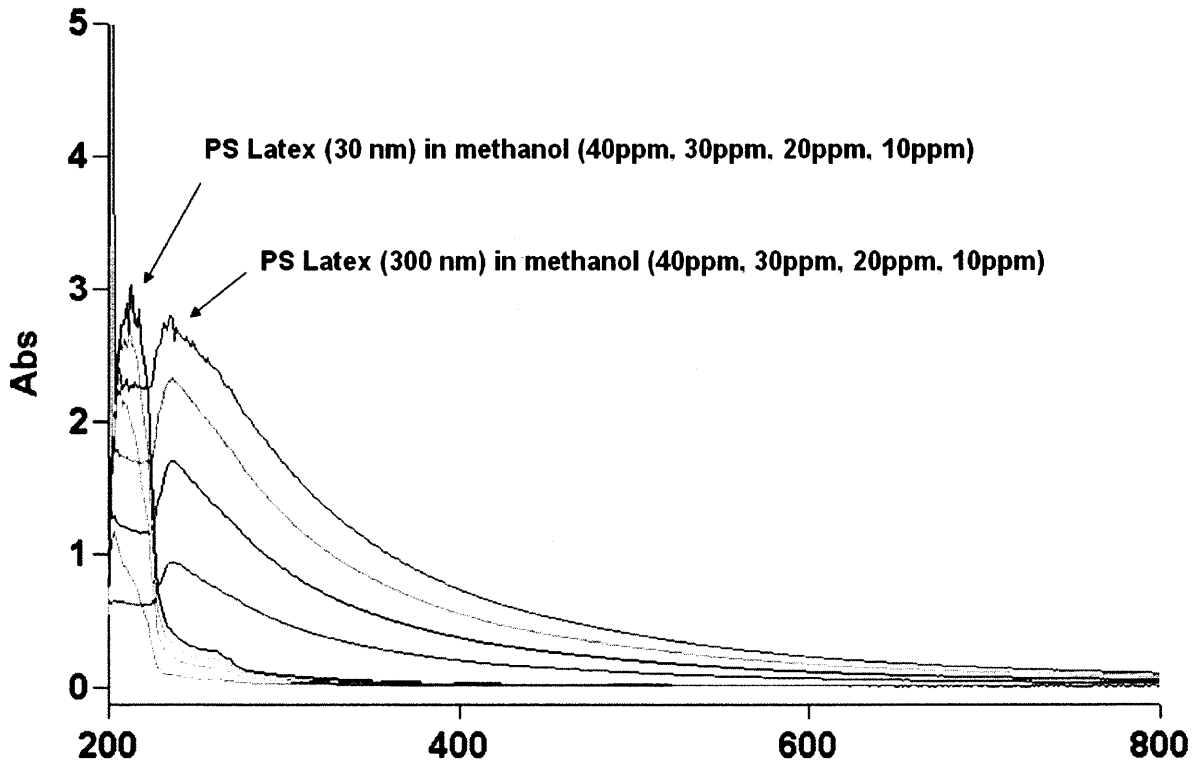

Figure A.1 UV spectra of PS latex (30 nm and 300 nm) in methanol.

An alternative method to measure pore characteristics is using a Capillary Flow Porometer (Porous Materials, Inc.) which adapted the principle of bubble point measurement. Pore size and pore size distribution can be detected with an appropriate selection of wetting solvents. At this time, this method can measure the pore within the range of 10 nm to 20 μm.

APPENDIX B

ALTERNATIVE SELECTIONS FOR IMMISCIBLE POLYMERIC BLENDS

Hydrophobic semicrystalline major phase / Hydrophilic semicrystalline minor phase

System I: Poly(4-methyl-1-pentene)/Polyethylene vinyl alcohol (PMP/EVOH)

The first system chosen to extend the concept of immiscible blends was Poly(4-methyl-1-pentene) (PMP)/ Polyethylene vinyl alcohol copolymer (EVOH). PMP was used as a hydrophobic matrix and EVOH as a hydrophilic dispersed phase. The material properties are listed in Table B.1. Both polymers are semicrystalline with high melting temperatures. The immiscible blend was prepared by twin screw extruder compounding. Because of the mismatched rheological properties, a compatibilizer, Lotader® AX8950, was used to improve the dispersion of EVOH. Scanning electron microscope (SEM) images of fracture surfaces of the blends, with or without compatibilizer, are shown in Figure B.1. The EVOH dispersed phase was broken down to about 5μm with the help of the compatibilizer, from 5 to 20 μm without the compatibilizer.

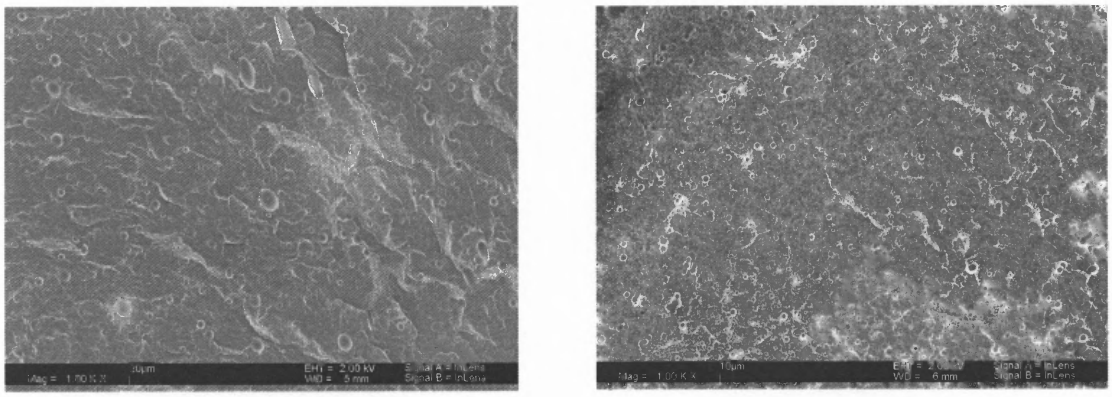

(a) (b)

Figure B.1 SEM images of fracture surface of blends (a) PMP/EVOH (90/10) (b) PMP/EVOH/AX8950 (90/10/2).

Table B.1 Material Properties

Polymer	**Used in system**	**Grade**	**Source**	**Density (g/cm^3)**	**T_g (°C)**	**T_m (°C)**	**T_c (°C)**	**Melt Flow Rate (g/10min)**
Poly(4-methyl-1-pentene), (PMP)	I	MX002	Mitsui Chemical America	0.835	20	235	200	22 (260 °C, 5 kg)
Polyethylene vinyl alcohol copolymer, (EVOH)	I and II	F171B	EVALCA	1.19	57	182	158	3.7 (210 °C, 2.16 kg)
Polypropylene (PP)	II and III	H413-02Z	Dow	0.9	-5	162	115	2 (230 °C, 2.16 kg)
Ethylene-methyl acrylate-glycidyl methacrylate terpolymer, (E/MA/MGA)	I	Lotader® AX8950	ATOFINA	0.94	NA	NA	NA	NA
Functionalized polyolefin, (PP type)	II	ADMER® QF551A	Mitsui Chemicals	0.89	NA	NA	NA	4.7 (230 °C, 2.16 kg)
Sulfonated PS	III	Versa-TL®70	ALCO Chemicals	0.8	NA	NA	NA	NA

The precursor films of the blends were extruded by a Brabender single screw extruder equipped with a sheet die. Membranes were prepared by stretching the precursor films at different stretching rates (R_S), 0.25 cm/min to 6.25 cm/min, extension ratios (E_S), 100% to 200%, and stretching temperatures (T_S), 25 °C to 80 °C. Figure B.2 represents the SEM images of stretched membranes at a stretching temperature between the T_g-s of PMP and EVOH. In the PMP/EVOH system, a debonded structure is observed, which indicates poor interfacial adhesion between the hydrophobic PMP (nonpolar) and the hydrophilic EVOH (polar) phases. A craze at the tip of the debonded structure might result from the less ductile behavior of PMP at low stretching temperature, which is close to its T_g, and the higher stress level around the dispersed phase, which is due to its larger size. In the PMP/EVOH/AX8950 system, a less pronounced debonded structure is shown in Figure B.2(b). A series of experiments by varying stretching conditions was conducted in the PMP/EVOH/AX8950 system. However, no significant morphological differences in the stretched membranes were found. There was no methanol permeation up to 24 hour of testing in both cases. This might be a result of the strong adsorption of energy due to the debonding process induced by the weak interfacial adhesion.

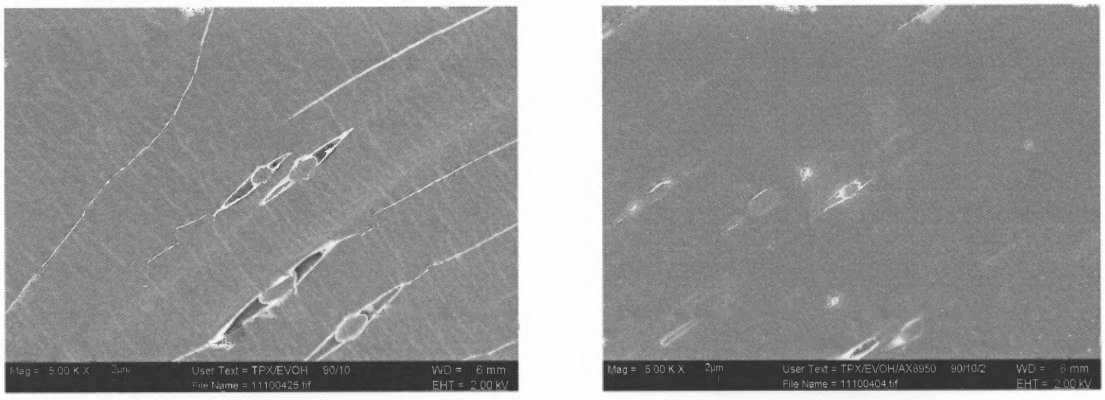

(a) (b)

Figure B.2 SEM images of stretched membranes (a) PMP/EVOH (90/10) (b) PMP/EVOH/AX8950 (90/10/2). (R_S = 2.5 cm/min, T_S = 25 °C, and E_S = 200%)

System II: Polypropylene/Polyethylene vinyl alcohol (PP/EVOH)

The second system selected for the study was Polypropylene (PP)/ Polyethylene vinyl alcohol copolymer (EVOH). PP was used as a hydrophobic matrix phase and EVOH as a hydrophilic dispersed phase. A PP-type adhesive resin, ADMER® QF551A, was used as a compatibilizer in this system. Because of the significant mismatch in the rheological behaviors between PP and EVOH, the compatibilizer was chosen for improving the interfacial adhesion. However, it could still reduce the size of the dispersed phase effectively. The preparation of immiscible blends, precursor films, and stretched membranes followed the procedure described in the previous section. The blend morphologies of PP/EVOH and PP/EVOH/QF551A are shown in Figure B.3. The effect of compatibilizer concentration and a two-step mixing protocol on the blend morphology are shown in Figure B.4. The size of the dispersed phase decreases with increasing compatibilizer concentration. From our previous study, using the two-step mixing protocol can improve the dispersion of the minor phase. In the two-step mixing process, EVOH/QF551A was compounded and pelletized first, and then the blend was compounded with PP. The mixing protocol does not show a dramatic change

on the blend morphologies of the PP/EVOH/QF551A (Figure B.4(b) and (d)). However, it does alter the morphology of the stretched membrane.

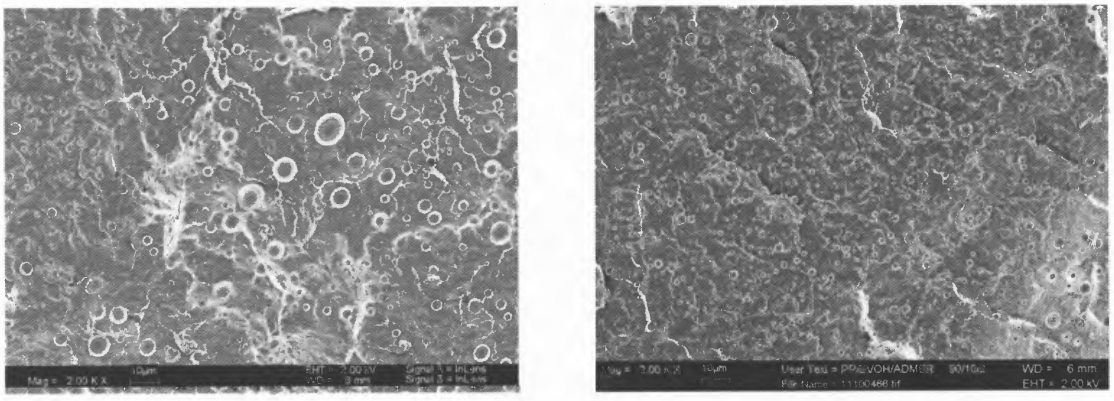

(a) (b)

Figure B.3 SEM images of fracture surface of extruded blends (a) PP/EVOH (90/10) (b) PP/EVOH/QF551A (90/10/2).

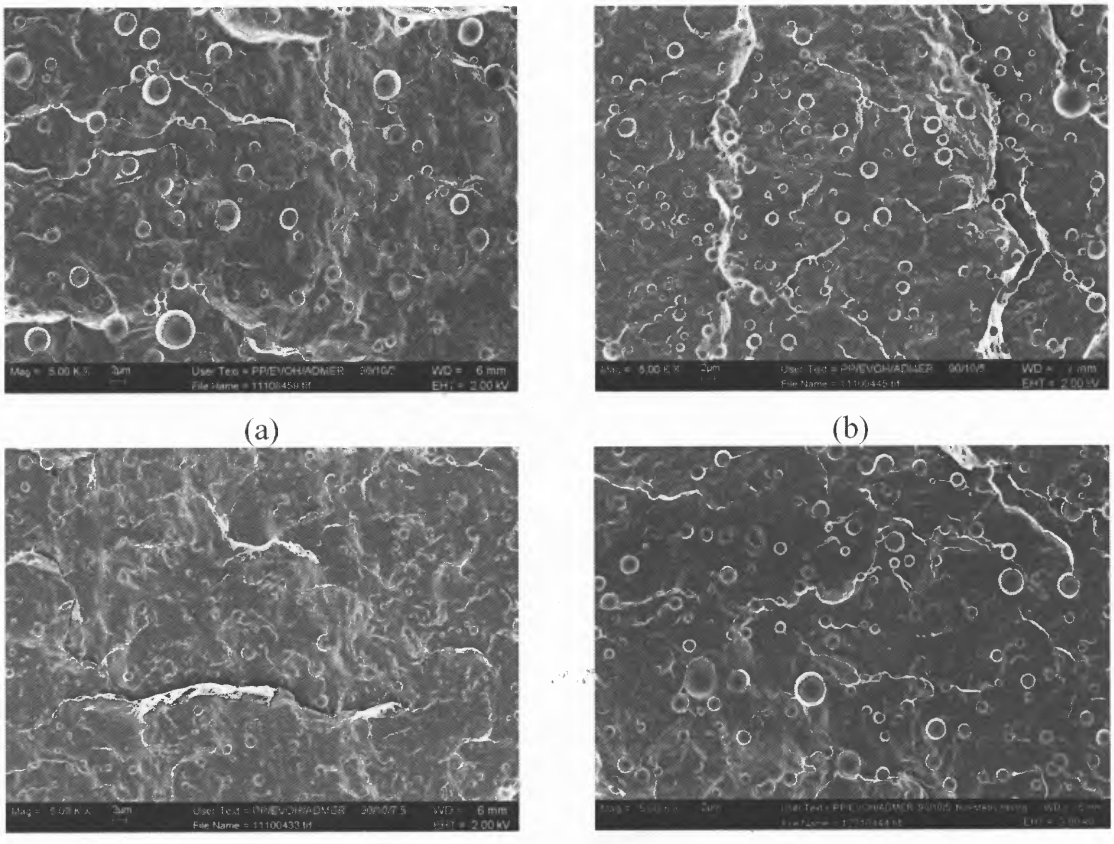

(a) (b)

(c) (d)

Figure B.4 SEM images of fracture surface of extruded blends (a) PP/EVOH/QF551A (90/10/2) (b) PP/EVOH/QF551A (90/10/5) (c) PP/EVOH/QF551A (90/10/7.5) (d) PP/EVOH/QF551A (90/10/5), two-step mixing.

The morphology of the stretched membranes (two-step mixing protocol, stretching temperature between T_g-s of PP and EVOH) is shown in Figure B.5. The predominant morphology in these membranes is debonded pores around a dispersed phase. The numbers of debonded pores around the smaller dispersed phase, Figure B.5(a), indicates poor interfacial adhesion between PP/EVOH even in the presence of the compatibilizer. Debonding happened at a lower stress level around the smaller dispersed phase. On the other hand, the interfacial adhesion can be improved by the two-step mixing. The lack of small debonded pores in Figure B.5(b) indicates a better interfacial adhesion around the small dispersed phase. However, the presence of large debonded pores shows the interfacial adhesion still was not high enough to prevent debonding at the higher stress level around the larger dispersed phase. There was no methanol permeation up to 24 hour of testing in these samples. This might be due to the strong adsorption of energy resulting from debonding induced by the weak interfacial adhesion.

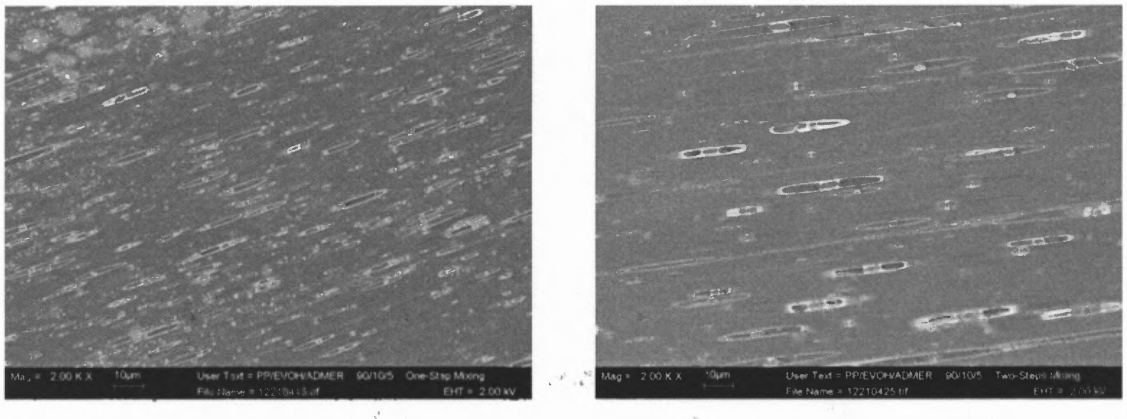

(a) (b)

Figure B.5 SEM images of stretched membranes (a) PP/EVOH/QF551A (90/10/5), one-step mixing (b) PP/EVOH/QF551A (90/10/5), two-step mixing. (R_S = 2.5 cm/min, T_S = 25 °C, and E_S = 200%).

Hydrophobic semicrystalline major phase / Hydrophilic amorphous minor phase

System III: Polypropylene/Sulfonated Polystyrene (PP/Sulfonated-PS)

Following our earlier work with PP/PS system, it was decided to evaluate a polar/nonpolar system using PP/Sulfonated PS system. The sulfonated PS was obtained as a powder form. However, attempts to process it in the present of PP by melt mixing equipment were not successful due to its lack of a distinct softening temperature. Further experiments were not conducted for this system.

REFERENCES

1. Baker, R.W., ed. *Membrane Technology and Applications*. 2nd ed. 2004, John Wiley & Sons Ltd.: West Sussex, England.

2. Vandezande, P., Gevers, L. E. M., Vankelecom, I. F. J., *Solvent resistant nanofiltration: separating on a molecular level.* Chemical Society Reviews, 2008. **37**: p. 365.

3. Paul, D.R., Yampol'skii, Y. P., ed. *Polymeric gas separation membranes*. 1994, CRC Press Inc.: Boca Raton, FL.

4. Kesting, R.E., ed. *Synthetic Polymeric Membranes*. 2nd ed. 1985, John Wiley & Sons, Inc.: NYC, New York.

5. Atkinson, P.M., Lloyd, D. R. , *Anisotropic flat sheet membrane formation via TIPS: thermal effects.* Journal of Membrane Science, 2000. **171**: p. 1.

6. Lai, J.-Y., Lin, F. -C., Wu, T. -T., Wang, D. -M., *On the formation of macrovoids in PMMA membranes.* Journal of Membrane Science, 1999. **155**: p. 31.

7. Nunes, S.P., Peinemann, K. -V., ed. *Membrane technology in the chemical industry*. 2001, Wiley-VCH: Weinheim, Germany.

8. Arora, P., Zhang Z., *Battery separators.* Chemical Reviews, 2004. **104**: p. 4419.

9. Chen, R.T., Saw, C. K., Jamieson, M. G., Aversa, T. R., Callahan, R. W., *Structural characterization of Celgard microporous membrane precursors: melt-extruded polyethylene films* Journal of Applied Polymer Science, 1994. **53**: p. 471.

10. Tadmor, Z., Gogos, C. G., ed. *Principles of Polymer Processing*. 1979, John Wiely & Sons: NYC, New York.

11. Schultz, J.M., ed. *Polymer Crystallization*. 2001, Oxford University Press: NYC, New York.

12. Sprague, B.S., *Relationship of structure and morphology to properties of "hard" elastic fibers and films.* Journal of Macromolecular Science Physics, 1973. **B8**(1-2): p. 157.

13. Keller, A., Machin, M. J., *Oriented crystallization in polymers.* Journal of Macromolecular Science Physics, 1967. **B1**(1): p. 41.

14. Schultz, J.M., *Microstructural aspect of failure in semicrystalline polymers.* Polymer Engineering and Science, 1984. **24**: p. 770.

15. Sadeghi, F., Ajji, A., Carreau, P. J., *Analysis of microporous membranes obtained from polypropylene films by stretching.* Journal of Membrane Science, 2007. **292**: p. 62.

16. Samuels, R.J., *Effect of Structure on the Deformation and Failure of Oriented Polymer Films.* Polymer Engineering and Science, 1999. **39**: p. 2358.

17. Samuels, R.J., *The Influence of Structure on the Failure of Isotactic Polypropylene Films.* Polymer Engineering and Science, 1979. **19**(2): p. 66.

18. Lee, S.-Y., Park, S. -Y., Song, H. -S., *Lamellar crystalline structure of hard elastic HDPE films and its influence on microporous membrane formation.* Polymer, 2006. **47**: p. 3540.

19. Perterlin, A., *Molecular model of drawing polyethylene and polypropylene.* Journal of Materials Science, 1971. **6**: p. 490.

20. Bowden, P.B., Young, R. J., *Review: Deformation mechanism in crystalline polymers.* Journal of Materials Science, 1974. **9**: p. 2034.

21. Sperling, L.H., ed. *Introduction to Physical Polymer Science.* 3rd ed. 2001, John Wiley & Sons: NYC, New York.

22. Butler, M.F., Donald, A. M., *Deformation of spherulitic polyethylene thin films.* Journal of Materials Science, 1997. **32**: p. 3675.

23. Dijkstra, P.T.S., Van Dijk, D. J., Huetink, J. , *A microscopy study of transition from yielding to crazing in polypropylene.* Polymer Engineering and Science, 2002. **42**: p. 152.

24. Way, J.Y., Atkinson, J. R., Nutting, J., *The effect of spherulite size on the fracture morphology of polypropylene.* Journal of Materials Science, 1974(9): p. 293.

25. Zhou, J.-J., Liu, J. -G, Yan, S. -K, Dong, J. -Y. Chan, C. -M., Schultz, J. M., *Atomic force microscope study of the lamellar growth of isotactic polypropylene.* Polymer, 2005. **46**: p. 4077.

26. Jang, B.Z., Uhlmann, D. R., Vander Sande, J. B., *Crazing in polypropylene.* Polymer Engineering and Science 1985. **2**(25): p. 98.

27. Pasquini, N., ed. *Polypropylene Handbook.* 2nd ed. 2005, Hanser Gardner Publications, Inc.: Cincinnati, OH.

28. Ibhadon, A.O., *Fracture Mechanics of Polypropylene: Effect of Molecular Characteristics, Crystallization Conditions, and Annealing on Morphology and Impact Performance.* Journal of Applied Polymer Science, 1998. **69**: p. 2657.

29. Varga, J., *Review: Supermolecular structure of isotactic polypropylene.* Journal of Materials Science, 1992. **27**: p. 2557.

30. Karger-Kocsis, J., ed. *Polypropylene*. 1999, Kluwer Academic Publishers: Dordrecht, The Netherlands.

31. Li, J.X., Cheung, W. L., *On the deformation mechanisms of β-polypropylene: 1. Effect of necking on β-phase PP crystals.* Polymer, 1998. **39**: p. 6935.

32. Campbell, R.A., Phillips, P. J., Lin, J. S., *The gamma phase of high-molecular-weight polypropylene: 1. Morphological aspects.* Polymer, 1993. **34**: p. 4809.

33. Mezghani, K., Phillips, P. J., *The γ–phase of high molecular weight isotactic polypropylene. II: The morphology of γ–form crystallized at 200 MPa.* Polymer, 1997. **38**: p. 5725.

34. Grubb, D.T., Yoon, D. Y., *Morphology of quenched and annealed isotactic polypropylene.* Polymer Communications, 1986. **27**: p. 84.

35. Hsu, C.C., Geil, P. H., *Structure and Properties of Polypropylene Crystallized from Glass State.* Journal of Polymer Science Part B: Polymer Physics, 1986. **24**: p. 2379.

36. Coccorullo, I., Pantani, R., Titomanlio, G., *Crystallization kinetics and solidified structure in iPP under high cooling rate.* Polymer, 2003. **44**: p. 307.

37. Vittoria, V., *Effect of Annealing on the Structure of Quenched Isotactic Polypropylene.* Journal of Macromolecular Science Physics, 1989. **B28**(3&4): p. 489.

38. Turner Jones, A., Aizlewood, J. M., Beckett, D. R. , Makromolekulare Chemie 1964. **75**: p. 134.

39. Rodriguez, F., Cohen, C., Ober, C. K., Archer, L. A., ed. *Principles of Polymer Systems*. 5th ed. 2003, Taylor & Francis: NYC, New York.

40. Lotz, B., *What can polymer crystal structure tell about polymer crystallization processes?* The European Physical Journal E, 2000. **3**: p. 185.

41. Salamone, J.C., ed. *Polymeric Materials Encyclopedia.* 1996, CRC press: Boca Raton, FL.

42. Lotz, B., Wittmann, J. C., *The molecular origin of lamellar branching in the a (monoclinic) form of isotactic polypropylene.* Journal of Polymer Science Part B: Polymer Physics, 1986. **24**: p. 1541.

43. Lotz, B., Wittmann, J. C., Lovinger, A. J., *Structure and morphology of poly(propylene): a molecular analysis.* Polymer, 1996. **37**: p. 4979.

44. Padden, F.J.J., Keith, H. D. , *Mechanism for lamellar branching in isotactic polypropylene.* Journal of Applied Physics, 1973. **44**: p. 1217.

45. Norton, D.R., Keller, A., *The spherulitic and lamellar morphology of melt-crystallized isotactic polypropylene.* Polymer, 1985. **26**: p. 704.

46. Aboulfaraj, M., G'Sell, C., Ulrich, B., Dahoun, A., *In situ observation of plastic deformation of polypropylene spherulites under uniaxial tension and simple shear in the scanning electron microscope.* Polymer, 1995. **36**: p. 731.

47. Coulon, G., Castelein, G., Gsell, C., *Scanning force microscopic investigation of plasticity and damage mechanism in polypropylene spherulites under simple shear.* Polymer, 1998. **40**: p. 95.

48. Way, J.Y., Atkinson, J. R., *Some studies of deformation processes in fully-spherulitic polypropylene.* Journal of Materials Science, 1971. **6**: p. 102.

49. Karger-Kocsis, J., Varga, J., *Effect of β–α Transformation on the Static and Dynamic Tensile Behavior of Isotactic Polypropylene.* Journal of Applied Polymer Science, 1996. **62**: p. 291.

50. Tordjeman, P., Robert, C., Marin, C., Gerard P., *The effect of α, β crystalline structure on the mechanical properties of polypropylene.* European Physical Journal 2001. **E**(4): p. 459.

51. Labour, T., Vigier, G., Seguela, R., Gauthier, C., Orange, G., Bomal, Y., *Influence of the β-Crystalline Phase on the Mechanical Properties of Unfilled and Calcium Carbonate-filled Polypropylene: Ductile Cracking and Impact Behavior.* Journal of Polymer Science Part B: Polymer Physics, 2001. **40**: p. 31.

52. Li, J.X., Cheung, W. L., Chan, C. M. , *On the deformation mechanisms of β-polypropylene 2. Changes of lamellar structure caused by tensile load* Polymer, 1999. **40**: p. 2089.

53. Alamo, R.G., Kim, M. H., Galante, M. J., Isasi, J. R., Mandelkern, L. , *Structural and kinetic factors governing the formation of the γ polymorph of isotactic polypropylene.* Macromolecules, 1999. **32**: p. 4050.

54. Iijima, M., Strobl, G., *Isothermal crystallization and melting of isotactic polypropylene analyzed by time- and temperature-dependence small-angle X-ay scattering experiments.* Macromolecules, 2000. **33**: p. 5204.

55. Bruckner, S., Meille, S. V., Petraccone, V., Pirozzi, B., *Polymorphism in isotactic polypropylene.* Progress in Polymer Science, 1991. **16**: p. 361.

56. Kristiansen, M., Tervoort, T., Smith, P., Goossens, H., *Mechanical Properties of Sorbitol-Clarified Isotactic Polypropylene: Influence of Additive Concentration on Polymer Structure and Yield Behavior.* Macromolecules, 2005. **38**: p. 10461.

57. Kotek, J., Kelnar, I., Baldrian J., Raab, M., *Tensile behavior of isotactic polypropylene modified by specific nucleation and active fillers.* European Polymer Journal 2004. **40**: p. 679.

58. Nagasawa, S., Fujimori, A., Masuko, T., Iguchi, M., *Crystallization of polypropylene containing nucleators.* Polymer, 2005. **46**: p. 5241.

59. Sudar, A., Moczo, J., Voros, G., Pukanszky, B., *The mechanism and kinetics of void formation and growth in particulate filled PE composites.* eXPRESS Polymer Letter, 2007. **1**: p. 763.

60. Chandavasu, C., Xanthos, M., Sirkar, K. K., Gogos, C. G., *Polypropylene blends with potential as materials for microporous membranes formed by melt processing.* Polymer, 2002. **43**: p. 781.

61. Michler, G.H., Balta-Calleja, F. J., ed. *Mechanical Properties of Polymers Based on Nanostructural and Morphology.* 2005, CRC Press: Boca Raton, FL.

62. Meeten, G.H., ed. *Optical properties of polymers.* 1986, Elsevier: NYC, New York.

63. Poussin, L., Bertin, Y. A., Parisot, J., Brassy, C. , *Influence of thermal treatment on the structure of an isotactic polypropylene.* Polymer, 1998. **39**: p. 4261.

64. Alamo, R.G., Brown, G. M., Mandelkern, L., Lehtinen, A., Paukkeri, R. , *A morphological study of a highly structurally regular isotactic poly(polypylene) fraction.* Polymer, 1999. **40**: p. 3933.

65. Wu, C.M., Chen, M. and Karger-Kocsis, J., *Effect of micromorphological features on the interfacial strength of iPP/Kevlar fiber microcomposites.* Polymer 2001. **42**: p. 199.

66. Botev, M., Neffati, R., Rault, J., *Mobility and relaxation of amorphous chains in drawn polypropylene: H-NMR study.* Polymer, 1999. **40**: p. 5227.

67. Boyer, R.F., *An apparent double glass transition in semicrystalline polymers.* Journal of Macromolecular Science, Part B Physics, 1973. **B8**(3-4): p. 503.

68. Boyd, R.H., *Relaxation processes in crystalline polymers: experimental behavior - a review.* Polymer, 1985. **26**: p. 323.

69. Hedesiu, C., Demco, D. E., Kleppinger, R., Vanden Poel, G., Gijsbers, W., Blumich, B., Remerie, K., Litvinov, V. M. , *Effect of temperature and annealing on the phase composition, molecular mobility, and the thickness of domains in isotactic polypropylene studied by proton solid-state NMR, SAXS, and DSC.* Macromolecules, 2007. **40**: p. 3977.

70. Sawyer, L.C., Grubb D. T., *Polymer Microscopy.* 1996, Springer: NYC, New York.

71. Harold, P.K., Alexander, L. E., *X-Ray Diffraction Procedures: For Polycrystalline and Amorphous Materials*. 1974: Wiley-Interscience.

72. Samios, D., Tokumoto, S., Denardin, E. L. G., *Large plastic deformation of isotactic poly(propylene) (iPP) evaluated by WAXD techniques.* Macromolecular Symposia, 2005. **229**: p. 179.

73. Trotignon, J.P., Lebrun J. L., Verdu, J., *Crystalline polymorphism and orientation in injection-moulded polypropylene.* Plastics and Rubber Processing and Applications, 1982. **2**: p. 247.

74. Suzuki, H., Grebowicz, J., Wunderlich, B., *Glass transition of poly(oxymethylene).* British Polymer Journal, 1985. **17**(1): p. 1.

75. Androsch, R., Wunderlich, B., *The link between rigid amorphous fraction and crystal perfection in cold-crystallized poly(ethylene terephthalate).* Polymer, 2005. **46**: p. 12556.

76. Drozdov, A.D., Christiansen, J. deC., *The effect of annealing on the elastoplastic and viscoelastic responses of isotactic polypropylene.* Computational Materials Science, 2003. **27**: p. 403.

77. Korikov, A.P., Kosaraju, P. B., Sirkar, K. K., *Interfacially polymerized hydrophilic microporous thin film composite membranes on porous polypropylene hollow fibers and flat films.* Journal of Membrane Science, 2006(279): p. 588.

78. Lee, Y., Clark, M. M., *Modeling of flux decline during crossflow ultrafiltration of colloidal suspensions.* Journal of Membrane Science, 1998(149): p. 181.